PB84-110493

NBS (National Bureau of Standards)
Materials Measurements

(U.S.) National Bureau of Standards
Washington, DC

Prepared for

National Aeronautics and Space Administration
Washington, DC

Aug 83

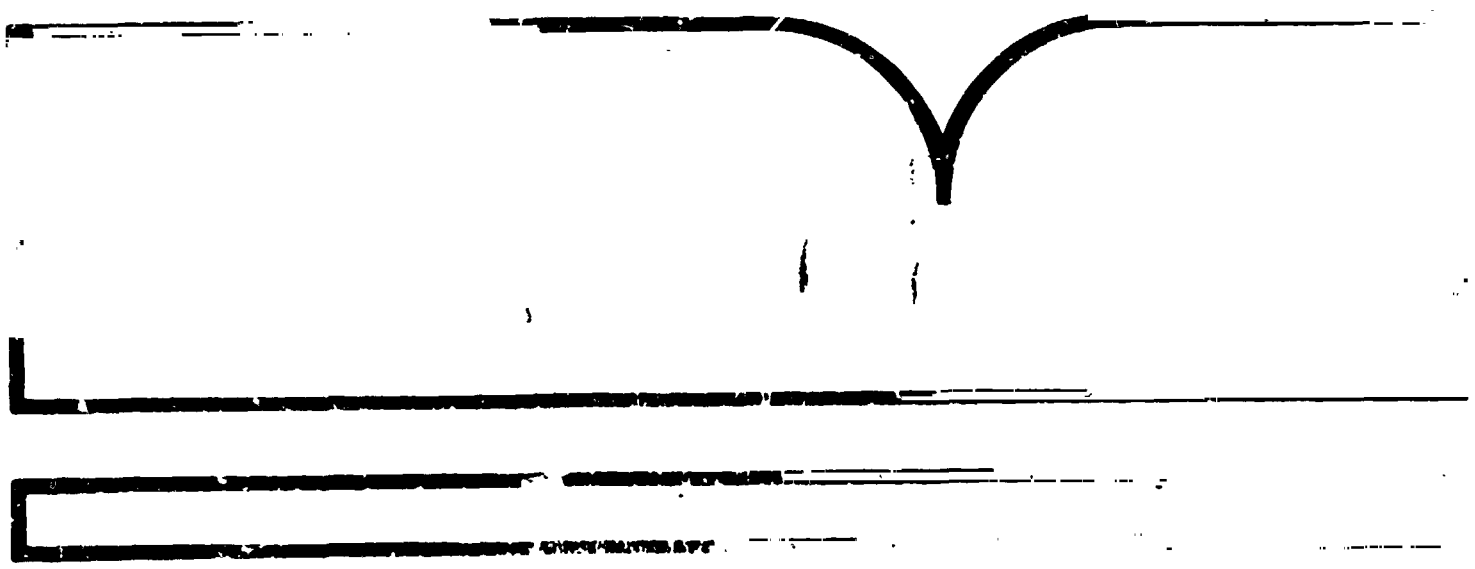

NBS-114A (REV. 2-8C)

PB84 110493

U.S. DEPT. OF COMM. BIBLIOGRAPHIC DATA SHEET (See instructions)	1. PUBLICATION OR REPORT NO.	2. Performing Organ. Report No.	3. Publication Date

4. TITLE AND SUBTITLE

NBS: Materials Measurements

5. AUTHOR(S)

J. R. Manning

6. PERFORMING ORGANIZATION (If joint or other than NBS, see instructions)

NATIONAL BUREAU OF STANDARDS
DEPARTMENT OF COMMERCE
WASHINGTON, D.C. 20234

7. Contract/Grant No.
NASA Gov't. Order H-27954B

8. Type of Report & Period Covered
Annual Report
April 1, 1982-March 31, 1983

9. SPONSORING ORGANIZATION NAME AND COMPLETE ADDRESS (Street, City, State, ZIP)

Office of Materials Processing in Space
National Aeronautics and Space Administration
Washington, DC 20546

10. SUPPLEMENTARY NOTES

☐ Document describes a computer program; SF-185, FIPS Software Summary, is attached.

11. ABSTRACT (A 200-word or less factual summary of most significant information. If document includes a significant bibliography or literature survey, mention it here)

This report describes NBS work for NASA in support of NASA's Materials Processing in Space Program under NASA Government Order H-27954B (Properties of Electronic Materials) covering the period April 1, 1982 to March 31, 1983. This work is directed toward measurement of materials properties important to the design and interpretation of space processing experiments and determinations of how the space environment may offer a unique opportunity for performing improved measurements and producing materials with improved properties.

The work is being carried out in three independent tasks:

Task 1. Surface Tensions and Their Variations with Temperature and Impurities
Task 2. Convection During Unidirectional Solidification
Task 3. Measurement of the High Temperature Thermophysical Properties of Tungsten Group Liquids and Solids

The results obtained for each task are given in detailed summaries in the body of the report. Emphasis in Tasks 1 and 2 is on how the reduced gravity obtained in space flight can affect convection and solidification processes. Emphasis on Task 3 is toward development of techniques for thermodynamic measurements on reactive materials, requiring levitation and containerless processing.

12. KEY WORDS (Six to twelve entries; alphabetical order; capitalize only proper names; and separate key words by semicolons)

surface tension, convection, directional solidification, thermophysical properties, silicon, tungsten, binary alloy

13. AVAILABILITY

☒ Unlimited
☐ For Official Distribution. Do Not Release to NTIS
☐ Order From Superintendent of Documents, U.S. Government Printing Office, Washington, D.C. 20402.
☐ Order From National Technical Information Service (NTIS), Springfield, VA. 22161

14. NO. OF PRINTED PAGES

15. Price

USCOMM-DC 6043-P80

NBSIR 83-2772

NBS: Materials Measurements

U.S. DEPARTMENT OF COMMERCE
National Bureau of Standards
Washington, DC 20234

August 1983

Annual Report
For the Period 1 April 1982 - 31 March 1983
NASA Government Order C-27884B
Processing of Electronic Materials

NBSIR 83-2772

NBS: MATERIALS MEASUREMENTS

J. R. Manning

U.S DEPARTMENT OF COMMERCE
National Bureau of Standards
Washington, DC 20234

August 1983

Annual Report
For the Period 1 April 1982 - 31 March 1983
NASA Government Order H-27954B
Properties of Electronic Materials

U.S. DEPARTMENT OF COMMERCE, Malcolm Baldrige, *Secretary*
NATIONAL BUREAU OF STANDARDS, Ernest Ambler, *Director*

TABLE OF CONTENTS

National Bureau of Standards
Materials Measurements

Summary

This report describes NBS work for NASA in support of NASA's Materials Processing in Space Program under NASA Government Order H-27954B (Properties of Electronic Materials) covering the period April 1, 1982 to March 31, 1983. This work is directed toward measurement of materials properties important to the design and interpretation of space processing experiments and determinations of how the space environment may offer a unique opportunity for performing improved measurements and producing materials with improved properties.

The work is being carried out in three independent tasks:

Task 1. Surface Tensions and Their Variations with Temperature and Impurities

Task 2. Convection During Unidirectional Solidification

Task 3. Measurement of the High Temperature Thermophysical Properties of Tungsten Group Liquids and Solids

The results obtained for each task are given in detailed summaries in the body of the report. Emphasis in Tasks 1 and 2 is on how the reduced gravity obtained in space flight can affect convection and solidification processes. Emphasis on Task 3 is toward development of techniques for thermodynamic measurements on reactive materials, requiring levitation and containerless processing.

With the advent of the Space Shuttle, it may become feasible to exploit the unique microgravity environment of space flight to produce improved materials and improved measurements of important materials properties. In materials processing on earth, gravity frequently produces

density-driven convection, thereby causing liquids to be stirred as they solidify. This stirring disturbs the quiescent boundary layer at the solidifying interface, and can be very undesirable if nearly perfect crystals are required. For example, it creates interface instabilities, introduces segregation of components and produces crystal defects in the resulting solid material. These defects and inhomogeneities, which are particularly troublesome in electronic technology and other advanced technical applications, might be avoided in materials produced under microgravity conditions.

In Task 1, surface tension and surface segregation effects are being investigated to determine the possible influence of these surface effects on convection and solidification processes. In particular, measurements are being made of the surface tension of liquid silicon. Silicon is one of the most important materials used in electronic technology. Because of the need for fully defect-free material, not readily obtainable under earth-bound conditions where gravity-driven convection can be important, silicon is a major candidate material for space flight processing. Under microgravity conditions, Marangoni convection arising from surface tension gradients could be the main source of fluid flows affecting solidification processes. Thus surface tension information will be important in planning materials processing in space. Because of the high reactivity of silicon, its surface tension is poorly known. Moreover, despite the technological importance of silicon, the dependence of its surface tension on temperature and impurities was really not known at all prior to the current work. This work is designed to provide these surface tension measurements.

In Task 2, solutal convection, which results from simultaneous temperature and composition gradients, and other convective phenomena arising during directional solidification are being investigated both by theoretical calculations and by experiments. The experiments are designed to test the theories and provide quantitative data on convection processes. Direct measurements of convection are being made during unidirectional solidification of transparent materials, particularly succinonitrile containing small amounts of ethanol. The theoretical calculations specifically include determinations of the effects a reduction in gravitational force will have on convection.

Interactions between temperature gradients and composition gradients can make it impossible to avoid solutal convection and other density-driven convection effects during materials processing on earth. Since this type of convection depends on gravity, its effects will be much less pronounced in space. NBS work is directed toward provision of measurements and development of models to define the conditions under which this type of convection will be important and determine how it can be avoided or controlled.

In Task 3, assistance is being provided to a joint project involving investigators from Rice University (Prof. J. Margrave) and General Electric Co. (Dr. R. T. Frost) in which a General Electric electromagnetic levitation facility is being applied to develop levitation/drop calorimetry techniques and determine their possibilities for use in space flight experiments. The critical advantage of such levitation experiments is the avoidance of specimen contamination since in highly reactive materials even slight contact with a container during heating and melting could completely

invalidate the experimental results. Measurements of the specific heat of liquid tungsten uncontaminated by reaction with container walls currently are being pursued in earth's gravity experiments to look at the limitations imposed by gravity in such work. For example, in these experiments, the large electromagnetic forces required to counteract gravity tend to produce instabilities in the liquid droplets. A number of the automated techniques being developed in this work should also be useful for space flight experiments.

Task 1

Surface Tensions and Their Variations with Temperature and Impurities

S. C. Hardy
Metallurgy Division
Center for Materials Science

Introduction

Surface tension gradients produced by temperature or concentration variations on free liquid surfaces result in shear stresses which can in many situations set the fluid into motion. In low gravity materials processing the primary fluid flows are expected to be of this type because buoyancy is greatly reduced. These thermocapillary flows can influence the temperature and solute fields in the bulk liquid and the morphology, microstructure and homogeneity of a solid produced from this liquid. Thus, knowledge of surface tension gradients is essential to the understanding of materials produced from the processes involving free liquid surfaces in low gravity. We are measuring the surface tension of liquid silicon in support of space experiments with this material which are being developed. The results of these measurements will also be of interest for silicon crystal growth research and production on earth.

The temperature and chemical concentration dependences of the surface tensions of many materials are poorly known; for highly reactive, high melting point elements like silicon often only estimates of these parameters can be found in the literature. Thus in a recent computer study of the fluid flow in Czochralski growth of silicon, calculations were performed for values from -0.1 mJ/m^{2}K to -0.4 mJ/m^{2}K for K, the rate of change of surface tension with temperature [1]. The flow was found to vary significantly both in magnitude and distribution for this variation in K. These results

show that accurate surface tension data is essential for meaningful calculations or quantitative interpretation of observed flow phenomena in floating zones of silicon.

The uncertainty in K for silicon stems basically from the lack of systematic measurements of the surface tension over a temperature range. Various workers have measured the surface tension at different temperatures [2, 3, 4]. However, K values calculated from their data are highly inaccurate because systematic errors in the different experiments are sufficiently large to obscure the surface tension differences due to temperature. It is essential in determinations of K to measure the surface tension over a temperature range in the same experiment so that the effects of systematic errors are minimized. This is especially true for silicon because of its extreme chemical reactivity. Liquid silicon dissolves almost all materials to some extent thereby picking up impurities which can surface segregate and significantly lower the surface tension. Thus it must be assumed that most experiments will have unique impurity concentrations.

The only systematic study of the surface tension of silicon over a temperature range that we know of is that of Lukin, et al [5]. The value they found for K is $-0.1\ mJ/m^2K$. Although this is a reasonable value, no details or data are presented. Moreover the density variation with temperature used in their work is significantly different from that generally accepted. Thus it is not possible to make any judgment as to the accuracy of their measurements.

Experimental

We are using the sessile drop technique to measure the surface tension of liquid silicon. This method is based on a comparison of the profile of a liquid drop with the profile calculated by solving the

Young-Laplace equation. The comparison can be made in several ways; we are using the traditional Bashforth-Adams [6] procedure with modern drop shape tables we have calculated which virtually eliminate interpolation errors.

Although we have used the sessile drop technique previously to measure the surface tension of gallium [7], the present experiments require essentially new apparatus because of the high temperatures involved. The melting point of silicon is 1410°C and it is desirable to make measurements to at least 1600°C in order to determine the temperature dependence of the surface tension.

Figure 1 is a schematic diagram of the experimental apparatus. The silicon is contained in a cup which stabilizes the liquid drop and imposes a circular cross section on the drop base, thus reducing errors arising from anisotropic wetting often encountered using flat drop supports. The outside diameter of the cup is used as the length standard in the calculation of the surface tension. The cup and drop are at the center of a cylindrical susceptor which is heated inductively. The quartz jacket enclosing the susceptor and drop connects through an O-ring coupling to a vacuum system consisting of a water cooled baffle and diffusion pump, gauges, valves for admitting gases to the system, and a forepump. Quartz windows at both ends of the tube allow simultaneous photography and temperature measurement of the drop with an automatic pyrometer.

Figure 2 shows the central region of the heating tube in more detail. The cup containing the silicon sits on a tungsten platform which in turn rests on two tungsten rods. These rods extend well out of the susceptor into a much cooler region of the heating tube. They are clamped to a

Young-Laplace equation. The comparison can be made in several ways; we are using the traditional Bashforth-Adams [6] procedure with modern drop shape tables we have calculated which virtually eliminate interpolation errors.

Although we have used the sessile drop technique previously to measure the surface tension of gallium [7], the present experiments require essentially new apparatus because of the high temperatures involved. The melting point of silicon is 1410°C and it is desirable to make measurements to at least 1600°C in order to determine the temperature dependence of the surface tension.

Figure 1 is a schematic diagram of the experimental apparatus. The silicon is contained in a cup which stabilizes the liquid drop and imposes a circular cross section on the drop base, thus reducing errors arising from anisotropic wetting often encountered using flat drop supports. The outside diameter of the cup is used as the length standard in the calculation of the surface tension. The cup and drop are at the center of a cylindrical susceptor which is heated inductively. The quartz jacket enclosing the susceptor and drop connects through an O-ring coupling to a vacuum system consisting of a water cooled baffle and diffusion pump, gauges, valves for admitting gases to the system, and a forepump. Quartz windows at both ends of the tube allow simultaneous photography and temperature measurement of the drop with an automatic pyrometer.

Figure 2 shows the central region of the heating tube in more detail. The cup containing the silicon sits on a tungsten platform which in turn rests on two tungsten rods. These rods extend well out of the susceptor into a much cooler region of the heating tube. They are clamped to a

stainless steel block at one end and rest freely on an identical block at the other end. These steel blocks rest on the walls of the quartz tube. The platform and cup can be moved along the rods and the entire assembly translates inside the quartz tube. This device permits convenient and rapid sample insertion and removal.

The induction heater operates at 450 kHz and has a power rating of 2.5 kW. This has proved adequate for these experiments if the susceptor is insulated sufficiently. The most promising insulation we have tried is zirconia, ZrO_2, because of its low thermal conductivity and outgassing rate. However, the stability of the insulation in conjunction with the susceptor material is critical. In our initial measurements we used zirconia wrapped about a tantalum susceptor. At operating temperature the tantalum reduced the zirconia and generated volatile species according to the following reaction [8]:

$$Ta(s) + ZrO_2(s) = TaO(g) + ZrO(g)$$

Similar reactions can occur with other combinations of insulator and susceptors (9). At present we are using zirconia insulation with molybdenum susceptors. This combination is reported to be non-reacting up to 2200°C [9, 10]. Metallic heat shields cannot be used because the skin depth at 450 kH. is only 0.06 cm. Since the field decays exponentially as the thickness over the penetration depth, a heat shield 0.006 cm thick reduces the field by 10%, a power loss which would be intolerable with our equipment.

The susceptor is constructed of two concentric cylinders of molybdenum with the third, inner cylinder of tantalum because of its lower vapor pressure. The total thickness is about 0.11 cm, which is sufficient to reduce the field to about 14% of the maximum value. Thus the interior of

the susceptor is not field free. This may result in net forces on the sessile drop which will cause distortions. Although we do not have evidence for such distortions, it is desirable to decrease this field penetration.

Because of the very high reactivity of liquid silicon, the choice of cup material is a critical feature of these measurements. Extensive studies of the compatibility of liquid silicon with various materials have been made recently in conjunction with the solar cell program of the DOE. This research suggests that boron nitride is the most promising of a very limited group of materials [11]. Liquid silicon has a contact angle with boron nitride of about 130° [11]. For our purposes a high contact angle is desirable because it minimizes the wetting of the top surface of the cup by the silicon with the attendent distortion of shape. More importantly, silicon does not dissolve boron nitride. Thus the silicon is not grossly contaminated by cup material. The bonding between the silicon and the boron nitride is sufficiently weak to preserve the cup on cooling. Most materials bond strongly to liquid silicon and are cracked by the differential thermal contraction on cooling. Thus the boron nitride cups can be used for many experiments. Although the DOE studies showed that silicon did acquire some free boron when in contact with boron nitride, we do not believe this will have a major effect on our measurements because boron has a higher surface tension than silicon and consequently will not surface segregate. The development of a bulk boron concentration will only increase the surface tension. Studies of the boron silicon system indicate that 1 atomic percent boron will raise

the surface tension of silicon about 25 mJ/m^2, i.e., approximately 3% (5). This would be a very high bulk impurity concentration.

The silicon used in these early experiments is polycrystalline material of six nines purity. The samples are cut from a large boule using a carbide cut-off wheel. After rinsing in water and alcohol, the silicon parallepiped is melted and solidified on a flat boron nitride block to form a button with roughly the shape of a sessile drop. This button is then placed in a boron nitride cup and a sessile drop is formed. The temperature of the silicon is raised to the maximum and the drop is photographed as it is cooled to various temperatures by reducing the power setting of the induction heater.

Results and Discussion

Figure 3 shows the surface tension of liquid silicon as a function of temperature for three different samples. Two sets of data are in good agreement with each other: the third set lies about 40 mJ/m^2 higher than these points. The slopes, however, are nearly the same for the two groupings of data. Linear regression analysis gives slopes of

$$-0.245 \pm 0.012 \frac{mJ}{m^2K} \text{ and } -0.237 \pm 0.025 \frac{mJ}{m^2K}$$

for the lower and higher data respectively where the range is the estimated probable error. Thus our early measurements indicate the variation with temperature of the surface tension of silicon is approximately -0.24 mJ/m^2K. This data was acquired before the construction of the vacuum system; the measurements were made in flowing argon which had been purified by passage over hot titanium. The 40 mJ/m^2 difference in the two sets of data is probably due to a different partial pressure of oxygen in the flowing argon.

It is possible, of course, that the surface tension difference arises from a drop asymmetry which we cannot observe or to bulk contamination with boron. These values of surface tension and the temperature variation of the surface tension should be regarded as preliminary and as a developmental step rather than a quantitative measurement.

We also show in Figure 3 as a dashed line the results of the Russian measurements referred to previously which have only been reported in summary form [5]. This curve is in fair agreement in absolute value of the surface tension with our lower data. However, the temperature variation is -0.1044 mJ/m^{2}K, a value less than half that which we found. Part of the discrepancy is due to the use of different density data. The authors of reference [5] claim to have measured the density and report their results by giving a value for the coefficient K_ρ which occurs in the expression

$$\rho = \rho_{1410} - K_\rho(T-1410).$$

The value of K_ρ for pure silicon they find is 0.1291×10^{-3}gm/cm^{3}K.

We have used in our calculations of surface tension the density measurements of Lucas [12] et al which are reported in detail, are systematic, and in good agreement with less extensive measurements by others. Lucas finds $K_\rho = 0.35 \times 10^{-3}$gm/cm^{3}K, a value significantly different from the Russian work. If the lower K_ρ is used to calculate surface tensions with our drop measurements, the temperature variation of the surface tension is reduced to -0.185 mJ/m^2, a result still significantly higher than that reported in the Russian work.

In summary, we have developed the instrumentation required to measure the temperature variation of the surface tension of silicon. Preliminary

measurements in flowing argon using boron nitride cups to contain the drops suggest that this temperature variation will be near $-0.24\ mJ/m^2K$. In future work we will be making measurements in vacuum and in atmospheres containing controlled concentrations of hydrogen and oxygen in order to determine the sensitivity of the silicon surface tension to oxygen partial pressure. In addition, the effects of other container materials will be investigated. Of particular interest is SiO_2 because of its wide use in industrial silicon crystal growth. Some determination of the impurity content of the silicon after the surface tension measurements is highly desirable to assess the extent to which the silicon is contaminated by contact with the cup. We will characterize our samples using Auger spectroscopy.

References

1. W. E. Langlois, J. Crystal Growth 56, 15 (1982).

2. P. H. Keck and W. Van Horn, Phys. Rev. 91, 512 (1953).

3. Eljutin, Kostikov and Levin, Izv. Vys. Uch. Sav., Tsvetn. Met., 2, 131 (1970).

4. Dshemiler, Popel and Zarevski, Fiz. Metri Met., 18, 83 (1964).

5. S. V. Lukin, V. I. Zhuchkov and N. A. Vatolin, J. of the Less-Common Metals, 67, 399 (1979).

6. F. Bashforth and J. C. Adams, The Theories of Capillary Action, University Press, Cambridge, 1883.

7. S. C. Hardy and J. Fine, Materials Measurements, NBSIR 80-2082, 1 (1980).

8. W. A. Chupka, J. Berkowitz and M. G. Inghram, J. Chem. Phys. 26, 1207 (1957).

9. W. D. Kingery, Property Measurements At High Temperatures, John Wiley and Sons, New York, 1959.

10. The Oxides Handbook, edited by G. V. Samsanov, IFI/Plenum, New York, 1973.

11. T. O'Donnell, M. Leipold and M. Hagan, Compatibility Studies of Various Refractory Materials in Contact with Molten Silicon, DOE/JPL-1012-7716, (1978).

12. L. D. Lucas, Mem. Sci. Rev. Met., 61, 1 (1964).

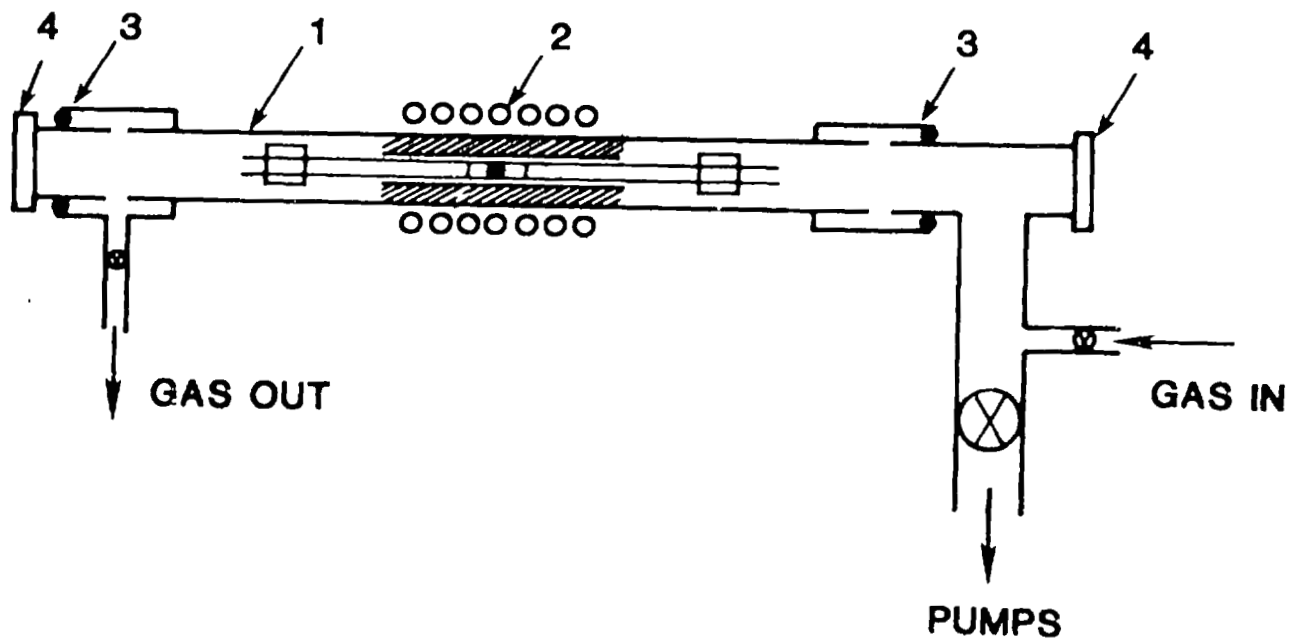

Fig. 1. Schematic diagram of experimental apparatus: (1) quartz tube, (2) induction coil, (3) O-ring seal, (4) window.

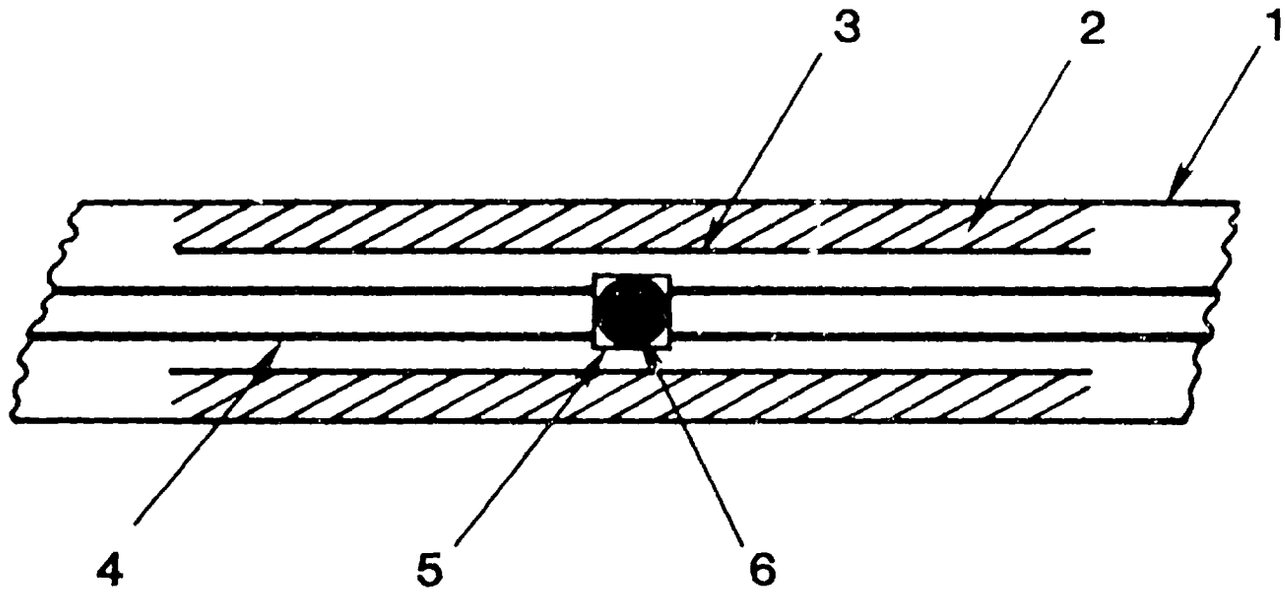

Fig. 2. Schematic diagram of high temperature zone of experimental apparatus: (1) quartz tube, (2) zirconia insulation, (3) molybdenum susceptor, (4) W rods, (5) W tray, (6) BN cup.

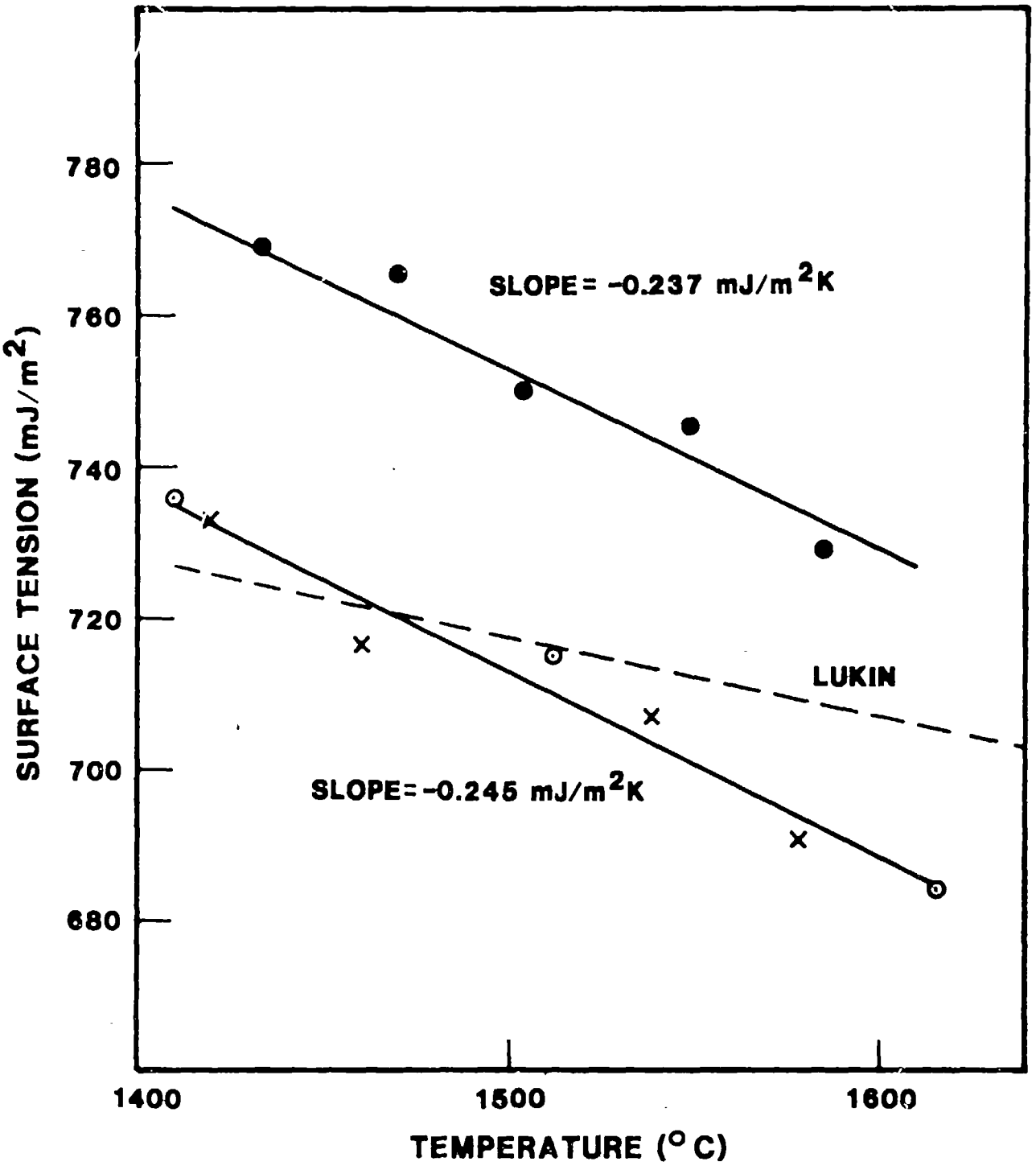

Fig. 3. The surface tension of silicon as a function of temperature (preliminary results).

Task 2

Convection During Unidirectional Solidification

R. J. Schaefer and S. R. Coriell
Metallurgy Division
Center for Materials Science

and

G. B. McFadden and R. G. Rehm
Mathematical Analysis Division
Center for Applied Mathematics

SUMMARY

During solidification of a binary alloy at constant velocity vertically upwards, thermosolutal convection can occur if the solute rejected at the crystal-melt interface decreases the density of the melt. We assume that the crystal-melt interface remains planar and that the flow field is periodic in the horizontal direction. The time-dependent nonlinear differential equations for fluid flow, concentration, and temperature are solved numerically in two spatial dimensions for small Prandtl numbers and moderately large Schmidt numbers. For slow solidification velocities, the thermal field has an important stabilizing influence; near the onset of instability the flow is confined to the vicinity of the crystal-melt interface. For fixed velocity as the concentration increases, the horizontal wavelength decreases rapidly; a phenomenon also indicated by linear stability analysis. The lateral inhomogeneity in solute concentration due to convection is obtained from the calculations. For a narrow range of solutal Rayleigh numbers and wavelengths, the flow is periodic in time.

Experimental observations of unidirectional solidification of succinonitrile containing ethanol have revealed an interaction between convective flow, interface shape, and the localized development of a cellular interface.

The effect is attributed to thermally induced convection and can be modified by changing the thermal field in the interface region.

In collaboration with M. E. Glicksman and Q. T. Fang of Rensselaer Polytechnic Institute, and R. F. Boisvert of the Scientific Computing Division, we have analyzed the stability of the parallel flow between a vertical crystal-melt interface and a vertical wall held at a temperature above the melting point of the crystal. Three modes of instability occur: (1) a buoyant mode, (2) a shear mode, and (3) a coupled crystal-melt mode. For Prandtl numbers greater than approximately two, the coupled crystal-melt mode occurs at a lower Grashof number than the other two modes. These calculations and similar calculations for a cylindrical geometry were motivated by and are in general agreement with recent experiments on succinonitrile at Rensselaer Polytechnic Institute.

Introduction

The general aim of this task is the theoretical and experimental study of the fluid flow and solute segregation which occur during solidification. The nature of the fluid flow, its effect on the shape of the crystal-melt interface and on the resulting distribution of solutes is examined. In particular, the role of solutal convection (gravity driven flow due to solute gradients) during the vertical directional solidification of a binary alloy is considered both theoretically and experimentally.

We present a disscussion of the numerical calculations first and then a description of the experiments: each Section can be read independently. The results of a number of calculations of the fluid flow and concentration field during directional solidification of an alloy with Prandtl number of 0.01 and Schmidt number of 10 are described in the Numerical Results section. The experimental section describes the fluid flow and crystal-melt interface shapes observed during the directional solidification of succinonitrile containing small additions of ethanol.

In an Appendix, we describe a linear stability analysis relevant to experimental work being conducted at Rensselaer Poytechnic Institute. As described in the Appendix an interface instability occurs under conditions for which in the absence of fluid flow, the crystal-melt interface would be morphologically stable.

NUMERICAL RESULTS

The basic equations and methods for calculating the fluid velocity, solute, and temperature fields during directional solidification of a binary alloy vertically upwards have previously been reported [1]. In this report we present the results of a number of numerical computations for an alloy of Prandtl number $P = 10^{-2}$ and Schmidt number $Sc = 10$. In general we will use dimensionless variables; Tables I and II define dimensional and dimensionless quantities, respectively.

The solutal Rayleigh number Rs^* at the onset of convective instability can be determined by linear stability calculations. For convective modes of instability, the results of the linear theory are approximately the same whether the planar crystal-melt interface is allowed to deform or is maintained rigid. The critical solutal Rayleigh number as a function of V/D is plotted in Fig. 1. In these calculations we have kept the imposed temperature gradient in the liquid constant so that $Ra(V/D)^4$ is constant; thus Ra decreases rapidly as (V/D) increases. Previous calculations [2-4] (see e.g. Table 3 of ref. 2) have indicated that as V/D increases the thermal field does not affect the critical solutal Rayleigh number. In fact, Hurle, Jakeman, and Wheeler [4] showed that for sufficiently large V/D the dependence of density on temperature could be completely neglected, i.e., they set the $Ra = 0$, and obtained results in agreement with those of ref. 2, which corresponded to a liquid temperature gradient of 200K/cm. Thus, linear stability theory indicates that for small values of V/D, the thermal field is important while for large values of V/D the thermal field is unimportant.

The different behavior in these two regimes is further illustrated in Figs. 2 and 3. The critical bulk solute concentration C for the onset of instability is plotted as a function of the horizontal wavelength λ for $D/V = 0.015$ and 0.15 cm in Figs. 2 and 3, respectively. The concentration

has been normalized by the minimum concentration C* as a function of wavelength; thus $C/C^* = Rs/Rs^*$. Linear stability theory predicts that the amplitude of a perturbation varies in time as $\exp[\sigma_r(\lambda)t]$. For a given value of $C/C^* > 1$, there is a positive maximum value of σ_r as a function of λ. The wavelength corresponding to the maximum value of σ_r for a given value of C/C^* is indicated by the dashed line in Figs. 2 and 3. For D/V = 0.015, the wavelength corresponding to the maximum growth rate, slowly decreases as C/C^* increases. In contrast, for D/V = 0.15 cm, the wavelength corresponding to the maximum growth rate rapidly decreases as C/C^* increases.

We note that the unperturbed melt density decreases with height if $Rs < kScRa/(P(k-1))$ or $Rs < 429\ Ra$ for the values given in Table II. This inequality holds for all of the non-linear numerical calculations presented in this report. Most of our numerical calculations have been carried out for D/V = 0.15 cm, where linear theory indicates that the thermal field is important and that the wavelength decreases rapidly with increasing solutal Rayleigh number. For $Rs/Rs^* \equiv 1$ we choose the horizontal wavelength as that corresponding to the onset of instability as determined by linear theory. As the solutal Rayleigh number increases, we find that even though we start with a given wavelength, the actual numerical solution has a smaller wavelength, usually one half the original wavelength. We then use this new wavelength as the starting wavelength for calculations at larger solutal Rayleigh numbers. This behavior is illustrated in Fig. 4. For D/V = 0.15 cm, the wavelength at the onset of convection $\lambda_o = 8.06$ D/V. At $Rs/Rs^* \cong 1.62$ and 1.65, the wavelength decreases to $\lambda_o/2$ and $\lambda_o/3$, respectively. At $Rs/Rs^* \cong 3.5$, the wavelength decreases again from $\lambda_o/3$ to $\lambda_o/6$. As will be discussed, the numerical solution may depend on the initial conditions. Over a narrow range of Rs/R we have found time dependent solutions which are indicated by the dashed line in Fig. 4.

Some tests of the numerical code have previously been described [1]. As a further test, we carried out calculations at $\lambda = \lambda_o$ and $Rs/Rs^* = 0.977$ and 1.020 on a (12, 36) grid and found no flow and flow, respectively, in agreement with linear stability analysis.

Figures 5-9 illustrate numerical results for $Rs/Rs^* = 1.29$. In our numerical calculations, we use a dimensionless time, $T_N = t\nu/H^2$. We also define a dimensionless time T_c based on the crystallization velocity, viz., $T_c = V^2t/D$, and note that $T_c/T_N = (VH/D)^2/Sc$. In the absence of convection, the time for the exponential concentration profile in front of the crystal-melt interface to develop is of the order of T_c/k for $k<<1$. Specifically, for $k = 0.3$ the interface concentration reaches 95% of its final value in a time corresponding to $T_c \cong 10.2$ or $T_N \cong 5.9$ for $(VH/D) = 4.17$ as in Figs. 5-9. For $Rs/Rs^* = 1.29$, the time to approach steady state in the flow, solute, and temperature fields corresponds to $T_N \cong 14$ as shown in Fig. 5 in which the maximum value of the stream function is plotted against time. In Figs. 6-7 we show the steady state stream function and concentration respectively as a function of position. At the top boundary, we have assumed that the fluid velocity and perturbed temperature gradient vanish, and have used a mixed boundary condition on the solute concentration, which ensures solute conservation [5]. The top boundary is an artificial boundary, and we would like to place it sufficiently far from the interface so that it does not influence the flow and solute segregation near the interface. From Fig. 6-7 it is evident that the top boundary is having little effect on the flow and solute concentration near the interface. As the solutal Rayleigh number increases, the flow is less confined to the interface and eventually it is not feasible in terms of computational times to move the upper boundary far enough from the interface. As illustrated in Fig. 8, the solute concentration at the crystal-melt interface varies by 60%. The average solute

concentration at the interface deviates by about 3% from the correct value due to the finite mesh (9 x 36) used in the calculation. In Fig. 9 we show the average solute concentration in the liquid as a function of distance from the crystal-melt interface. For comparison, the exponential concentration profile which would hold in the absence of convection is also shown in Fig. 9.

Over a narrow range of Rs/Rs* and $\lambda = \lambda_o/3$, we have found time-dependent solutions. These are shown in Figs. 10-21; the calculations were carried out on a (12 x 72) mesh with (VH/D) = 4.17 and Rs/Rs* = 3.3. Figs. 10 and 11 show the maximum value of the stream function and the average interface concentration in the melt, respectively, as a function of time. The period of oscillation is approximately $\Delta T_N \cong 0.56$ or $\Delta T_c \cong 0.97$, i.e., the interface has moved a distance 0.97 (D/V) during one cycle. The magnitude of the average interface composition oscillation is small, viz. about 1.6%, which is considerably less than the transverse segregation of about 18%. The magnitude of the stream function oscillation is considerably greater. Figures 12-21 show the stream function and concentration as a function of position at various times during one period of the oscillation. It is clear from these figures that the second vertical cell is undergoing the largest oscillation with the stream function varying in magnitude from 0.119 to 0.234. Note that the flow does not reverse in direction; rather these are oscillations superimposed on a base flow. This may explain why linear stability calculations, assuming a motionless base state, have not revealed any time dependent phenomena in this parameter range. We have also observed

that the steady state solution may depend on the initial conditions, i.e., there may be multiple steady states. As initial conditions, we have (1) perturbed a uniform concentration field, (2) perturbed a steady state (exponential) concentration field, and (3) used a solution for a

particular value of Rs as the initial condition for a different value of Rs. In Figs. 22-23, we show the steady state stream function and concentration field, respectively, for $Rs/Rs^* = 3.6$ using the oscillatory solution at $Rs/Rs^* = 3.3$ (see Figs. 10-21) as the initial condition. In contrast, Figs. 24-25 show the steady state stream function and concentration field, respectively, for exactly the same conditions as Figs. 22-23 except that the initial conditions consisted of a perturbed exponential concentration field. For this case, the final solution has one half the wavelength of the initial condition.

In Figs. 26-27, the stream function and concentration field, respectively, for $Rs/Rs^* = 5.03$ and $(VH/D) = 4.17$ are shown. Figs. 28-29 are identical to Figs. 26-27, respectively, except that (VH/D) and the number of mesh points in the vertical direction have been doubled. It is evident in Figs. 26 and 27 that the effect of the upper boundary is not negligible. As can be seen in Fig. 28 with $(VH/D) = 8.33$, the stream function vanishes at a distance of approximately 5.4 (D/V) from the interface. The solute segregation at the interface is about the same in Fig. 27 and 29, viz., 15%.

Figures 3-29 were for $D/V = 0.15$ cm; in Figs. 30-33 we show the results of a calculation for $D/V = 0.015$ cm, $Rs/Rs^* = 1.325$ and $Ra = 0.127$, corresponding to the same temperature gradient as in Figs. 3-29. As previously discussed, we do not expect the temperature field to stabilize the flow since the Rayleigh number is very small. As shown in Figs. 30-31, even though we have taken $H = 20$ (D/V), the flow is influenced by the upper boundary, and is certainly not confined to the vicinity of the crystal-melt interface. There are clearly fairly large lateral solute gradients far from the interface. Fig. 32 shows the solute concentration at the crystal-melt

interface; the solute segregation is about 60%. The average solute concentration as a function of distance from the interface is compared with the solute profile in the absence of convection in Fig. 33. The average interface concentration and the average concentration gradient at the interface are determined by the boundary conditions, and are independent of the fluid flow as can be seen from Fig. 33. However, at about 2 D/V from the interface, the average solute concentration with convection is about 40% higher than the unperturbed (convectionless) concentration. Since the Rayleigh number was small for the results of Figs. 30-33, we carried out an identical calculation with Ra = 0 to determine whether the thermal field can be completely neglected. The maximum value of the stream function was 80% larger for Ra = 0 than for Ra = 0.127 indicating that the thermal field plays a role even for Ra as small as 0.127.

The numerical results presented here provide insight into the solutal convection which can occur during directional solidification. The range of parameters which can be studied is severely limited by the computational times required for these calculations. Results for different values of the distribution coefficient and temperature gradient in the liquid would be desirable. We have limited the calculations to a Schmidt number of ten, which is appropriate for semiconductors. The time to reach steady state appears to be proportional to the Schmidt number for large Schmidt numbers so that calculations for metallic melts with Schmidt numbers of the order of 100 will take ten times as much computer time. The interaction of the solutal convection, which is driven by the adverse concentration gradient near the crystal-melt interface, with the thermal convection due to horizontal temperature gradients in a real furnace is an important area for further research.

EXPERIMENTAL

Background

Succinonitrile containing ethanol provides a useful system for the investigation of thermo-solutal effects during solidification. The density of ethanol being significantly less than that of succinonitrile, unidirectional upward solidification in this system leads to solute distributions which are predicted to be unstable with respect to convective perturbations. We previously determined the succinonitrile-rich end of the phase diagram for this system and, on the basis of the measured phase diagram parameters and the published physical properties of succinonitrile, predicted the critical concentration of ethanol in succinonitrile above which instability occurs, as a function of the velocity of upward solidification. The predicted instabilities are either interfacial, in which case the wavelength is short and the shape of the solid-liquid interface deviates from planarity, or convective, in which case the wavelength is longer and the liquid above the interface starts to flow. At a fixed temperature gradient, the concentration of ethanol required to produce interfacial instability decreases with increasing solidification velocity, while the concentration required to produce convective instability increases with increasing solidification velocity. At some compositions, there therefore exists a range of solidification velocities in which unidirectional upward solidification is predicted to be stable; above this velocity range interfacial instability is predicted and below this velocity range convective instability is predicted.

Our experimental observations of solidification processes in the region of these transitions have used both pure succinonitrile and succinonitrile doped with an appropriate concentration of ethanol to

investigate the behavior when a finite range of stable velocities is predicted. Because of the low solute distribution coefficient for ethanol in succinonitrile ($k \approx 0.044$), concentrations of interest are very low ($2 - 5 \times 10^{-3}$ wt.% ethanol) and the samples were thus made from ultra-purified succinonitrile and sealed under vacuum.

Perfectly uniform upward solidification of a substance with a normal thermal expansion coefficient (i.e., one which expands with increasing temperature) is convectively stable if no solutes are present. The convective instability predicted for the succinonitrile-ethanol system arises from the rejection of the lower-density solute by the advancing interface. In a real experiment, however, there are sources of convection which may be described as purely thermal and which interfere with observation of the effects predicted for truly unidirectional solidification. Any factor which causes the isotherms in the liquid to deviate from horizontal planes will be a driving force for convective flow.

There are two important causes for thermally induced fluid flow in the liquid above a solidifying interface when unidirectional solidification of a material in a tubular container is attempted by drawing the container downward through a temperature gradient. First, heat losses or gains through the container walls to the furnace or outside environment necessarily imply the presence of a radial component in the temperature gradient. These must be minimized by design of the crystal growth apparatus and by control of the interface position. The second origin for thermally induced convective flow is the distortion of the isotherms by the container walls. When no solidification is taking place, there is a gradient discontinuity at the solid-liquid interface due to the different

thermal conductivity of the solid and liquid. Because this gradient discontinuity is not present in the container walls, the isotherms in the region where the interfce meets the walls must be distorted from planarity. Succinonitrile is unusual in that the thermal conductivity of solid and liquid are, within experimental uncertainty, equal, so that at zero solidification velocity this effect is not important. When solidification starts, however, a gradient discontinuity is produced at the solid-liquid interface by the emission of latent heat of fusion. The heat emitted per unit area of the interface is vL where v is the velocity and L is the latent heat (4.7×10^7 J/m^3 for succinonitrile). Because in a typical experiment the discontinuity produced by this latent heat is not negligible compared to the externally imposed gradients, a significant thermal field distortion is produced by the container walls.

For the unidirectional solidification of metals it is often possible to use containers having much lower thermal conductivity than the metal, in which case the thermal distortions caused by the container walls will be small. However, lateral heat losses to the environment can be large in metallic systems due to the high melting temperatures. For an organic material such as succinonitrile, however, the thermal conductivity of the container cannot be much lower than that of the material and container wall effects are unavoidable. Radial heat losses to the environment, however, can be small because of the low melting temperature. Thus distortion of the isotherms may be similar in metallic and organic systems, although the most important cause of the distortion may differ.

In our experiments we have investigated the effects of radial gradients on "unidirectional" upward solidification under conditions close to those predicted to result in solute-induced interfacial or

convective instability, and have investigated methods to reduce the effects of radial gradients. We have also measured densities of succinonitrile-ethanol mixtures because earlier calculations were based on estimated values.

Experimental Methods

a. Density Measurements

The density of pure liquid succinonitrile and succinonitrile containing four different concentrations of ethanol (up to 6.67 wt.%) was measured by determining the temperatures at which calibrated standards with densities of 0.9700, 0.9800, and 0.9850 had neutral bouyancy. Distilled succinonitrile was used and measurements were carried out under air at atmospheric pressure. The temperature of neutral bouyancy was determined to within 0.1°C.

b. Convective Flow During Unidirectional Solidification

Pure succinonitrile and succinonitrile-ethanol samples are contained within borosilicate glass tubes 19 mm in diameter and approximately 50 cm long. The residual impurity content of the succinonitrile samples, before doping with ethanol, was found to be equivalent to approximately 10^{-4} wt.% (1ppm) of ethanol, in terms of its effect on the solidus and liquidus temperatures. Most experiments were carried out on a sample containing 2.6×10^{-3} wt.% ethanol.

To produce solidification, the sample tubes are drawn downward through a temperature gradient established by a thermostatically controlled lower cold water jacket and an upper heater which is either a similar hot water jacket or an electric heater. Growth velocities can be from 0.4 to 10 μm/s.

An important constraint for these experiments is the requirement of good visibility in the interface region. This can be attained only if the cylindrical tube is surrounded in the interface region by a medium with a refractive index similar to that of the succinonitrile, but which itself has a flat outer wall for microscopic observation. The best image is obtained if the index-matching medium is a fluid contained in a flat-walled outer container, but such a system could also undergo convective processes which would tend to perturb the temperature field within the solidification tube.

We have therefore surrounded the interface region of the solidification tube with close-fitting transparent solid pieces with flat outer windows. Heaters have been incorporated into these pieces in the region of the solid-liquid interface to provide control over the isotherm shape within the sample tube. The heaters are in the form of a flat (pancake-like) coil so that they can duplicate in the transparent solid the temperature discontinuity existing in the sample at the solid-liquid interface. The required heater power is proportional to the velocity of motion of the sample: for a velocity of 1 μm/s, a heater power of about 0.5 W is appropriate.

The sample tube is photographed from the side by a horizontally mounted microscope. To measure convective flow, small neutrally bouyant latex particles are incorporated into the sample. These are photographed using a triple flash exposure with unequal intervals between the flashes, to allow determination of the direction of particle motion. The particles are seen only in dark field illumination, but the interface shape is seen better in bright field illumination.

Results

a. Density

The measured densities of succinonitrile-ethanol solutions are shown in Figure 34. The measured densities are close to those which are calculated under the assumption that no change of total volume takes place when the two components are mixed, although a deviation from this behavior might have been expected on the basis of the liquid-phase miscibility gap in the succinonitrile-ethanol system. The lines of constant density lie almost exactly parallel to the liquidus line in the composition and temperature range which was measured. The density of the liquid at the liquidus is thus constant, 0.9880 g/cm^3. This leads to the unusual result that the liquid at the surface of a succinonitrile crystal growing into a succinonitrile-ethanol mixture has a constant density, no matter what the shape of the crystal, so long as the ethanol concentration does not exceed approximately 7 wt.%. Liquid not immediately at the surface, however, is not constrained to be at the liquidus and therefore has a variable density.

The measurements indicate a concentration dependence of liquid density $\alpha_c = -(\partial\rho/\partial c)/\rho = 2.7 \times 10^{-3}$ $(wt.\%)^{-1}$ which is close to the value used previously $(3.07 \times 10^{-3}$ $(wt.\%)^{-1}$.

b. Convective Flow During Unidirectional Solidification

When the succinonitrile sample is held stationary in the directional solidification apparatus, the solid-liquid interface is horizontal and very slightly concave upwards. The amount of this concavity, which probably results from a small radial heat loss, depends upon the position of the interface between the hot and cold jackets, the nature of the surrounding medium, and other details of the growth apparatus design. A

concave interface indicates that the liquid in the center of the tube is warmer than that near the wall at the same level. Therefore, as expected, there is an upward flow of liquid in the center and a downward flow closer to the walls, with the liquid immediately above the solid-liquid interface moving radially inward. The upward flow velocity at the tube center is typically 10 μm/s. The only microstructural features present at the interface in either pure or ethanol-doped samples are faint grooves due to grain boundaries or sub-boundaries.

When solidification is produced by drawing the sample tube downward, the solid-liquid interface becomes strongly concave in either pure or ethanol-doped succinonitrile. Simultaneously there is a substantial increase in the velocity of upward flow at the tube center (to about 40 μm/s for a growth velocity of 2 μm/s). The pattern of the flow remains unchanged.

These flow velocities are sufficiently large that they can be expected to seriously distort the solute distribution in the liquid above the solid-liquid interface. It was found, however, that the pancake-shaped auxiliary heater surrounding the interface region could be effective at altering this flow pattern.

When the auxiliary heater is not used, the convective flow can result in a transient macroscopic interface shape change which then leads to a localization of interfacial instabilities. The sequence of events which constitute this phenomenon is as follows:

a. The interface is equilibrated in its almost planar configuration at zero growth velocity.

b. Growth is started at a velocity somewhat less than that which is expected to produce interfacial instabilities.

c. The interface becomes concave upwards as a result of the heat flow effects mentioned above.

d. Following an incubation time which depends on the growth velocity, an additional deeper depression develops in the center of the concave interface. The size and shape of this depression also depends on the growth velocity.

e. The depression deepens rapidly and interfacial instabilities develop within it.

f. The cellular interface within the depression advances rapidly and catches up to the general contour of the concave interface.

g. The concave interface then propagates at steady state with a central cellular region in the area where the depression had been.

The incubation time for development of the depression is longer at lower growth velocities. At 1 μm/s, the depression has not been observed, and the interface remains bowl-shaped but smooth (no interfacial instabilities). At 2 μm/s the conditions for formation of the depression are apparently marginal and the incubation time in different runs was found to be between 26 and 125 minutes. At a growth velocity of 3 μm/s the incubation time was 13 to 15 minutes. At 4 μm/s the incubation time becomes more difficult to define because of shape changes (see below) which make the pit less distinct from the overall concavity of the interface.

The transient interface pit takes its most dramatic form under the most marginal conditions for its formation. Thus in the 2 μm/s run in which the pit took 125 minutes to develop, the pit was very deep, narrow,

and pointed before a cellular structure developed near its bottom and spread upwards along the walls (Figure 35 a). At faster growth rates, or when the growth conditions at 2 μm/s were somewhat different and the pit formed more rapidly, the pit was broader, shallower, and more rounded when the cellular structure developed within it (Figure 35 b). After the cellular interface formed within the pit, cells spread rapidly up the sides of the pit as far as the point where the pit merged into the overall bowl-shaped interface. The pit region then filled in rapidly with cellular material until the leading edge of this material was essentially coincident with the overall bowl-shaped contour of the interface. Figure 36 shows the development of the pit in a run at 2 μm/s. The position, relative to a fixed point in the apparatus, of the bottom of the pit is shown: after the cellular substructure develops, the position of the first solid (the leading edge of the cells) and the last liquid (the last entrained intercellular liquid) are shown.

After the development of the cellular interface in the central pit, the convective flow pattern in the liquid above this region is different. Many particles are seen indicating fluid flow downward into the central cellular interface. The flow appears to be less regular than the simple pattern which prevails before the cells develop, but we have not yet discerned its detailed structure.

When the auxiliary heater surrounding the interface is activated, the formation of the central pit can be suppressed. Ideally, the heater would be located exactly at the interface level and would transfer heat uniformly to the sample container walls from all sides. In practice it is difficult to arrange that the interface lies exactly in the plane of the heater because the vertical position of the interface is affected by many

factors including the growth velocity and the auxiliary heater power. Circumferentially uniform transfer of heat to the container walls can also only be approximated. Nonetheless, auxiliary heaters are very effective at changing the convective flow pattern and eliminating the central pit.

As an example, on one run at 2 μm/s a central pit developed 33 minutes after the start of growth and the interface within the pit then became cellular. The auxiliary heater was then turned on and its power level adjusted to give, as closely as possible, a flat interface near the walls of the sample tube. After approximately 30 minutes, the central cellular region of the interface had disappeared. The interface at this point was relatively flat but tilted to one side: the convective flow in the liquid was downward on one side of the tube (where the tilted interface was higher), across the tube above the interface, and upward on the opposite side (where the interface was lower). Similarly, if growth is started when the heater is activated to an appropriate level, the central pit does not develop.

Discussion

These experiments have demonstrated the importance of a previously unrecoreded interaction between convective flow, interface shape, and the development of cellular interfaces. As observed in the succinonitrile-ethanol system, the effect occurs over a small range of growth velocities, but this range of growth velocities is an important one because it represents the conditions which might be chosen for an attempt to grow a crystal of homogeneous, cell-free material. The predicted velocity for

interfacial instability in the system used for these experiments is approximately 10 μm/s (depending on the value of the temperature gradient, which is close to 10 K/cm), and the interactive effects were observed at growth velocities of 2 to 4 μm/s. In addition to being limited to a narrow velocity range, the effect is transient in nature, with the result that the evolution of interface shapes by this process will not be understood if observations are not sufficiently frequent.

Figure 37 summarizes the nature of these interactions in pure and solute-doped systems. At zero growth velocity, the solid-liquid interface in either system can be planar and horizontal. When solidification occurs, the thermal effect of the container walls results in a concave solid-liquid interface and a convective flow pattern in which the liquid above the solid-liquid interface sweeps radially inward and then up along the tube center.

In the pure material, the interface remains smooth and bowl-shaped. If solute is present, the radial inward flow redistributes the solute rejected by the interface and the concentration at the interface is highest in the central region. The resultant local depression of the melting point in this region causes the formation of the pit, which becomes progressively deeper as the geometry for diffusive and convective removal of solute becomes less favorable.

The absence of the pit in the pure system, and the fact that the pit formation can be suppressed by the auxiliary heaters, both support the interpretation that the pit formation is the result of lateral redistribution of solute at the solid-liquid interface. Formation of a macroscopic pit is possible only if the interface does not immediately become morphologically unstable, and the observed velocity dependence meets this condition.

Table 1. Definition of symb used for physical quantities.

ν (kinematic viscosity)

κ (thermal diffusivity of melt)

κ_s (thermal diffusivity of crystal)

D (diffusion coefficient of melt)

g (acceleration of gravity)

α (thermal coefficient of expansion of melt)

α_c (solutal coefficient of expansion of melt)

k_L (thermal conductivity of melt)

k_s (thermal conductivity of crystal)

k (distribution coefficieut)

C_∞ (bulk concentration of solute)

C_∞^* (bulk concentration corresponding to onset of convection)

G_L (temperature gradient in melt)

H (melt height)

V (crystal growth velocity)

λ (horizontal wavelength)

t (time)

Table 2. Dimensionless quantities used in calculations (unless otherwise specified)

Ratio of Thermal Conductivities	$k_L/k_S = 1.0$
Ratio of Thermal Diffusivities	$\kappa/\kappa_S = 1.0$
Distribution Coefficient	$k = 0.3$
Schmidt number	$Sc = V/D = 10.0$
Prandtl number	$P = V/\kappa = 0.01$
Thermal Rayleigh number	$Ra = (g\alpha G_L/V\kappa)(D/V)^4 = 1268.$
Critical solutal Rayleigh number	$R_S^* = (g\alpha_c C_\infty^*/VD)(D/V)^3 = 963.$
Dimensionless Crystal Growth Velocity	$VH/D = 4 - 20$
Ratio of solutal Rayleigh number,	$Rs = (g\alpha_c C_\infty/VD)(D/V)^3$,
to critical solutal Rayleigh number	$Rs/R_S^* =$ VARIOUS VALUES
Ratio of melt height to horizontal wavelength	$H/\lambda =$ VARIOUS VALUES

References

1. R. J. Schaefer, S. R. Coriell, R. G. Rehm, and G. 3. McFadden, NBSIR 82-2560, (ed. by J. R. Manning) p. 25 (1982).

2. S. R. Coriell, M. R. Cordes, W. J. Boettinger, and R. F. Sekerka, J. Crystal Growth 49, 13 (1980).

3. R. J. Schaefer and S. R. Coriell, in Materials Processing in the Reduced Gravity Environment of Space, ed. by Guy E. Rindone (Elsevier, 1982) p. 479.

4. D. T. J. Hurle, E. Jakeman, and A. A. Wheeler, J. Crystal Growth 58, 163 (1982).

5. S. R. Coriell, R. F. Boisvert, R. G. Rehm, and R. F. Sekerka, J. Crystal Growth 54, 167 (1981).

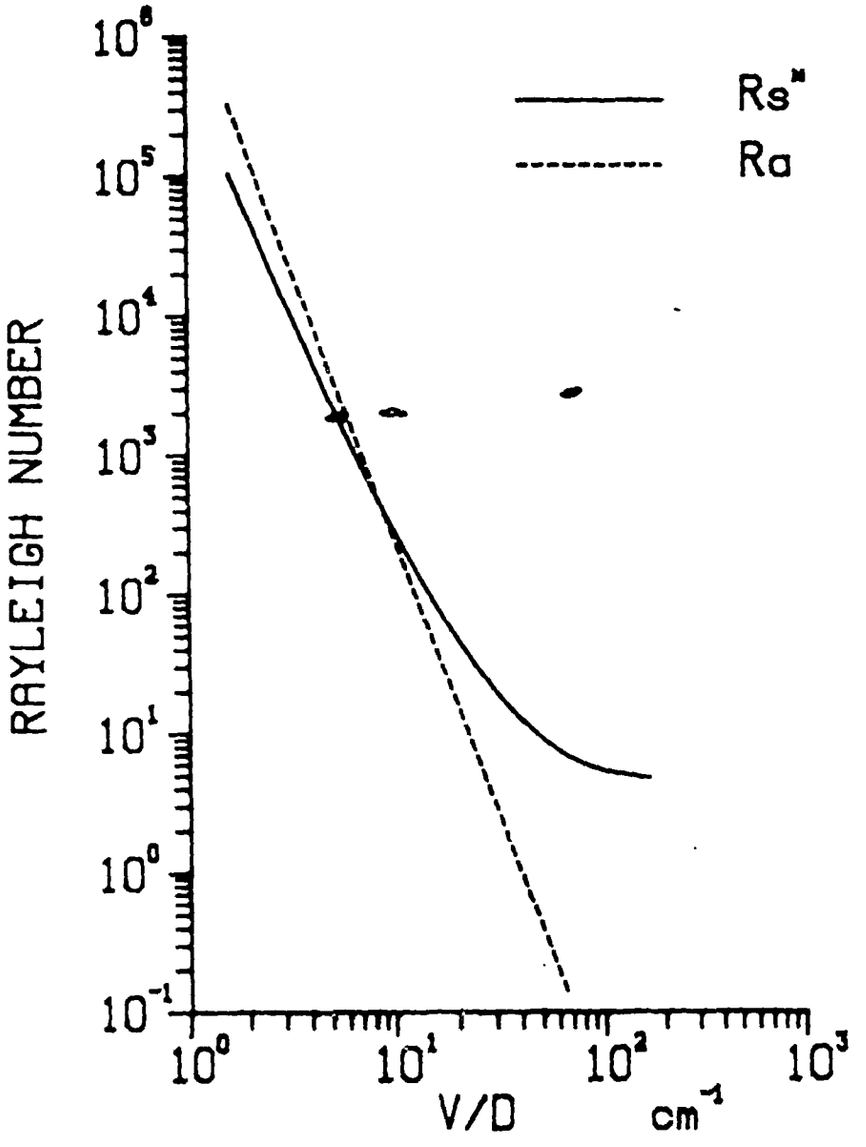

Fig. 1. The solutal Rayleigh number, Rs, at the onset of convection as a function of the ratio of interface velocity, V, and the diffusion constant, D. The temperature gradient in the melt was kept constant so that the thermal Rayleigh number, Ra, varies as the inverse fourth power of V/D. The values of the other parameters are given in Table 2.

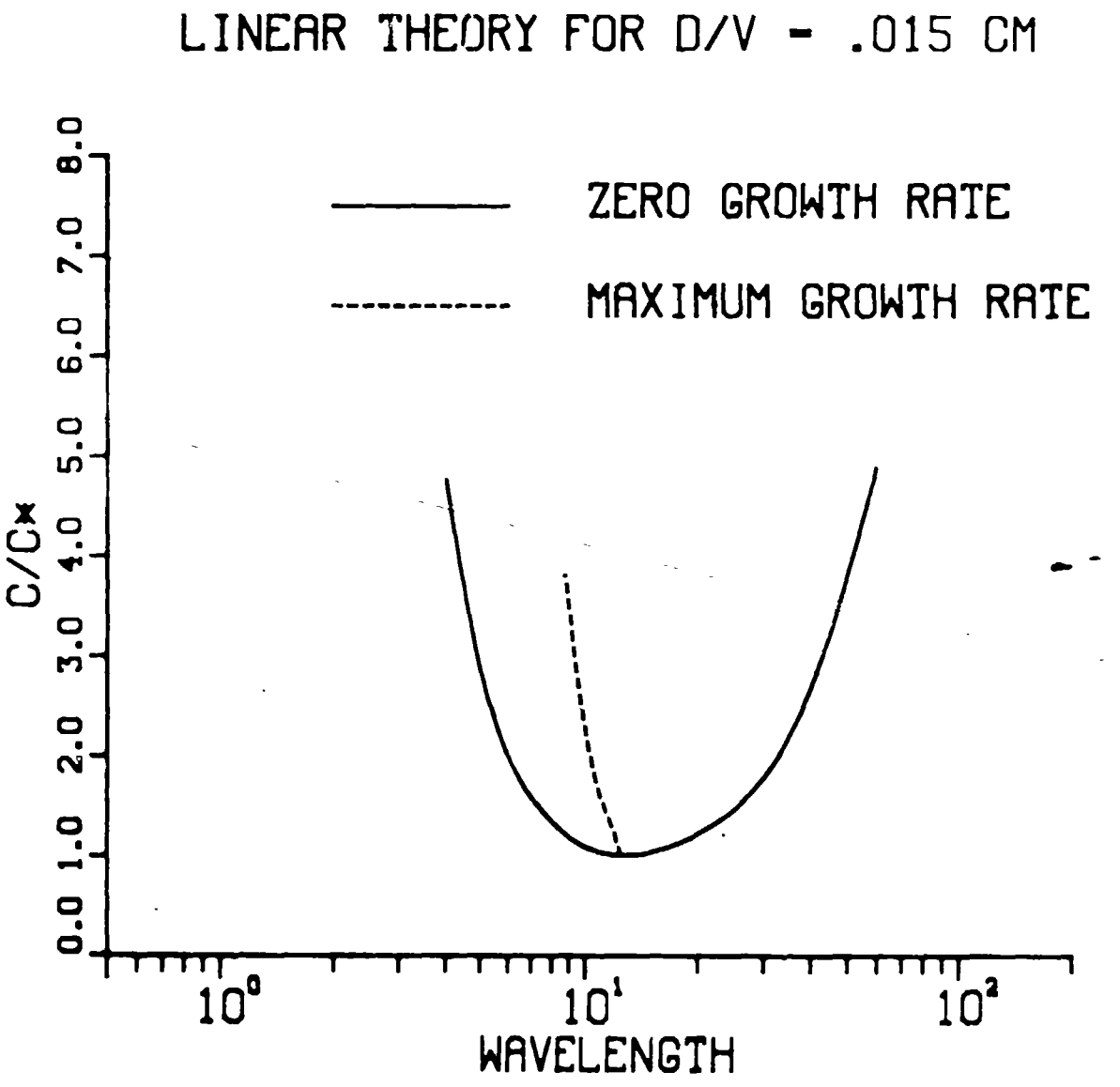

Fig. 2 The normalized critical bulk solute concentration, C, at the onset of convection as a function of the horizontal wavelength (in units of D/V = 0.015 cm.) of a sinusoidal perturbation. The wavelength corresponding to the maximum growth rate of the perturbation is indicated by the dashed line.

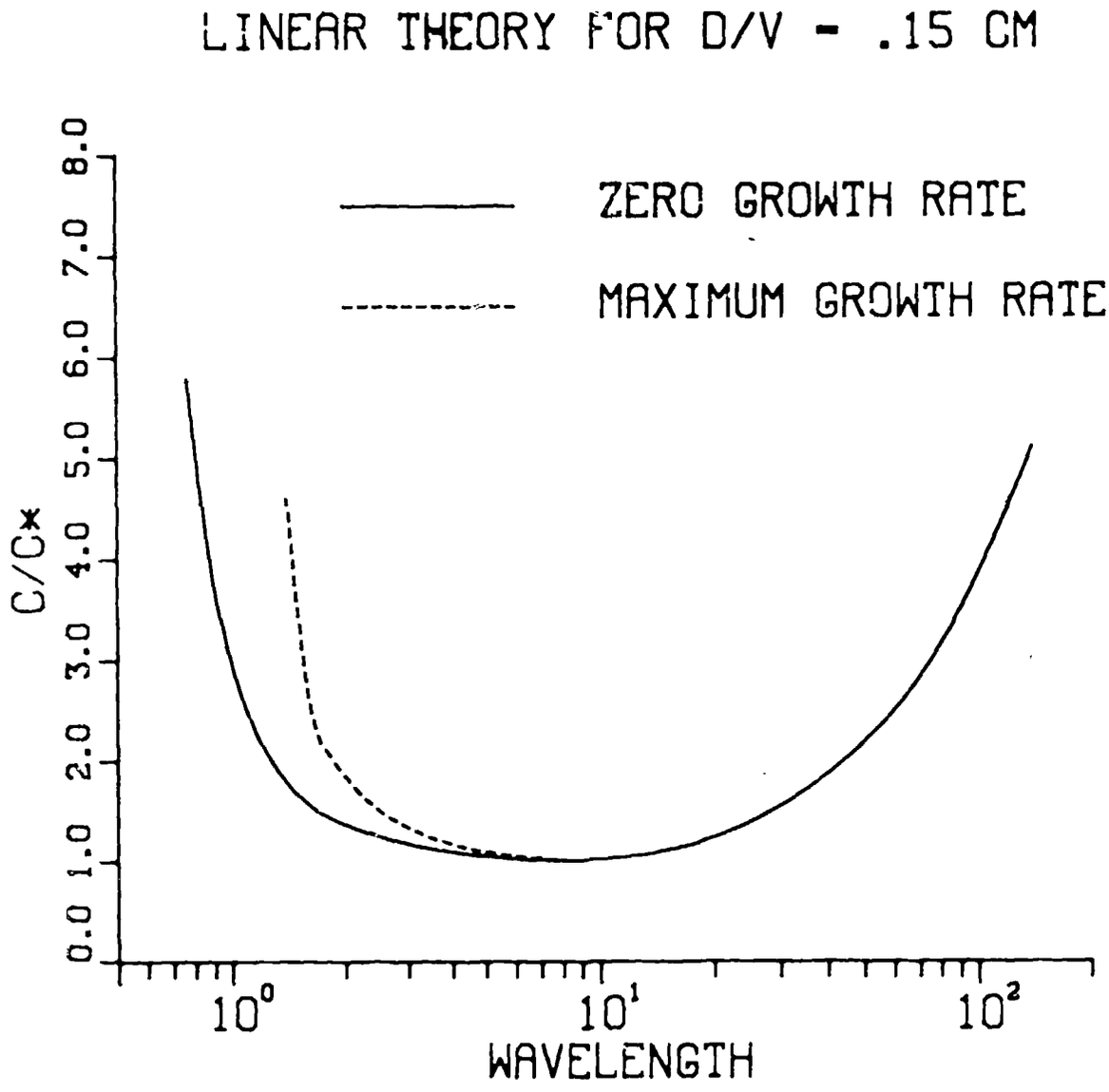

Fig. 3. The normalized critical bulk solute concentration, C, at the onset of convection as a function of the horizontal wavelength (in units of D/V = 0.15 cm.) of a sinusoidal perturbation. The wavelength corresponding to the maximum growth rate of the perturbation is indicated by the dashed line.

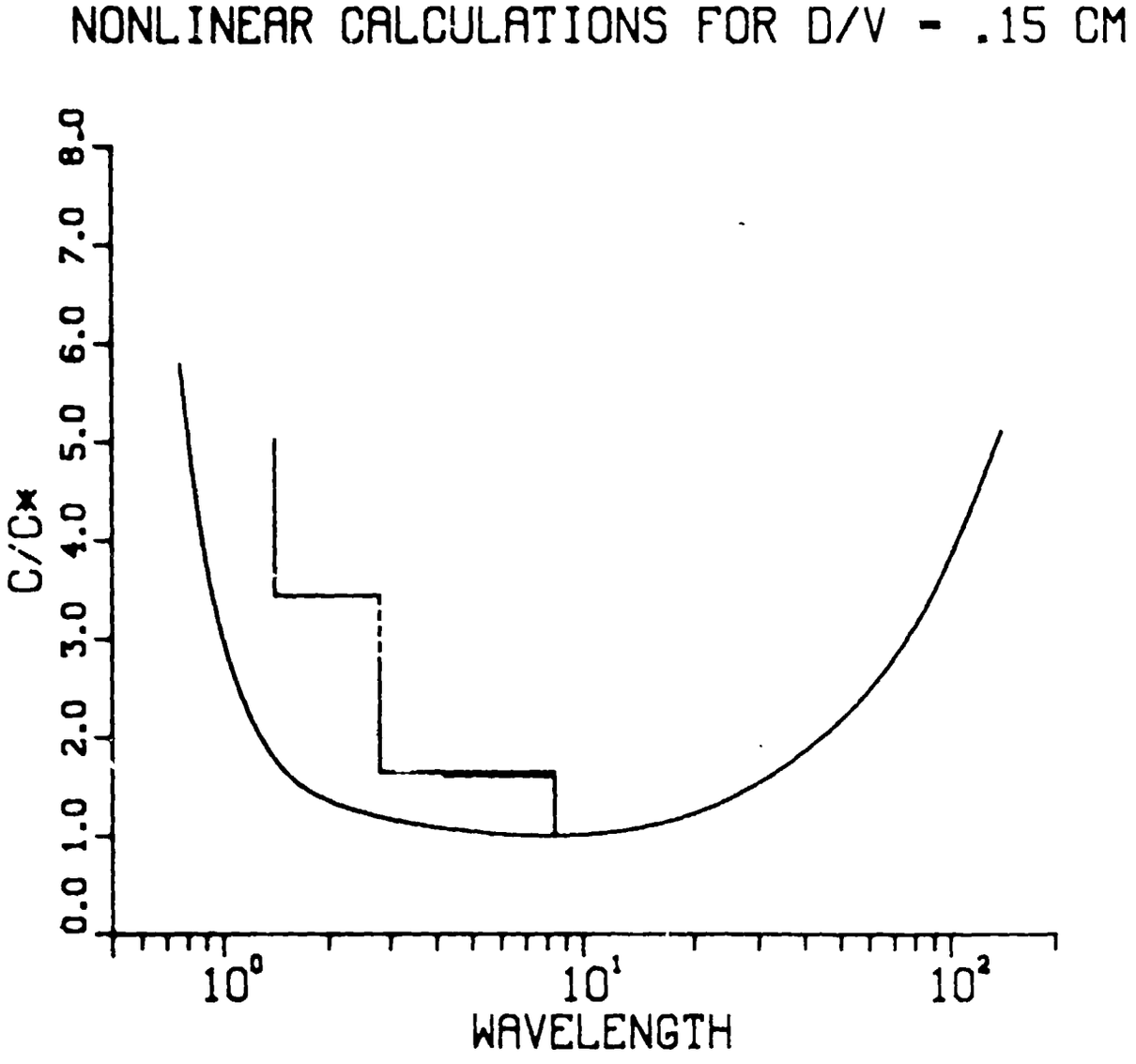

Fig. 4. The vertical lines indicate the wavelengths and solute concentrations for which numerical calculations were carried out. The horizontal lines indicate values of solute concentrations for which the wavelength decreases. The solid curve is the same as in Fig. 3.

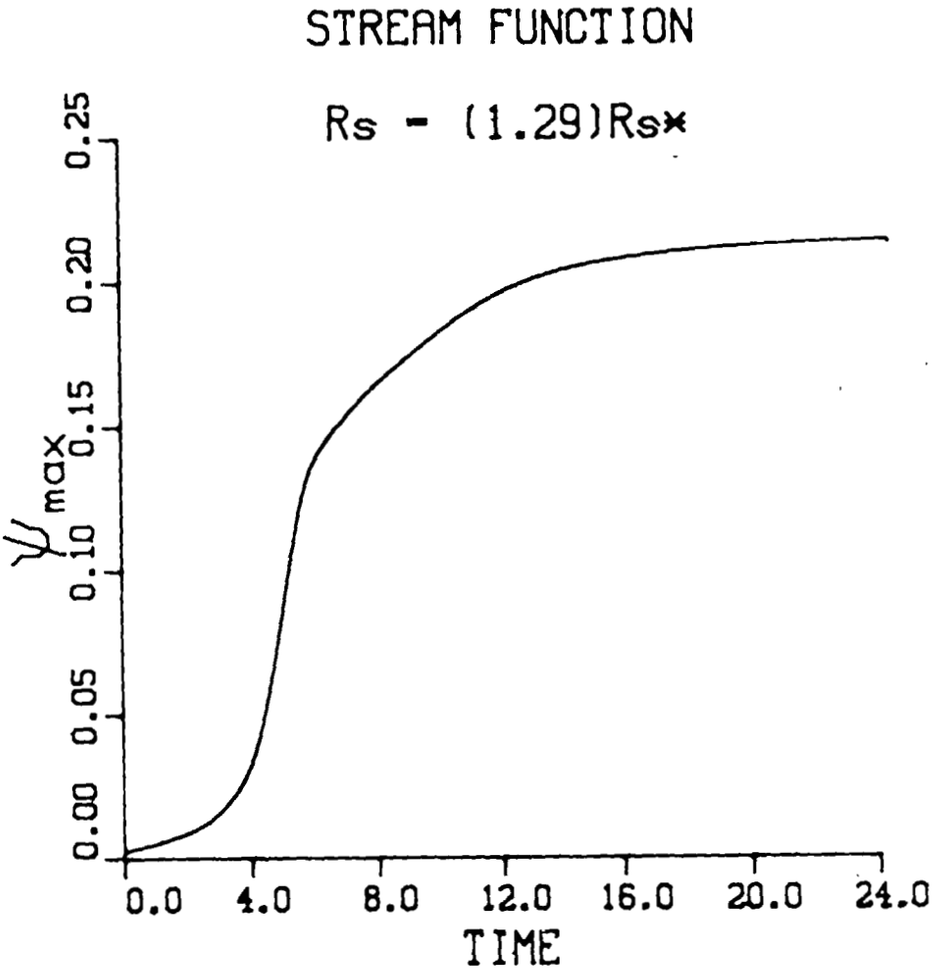

Fig. 5. The maximum of the stream function as a function of time (in units of H^2/ν) for $Rs/R\bar{s} = 1.29$, $VH/D = 4.17$, and $H/\lambda = 0.517$. The values of the other parameters are given in Table 2.

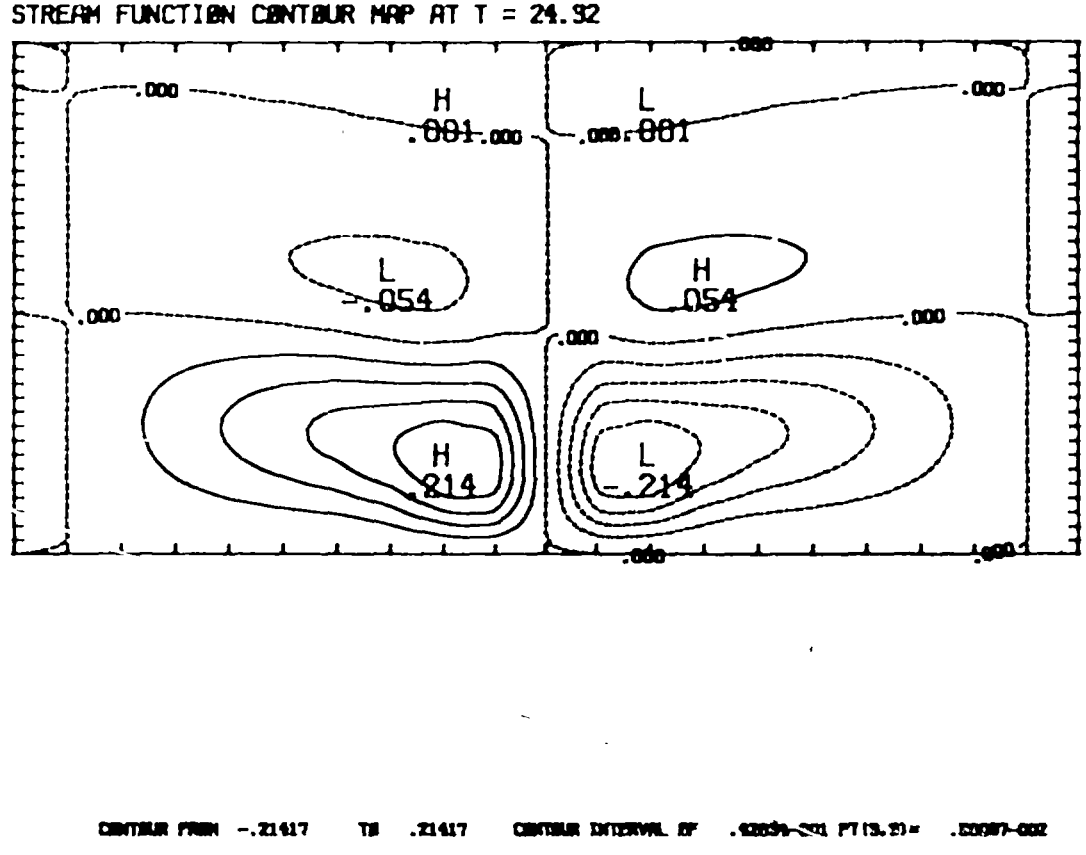

Fig. 6. The steady state stream function as a function of position for the same parameters as in Fig. 5. Each vertical and horizontal division indicates the mesh used in the numerical calculations; although the calculation is done for one half wavelength in the horizontal direction, slightly more than one wavelength is shown.

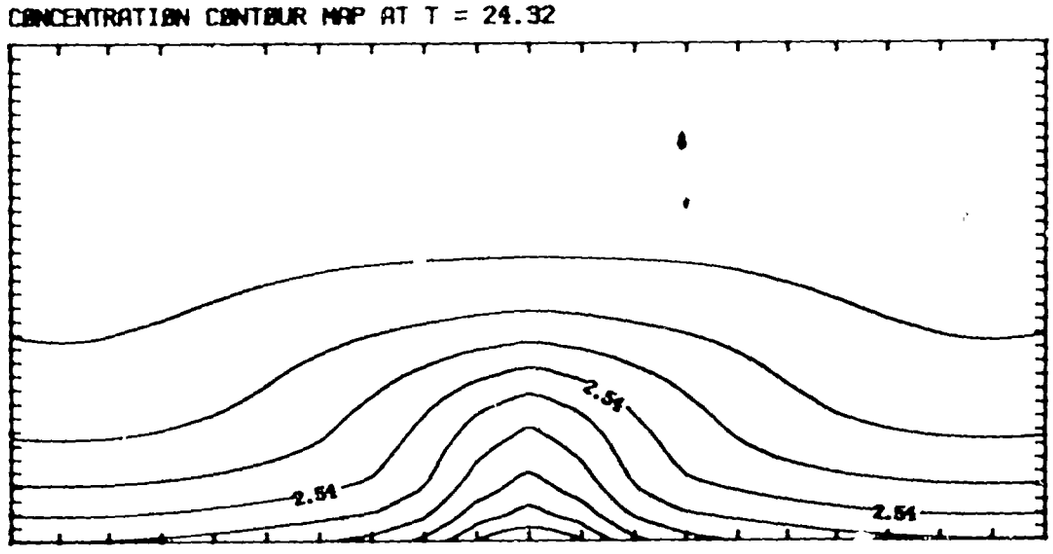

Fig. 7. The steady state concentration as a function of position for the same parameters as in Fig. 5.

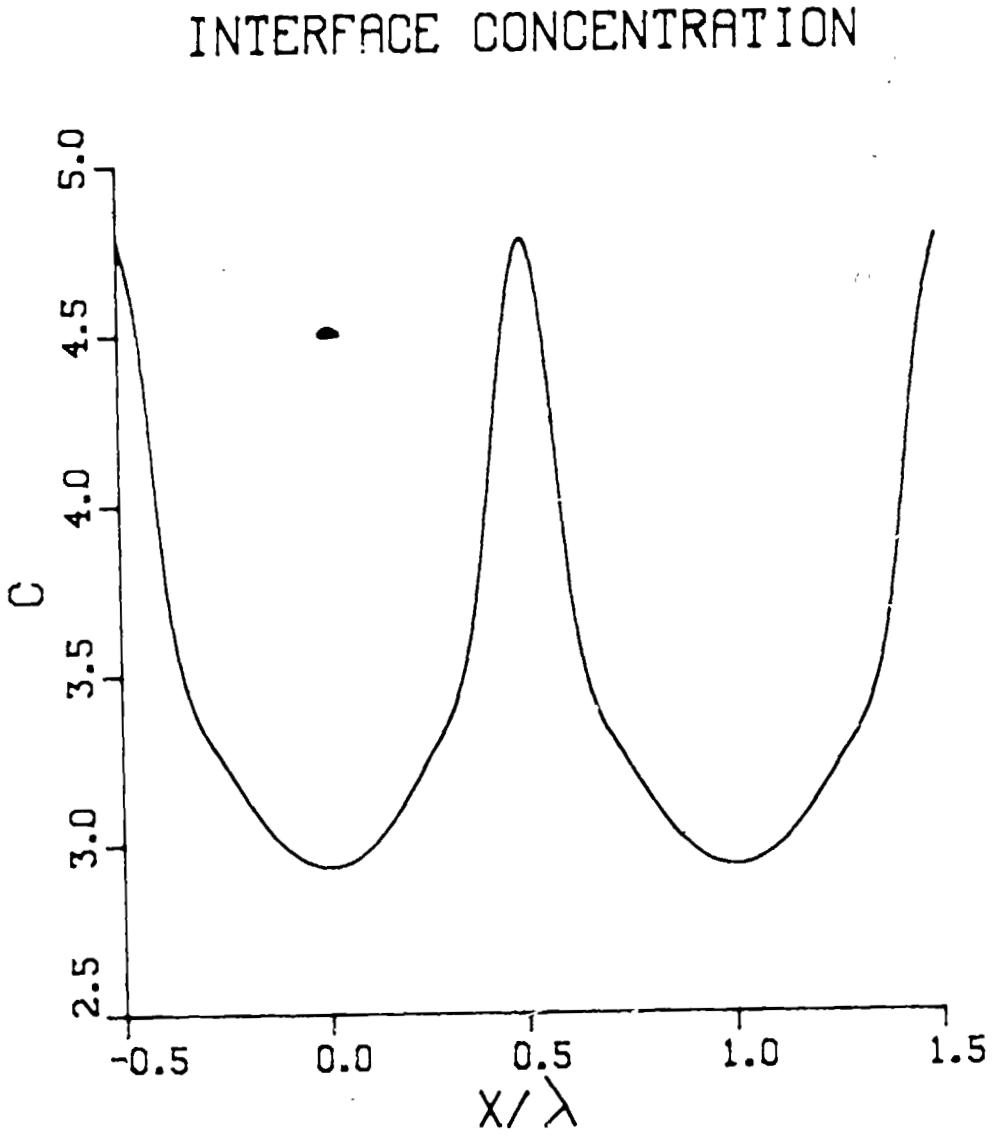

Fig. 8. The steady state interface concentration in the melt for two wavelengths in the lateral direction for the same parameters as in Fig. 5.

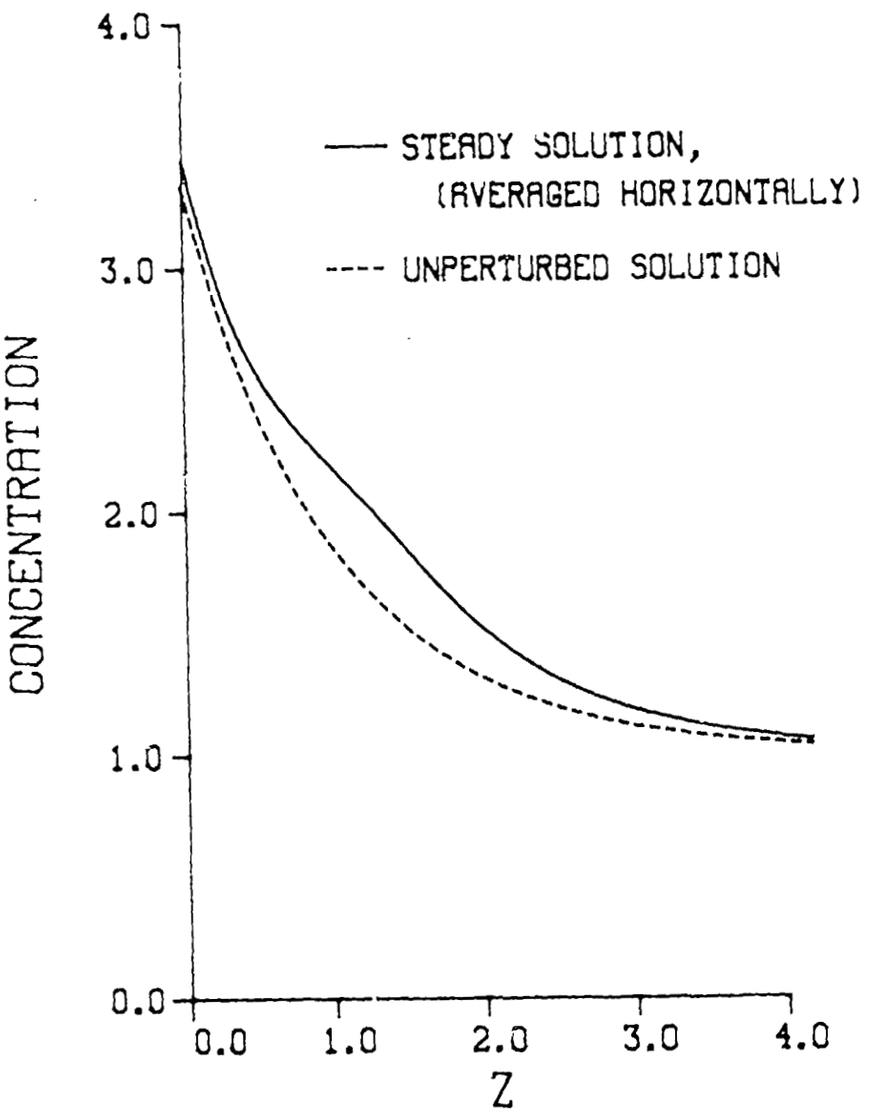

Fig. 9. The average steady state concentration in the melt as a function of the distance (in units of D/V) from the crystal-melt interface for the same parameters as in Fig. 5. The dashed line indicates the concentration in the absence of convection.

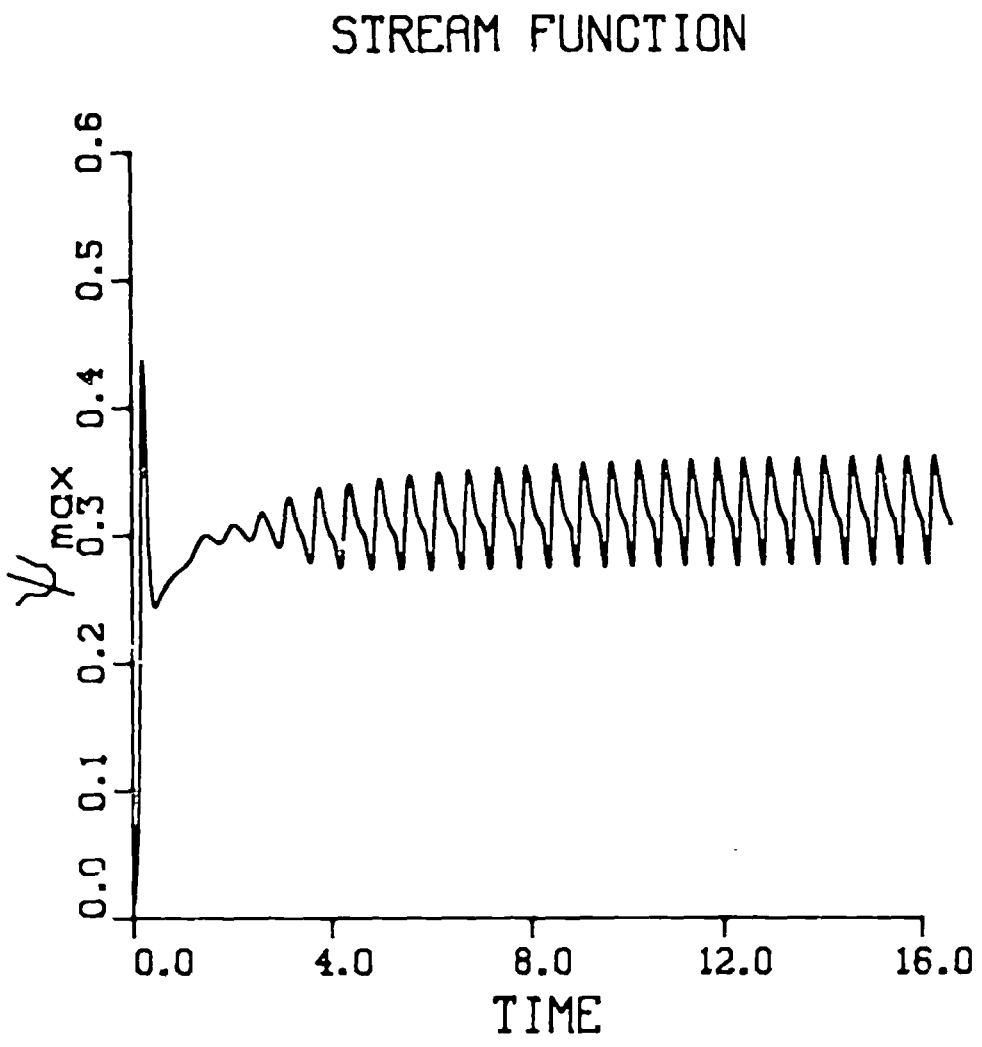

Fig. 10. The maximum of the stream function as a function of time (in units of H^2/ν) for $Rs/Rs^* = 3.3$, $VH/D = 4.17$, and $H/\lambda = 1.551$. The values of the other parameters are given in Table 2. The stream function is periodic in time; the spatial variation of the stream function during one cycle is shown in Figs. 12-16.

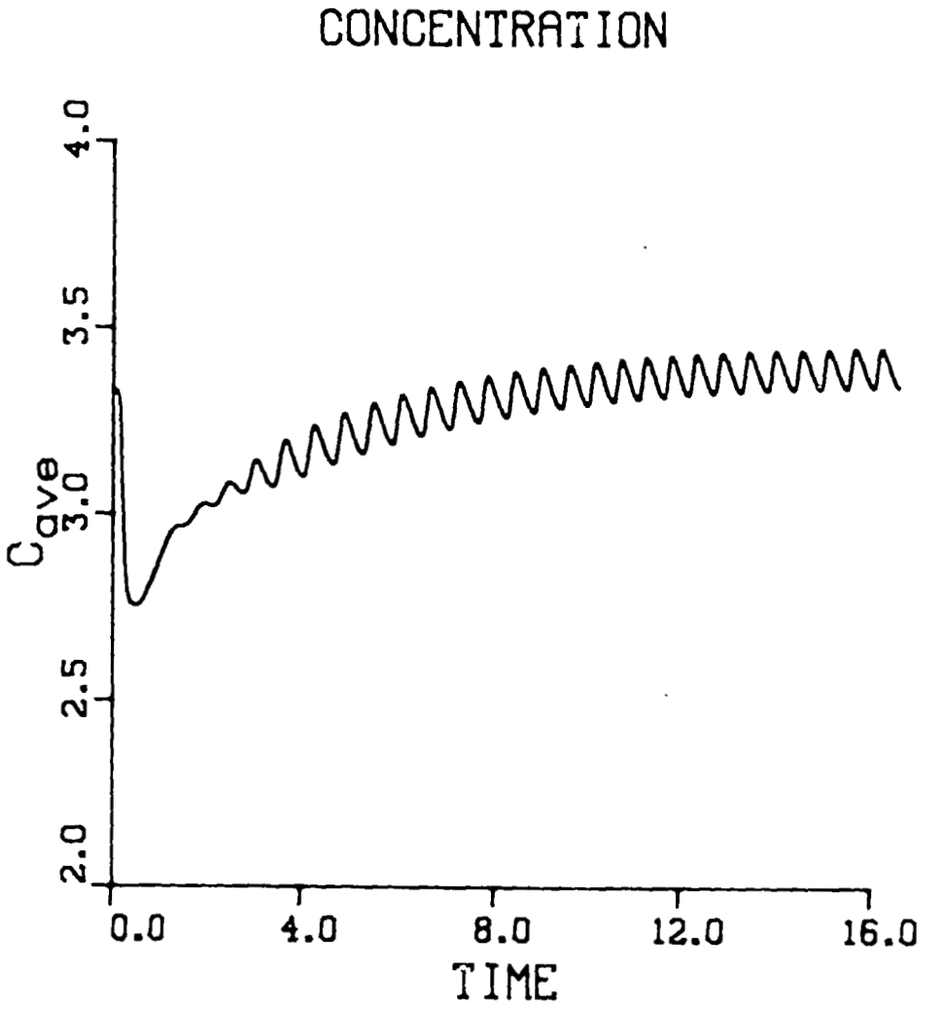

Fig. 11. The average concentration at the crystal-melt interface as a function of time for the same parameters as in Fig. 10. The spatial variation of the concentration during one cycle is shown in Figs. 17-21.

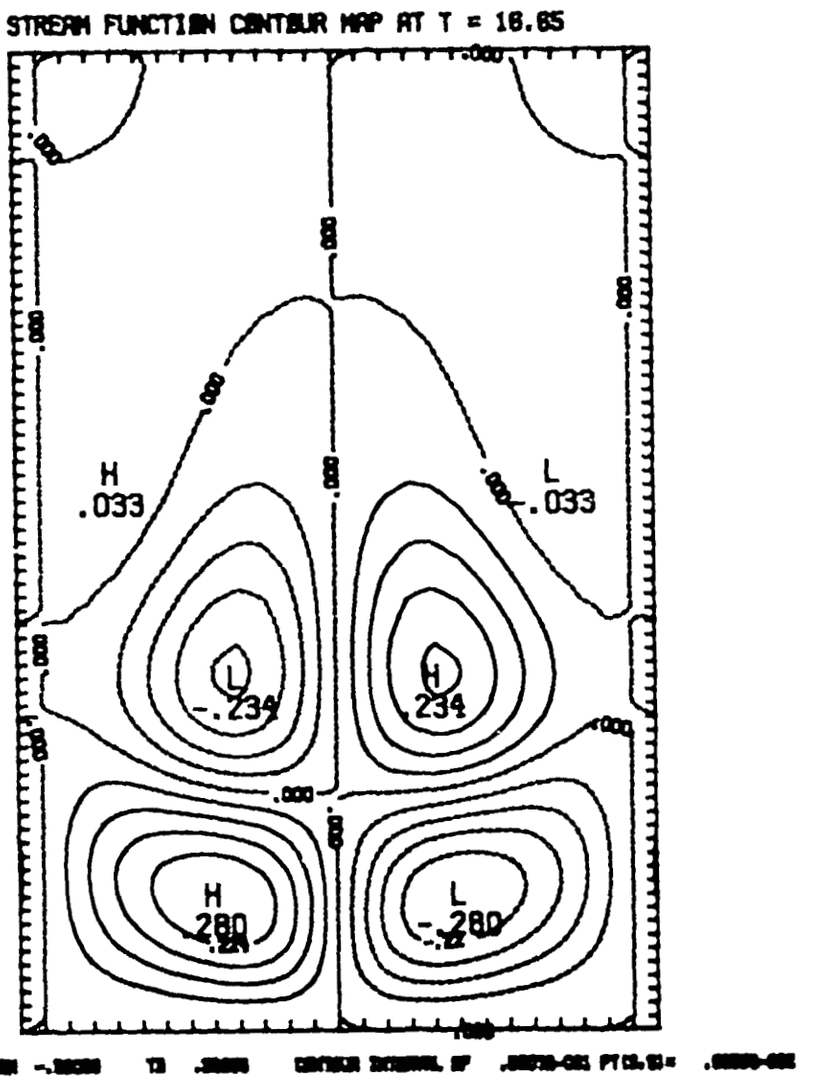

Fig. 12. The stream function as a function of position at dimensionless time 16.65 for the same parameters as in Fig. 10.

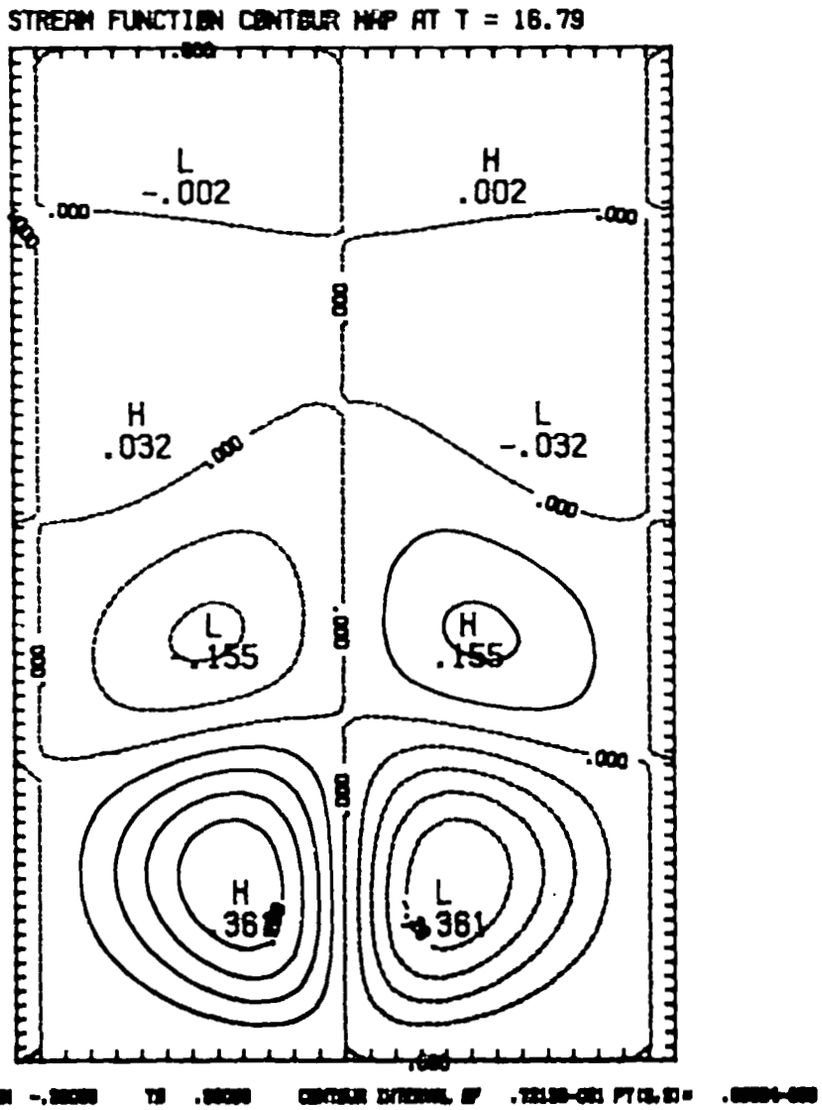

Fig. 13. The stream function as a function of position at dimensionless time 16.79 for the same parameters as in Fig. 10.

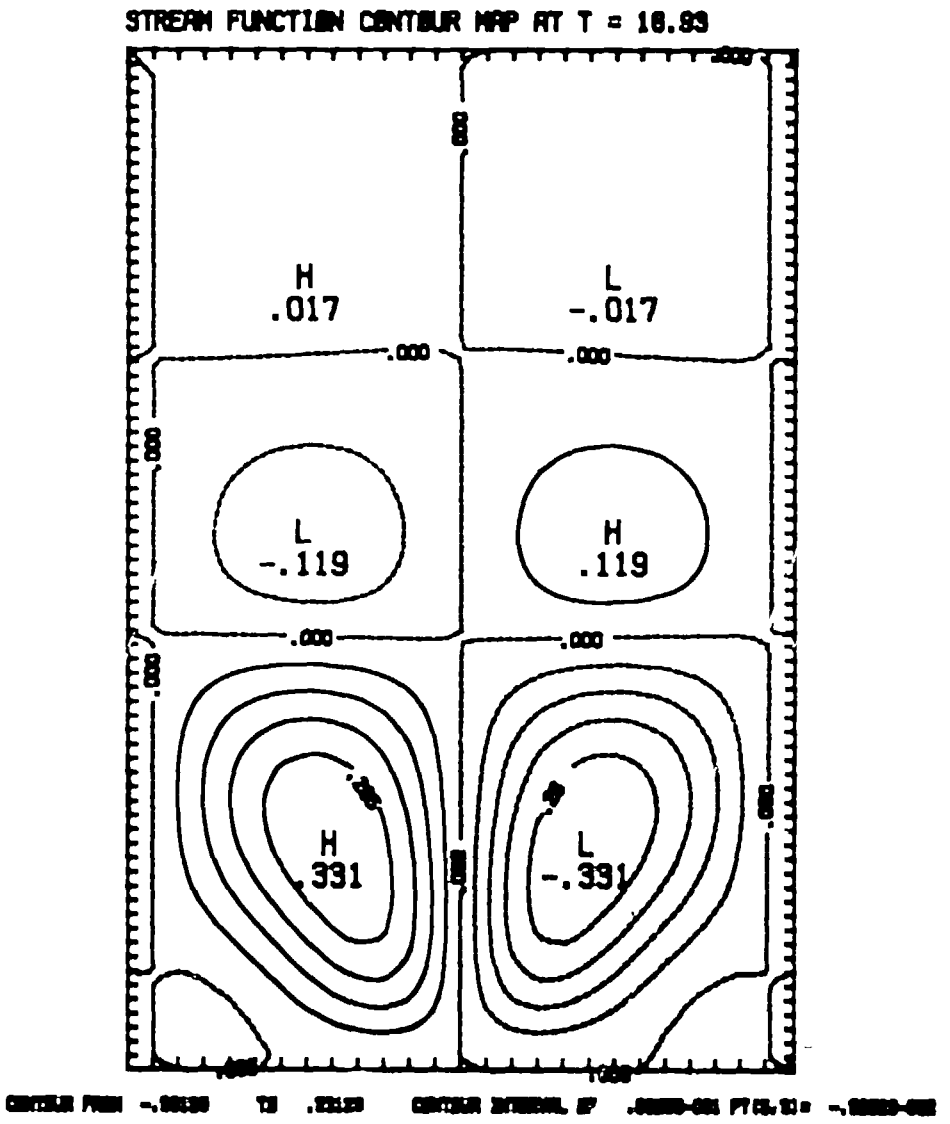

Fig. 14. The stream function as a function of position at dimensionless time 16.93 for the same parameters as in Fig. 10.

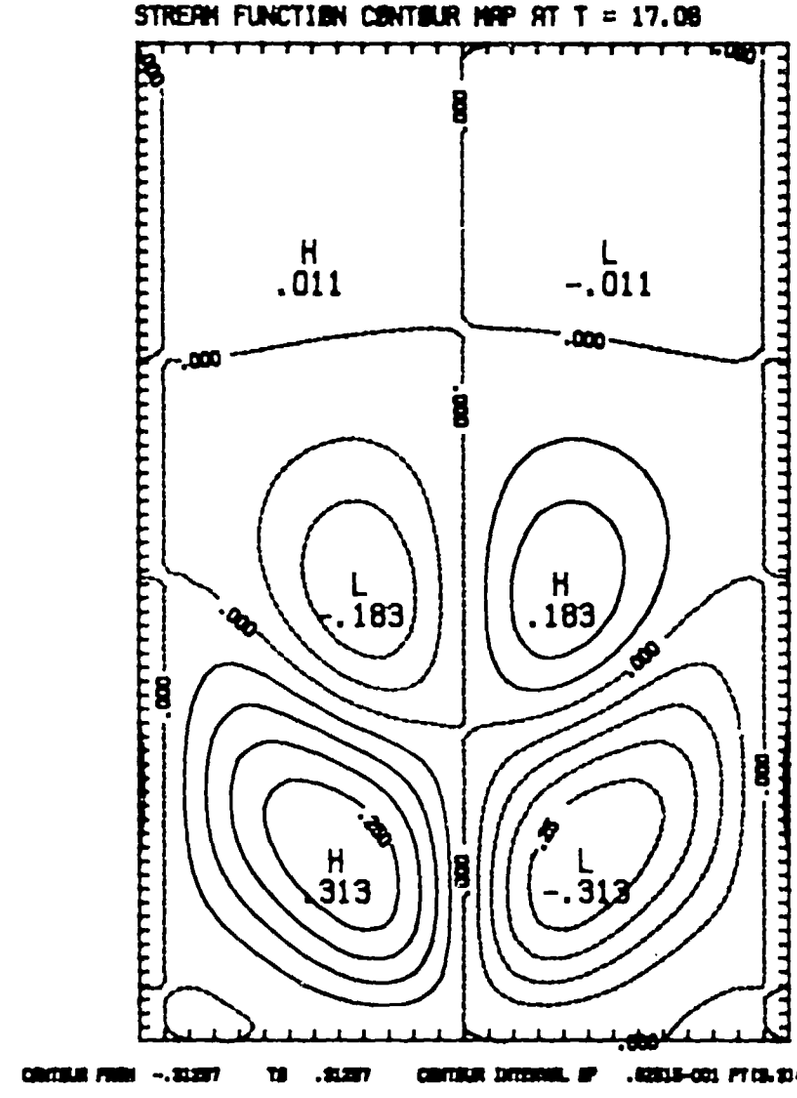

Fig. 15. The stream function as a function of position at dimensionless time 17.08 for the same parameters as in Fig. 10.

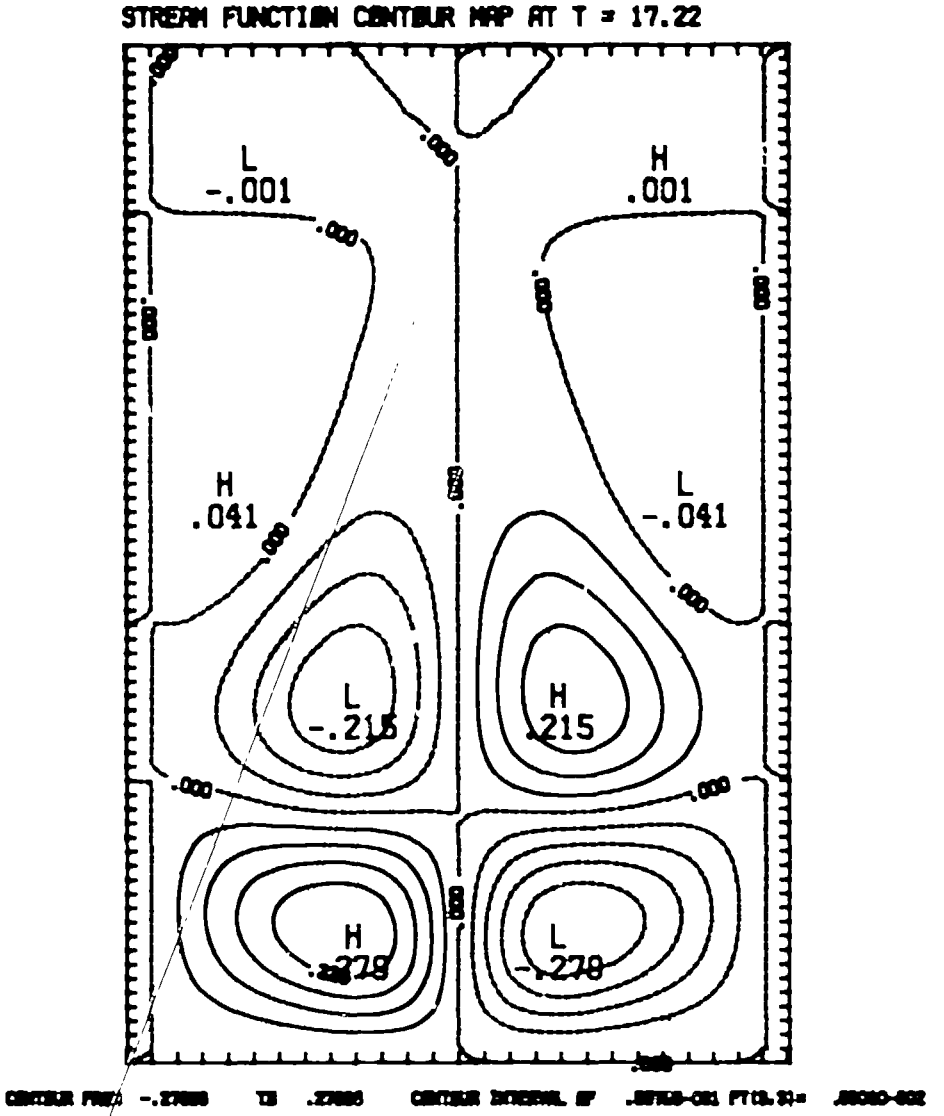

Fig. 16. The stream function as a function of position at dimensionless time 17.22 for the same parameters as in Fig. 10.

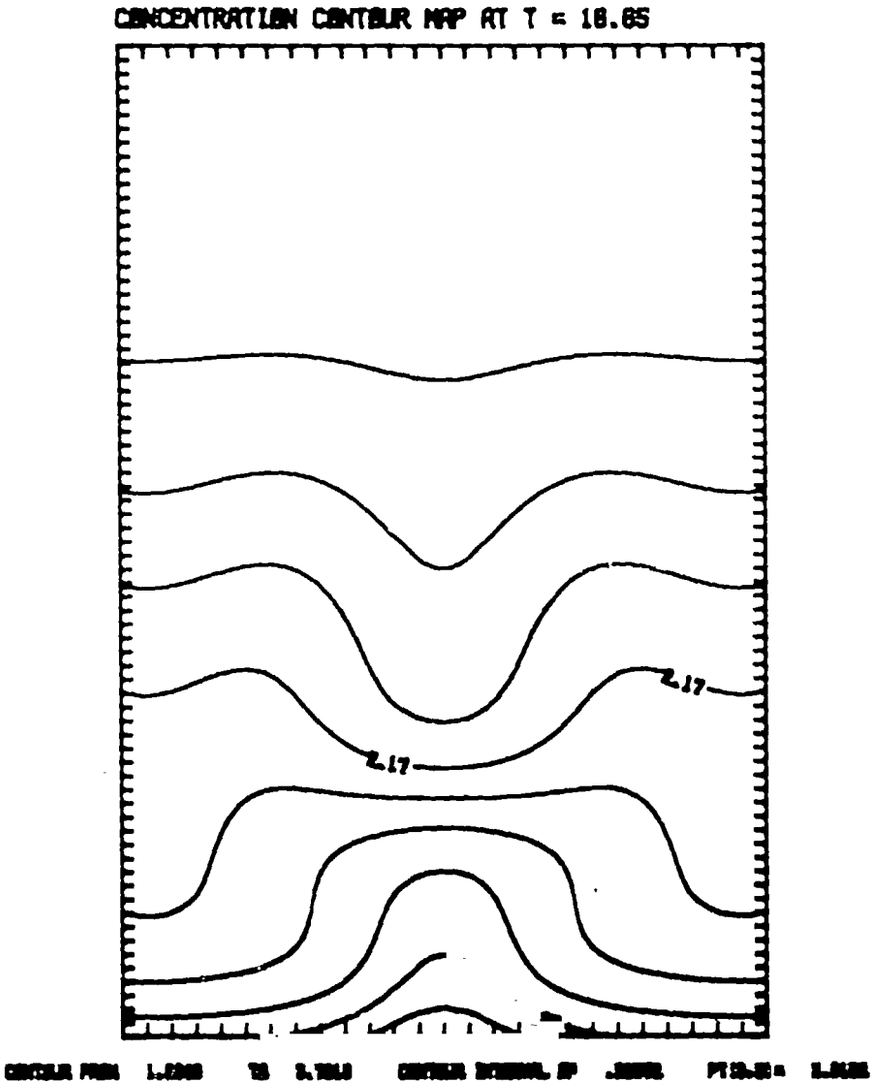

Fig. 17. The solute concentration as a function of position at dimensionless time 16.65 for the same parameters as in Fig. 10.

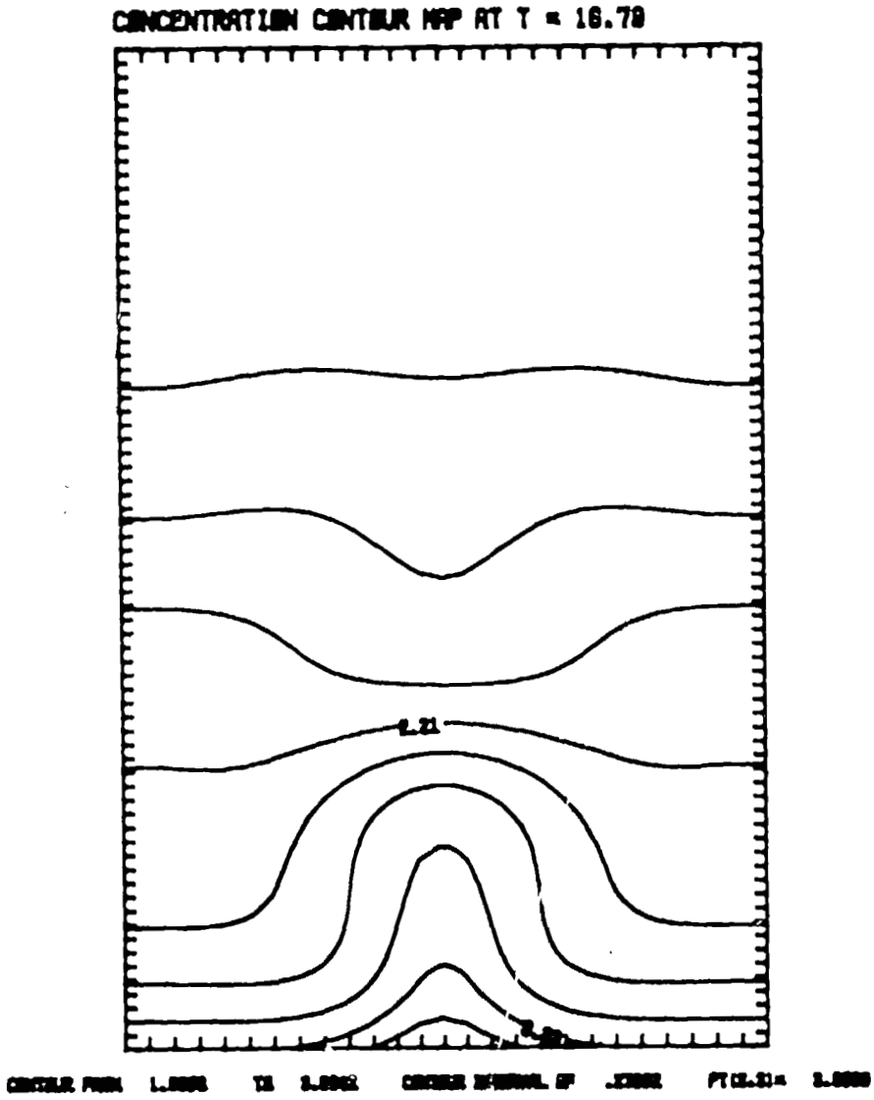

Fig. 18. The solute concentration as a function of position at dimensionless time 16.79 for the same parameters as in Fig. 10.

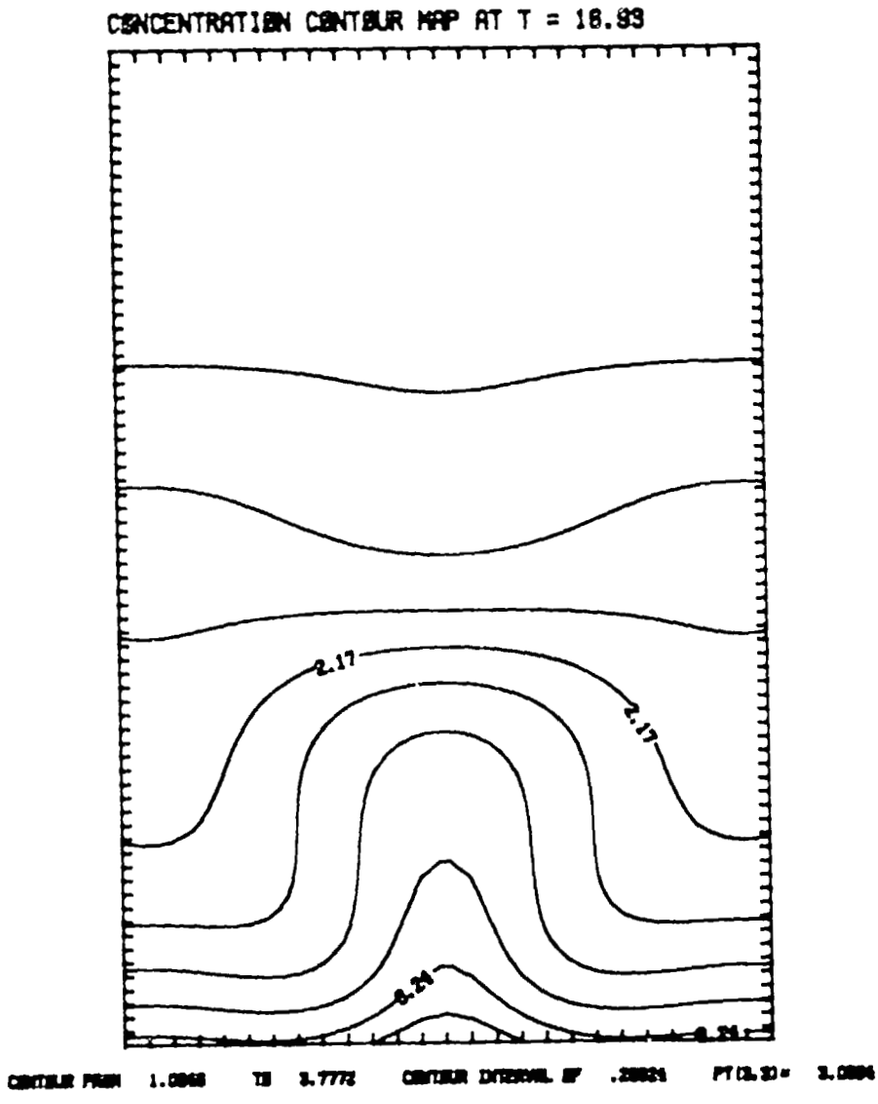

Fig. 19. The solute concentration as a function of position at dimensionless time 16.93 for the same parameters as in Fig. 10.

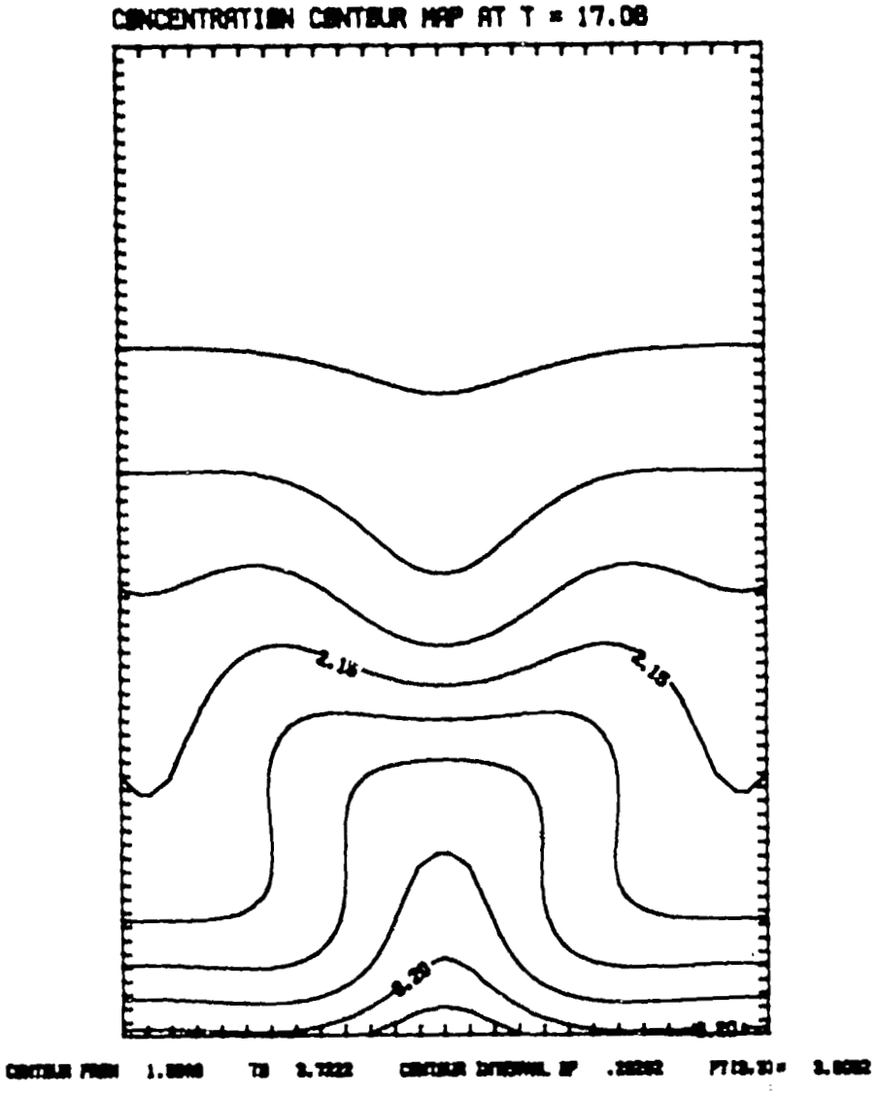

Fig. 20. The solute concentration as a function of position at dimensionless time 17.08 for the same parameters as in Fig. 10.

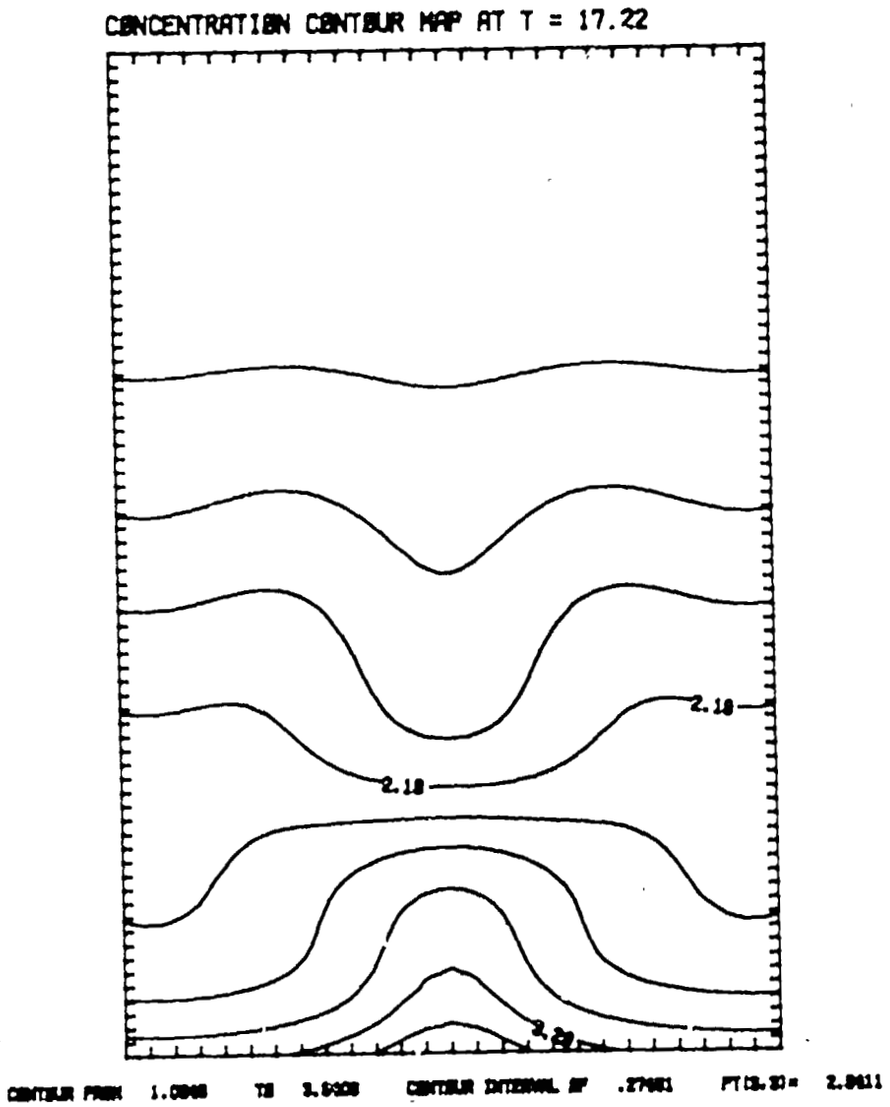

Fig. 21. The solute concentration as a function of position at dimensionless time 17.22 for the same parameters as in Fig. 10.

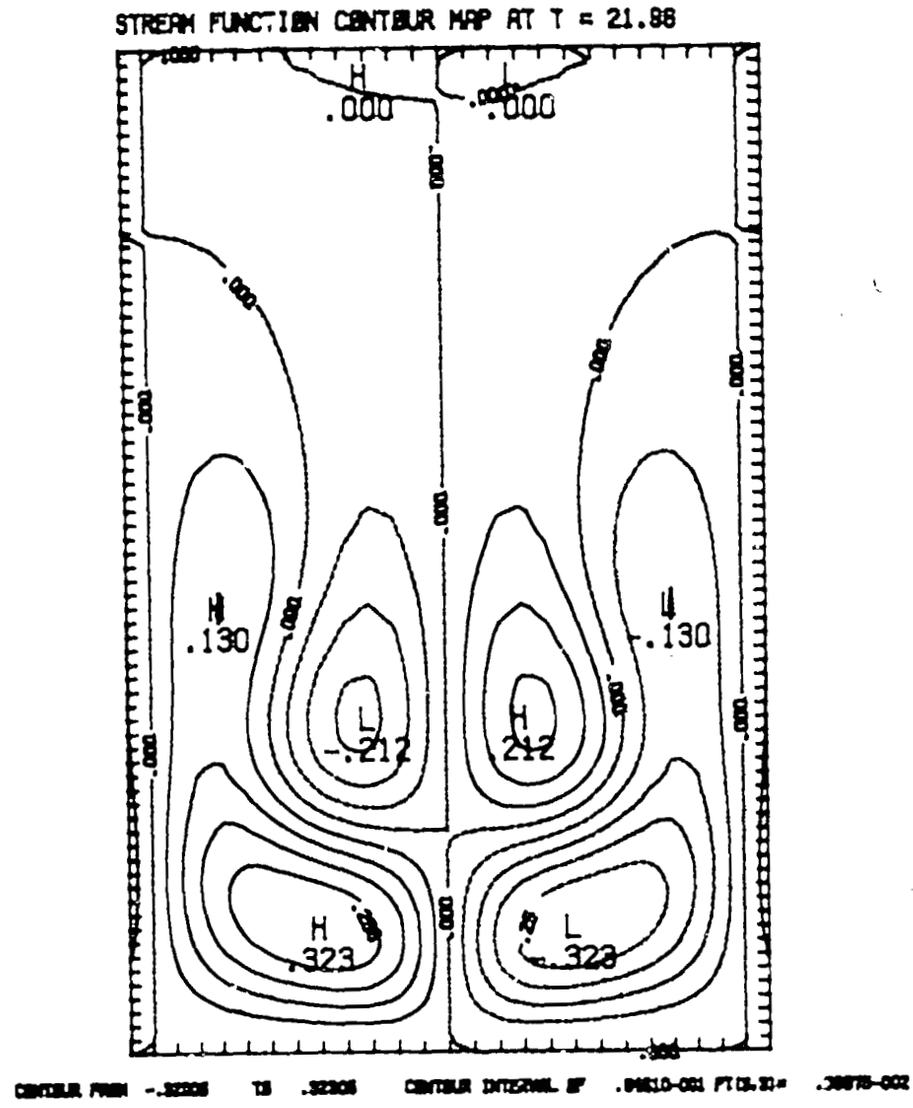

Fig. 22. The steady state stream function as a function of position for $R_s/R_s^* = 3.6$, $VH/D = 4.17$, and $H/\lambda = 1.552$. The values of the other parameters are given in Table 2. The initial state for this solution was the solution periodic in time shown in Figs. 10-21 with $R_s/R_s^* = 3.3$

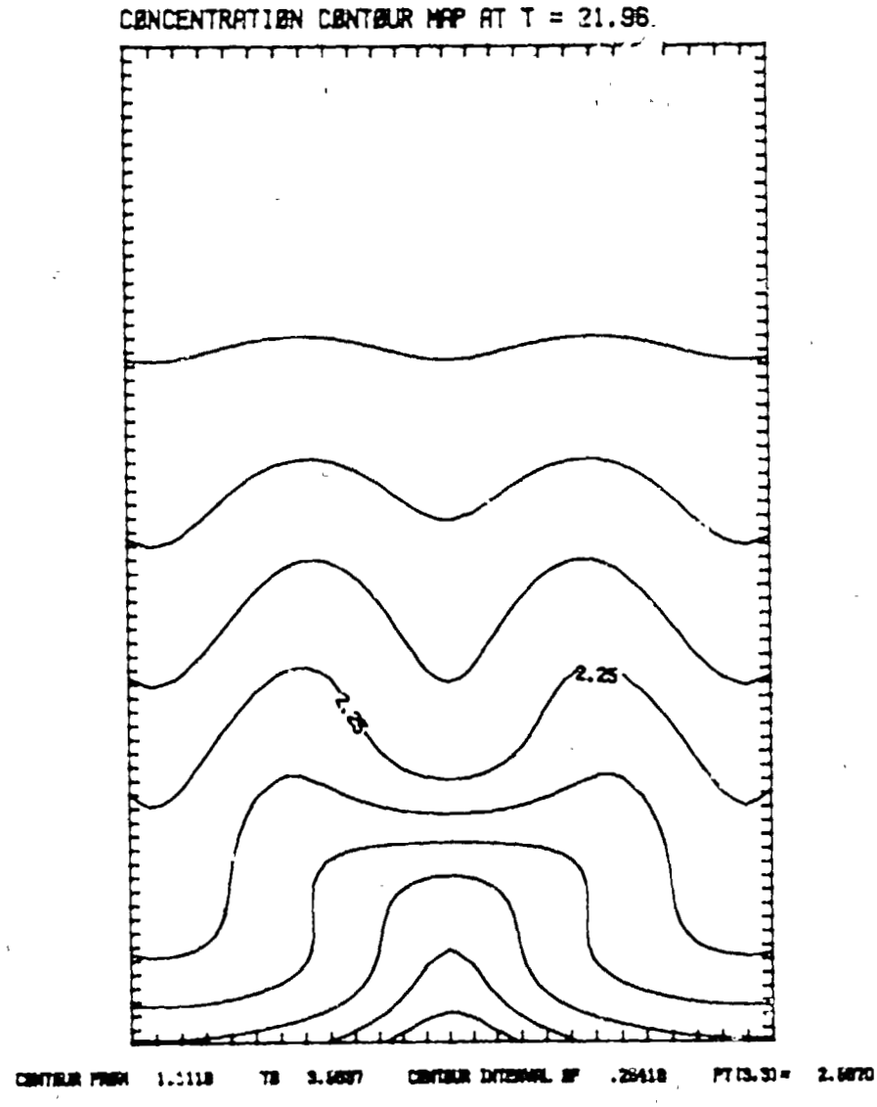

Fig. 23. The steady state concentration as a function of position for the same parameters as in Fig. 22.

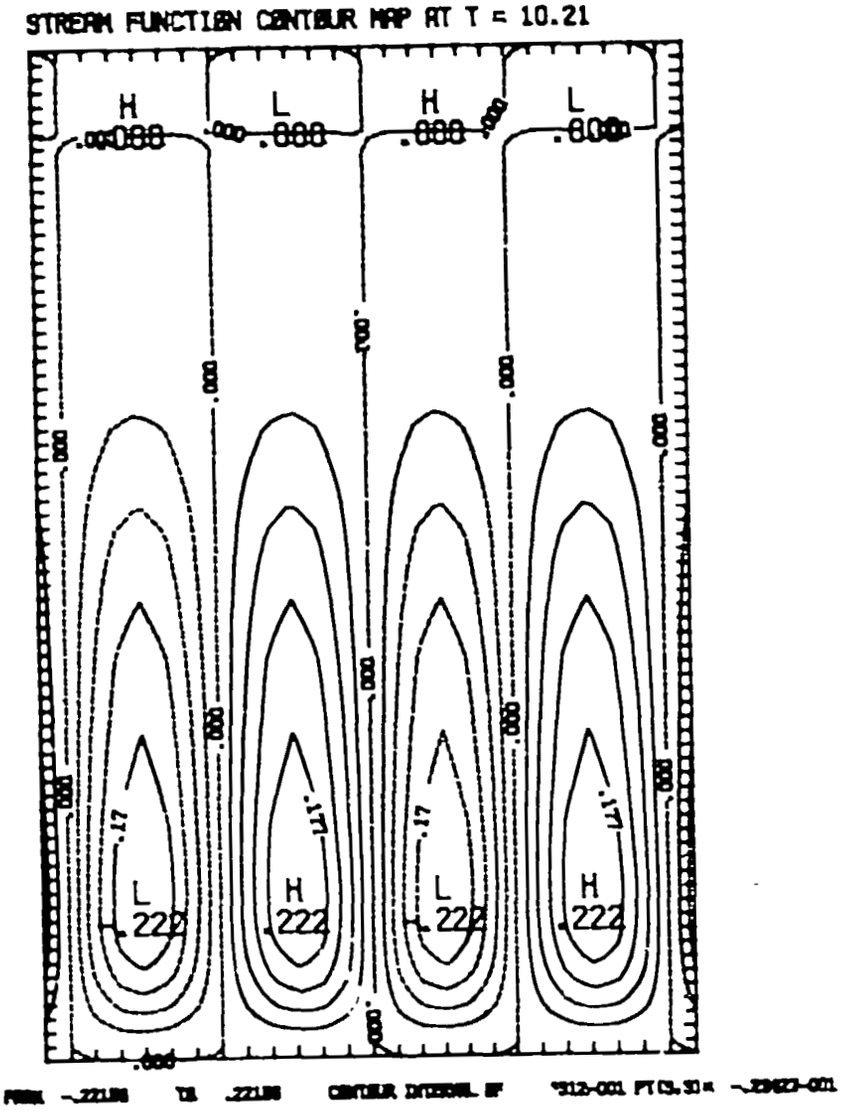

Fig. 24. The steady state stream function as a function of position for $Rs/R\overset{*}{s} = 3.6$, $VH/D = 4.17$, and $H/\lambda = 1.552$ (same as Figs. 22-23). The initial state for this solution was a perturbed exponential concentration field. The steady state solution has one half the wavelength of the initial state. Comparison with Fig. 22 indicates that the steady state solution depends on the initial conditions.

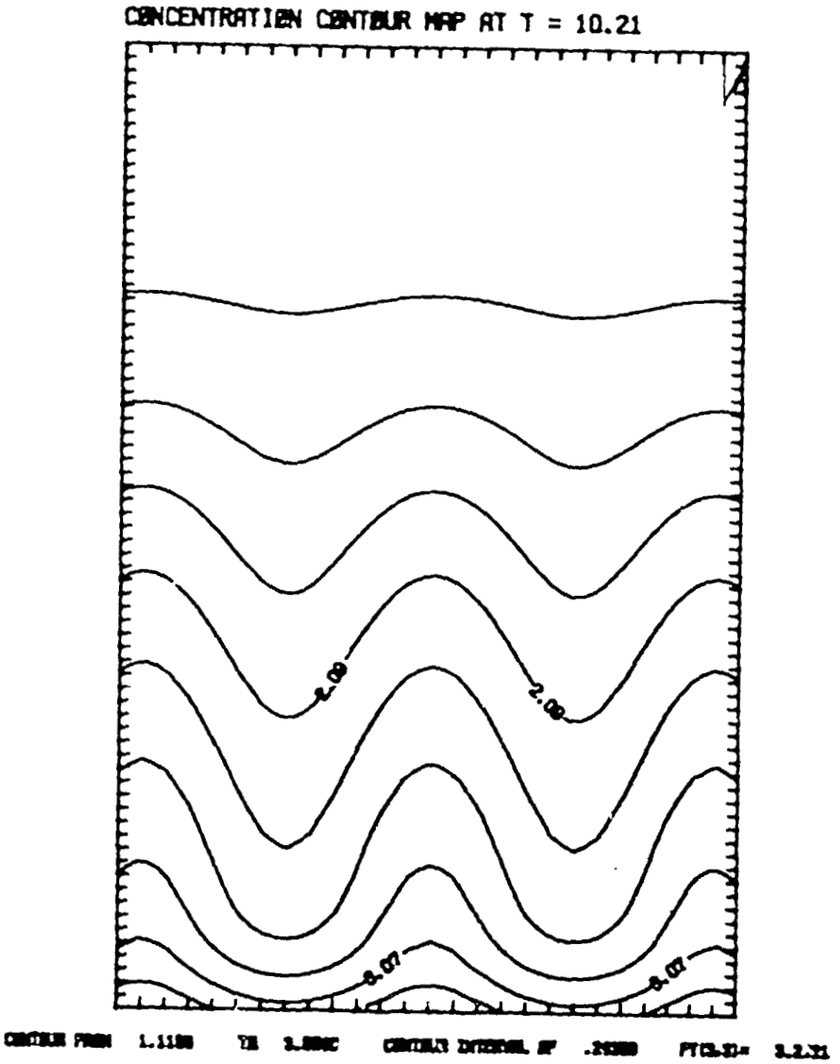

Fig. 25. The steady state concentration as a function of position for the same parameters as in Fig. 24.

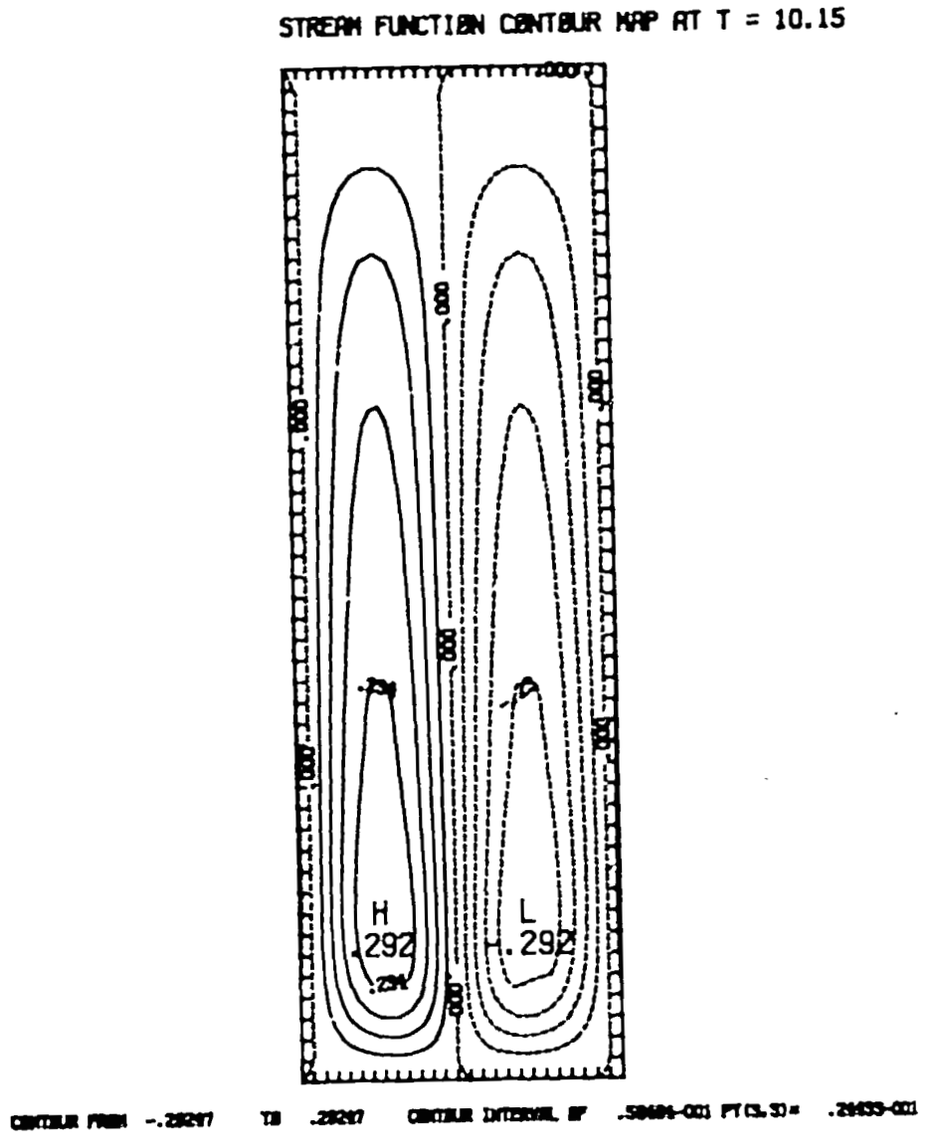

Fig. 26. The steady state stream function as a function of position for $R_s/R_{\bar{s}} = 5.03$, $VH/D = 4.17$, and $H/\lambda = 3.104$. The values of the other parameters are given in Table 2.

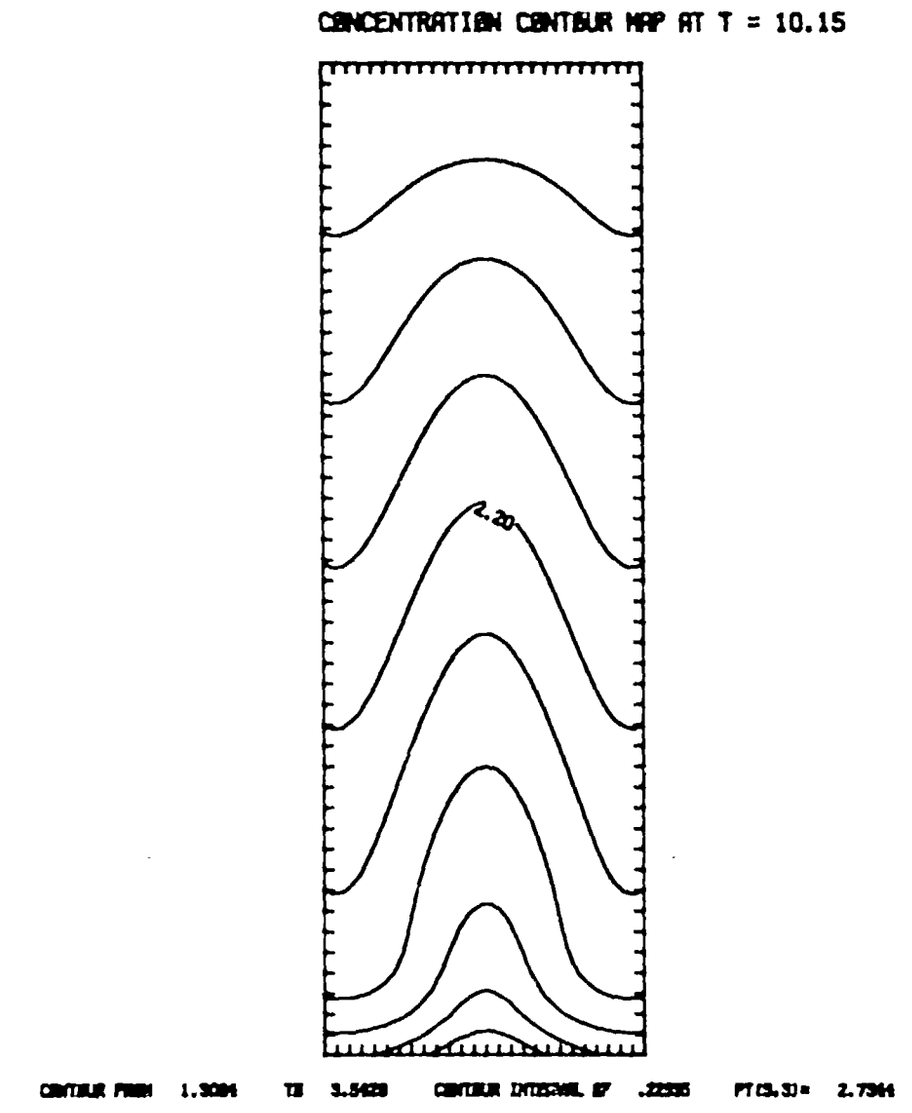

Fig. 27. The steady state concentration as a function of position for the same parameters as in Fig. 26.

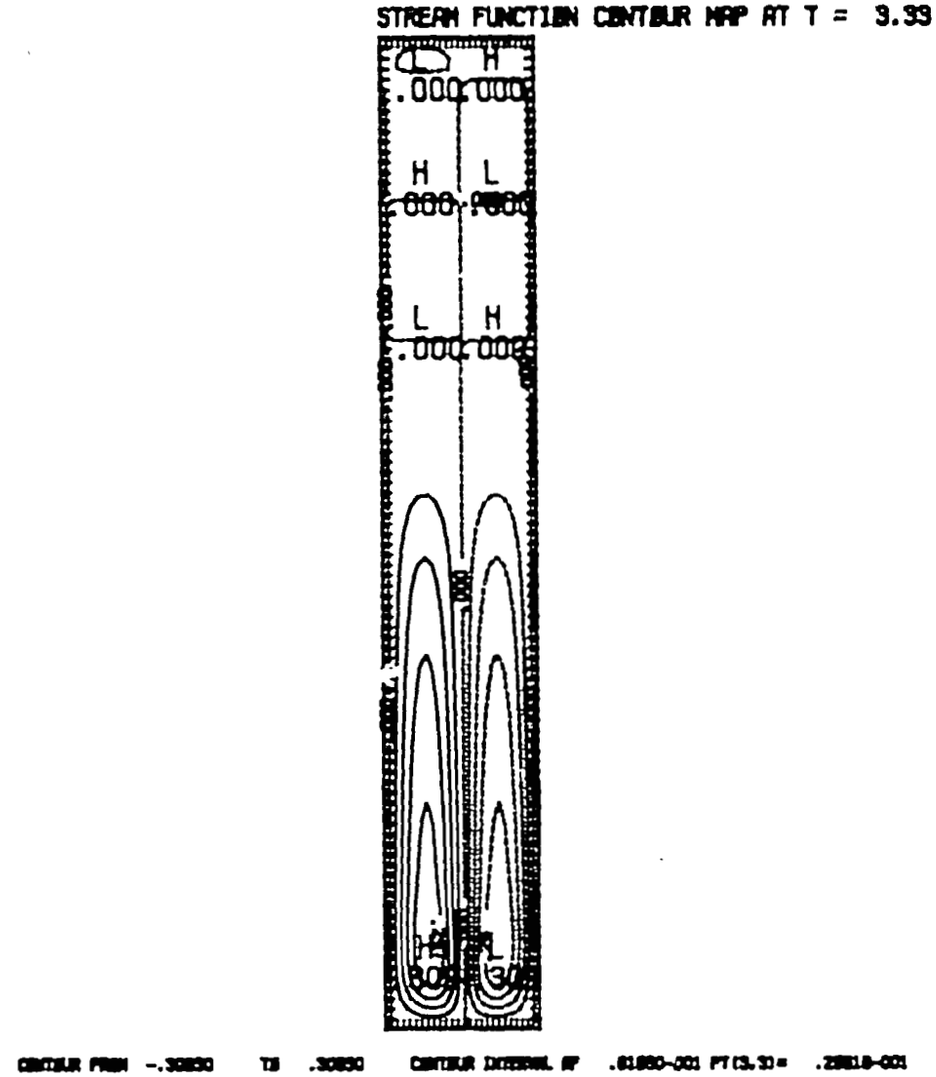

Fig. 28. The steady state stream function as a function of position for $R_s/R_{\bar{s}} = 5.03$, $VH/D = 8.33$, and $H/\lambda = 6.208$. The values of the other parameters are given in Table 2. This calculation is identical to that of Fig. 26 except that the height has been doubled.

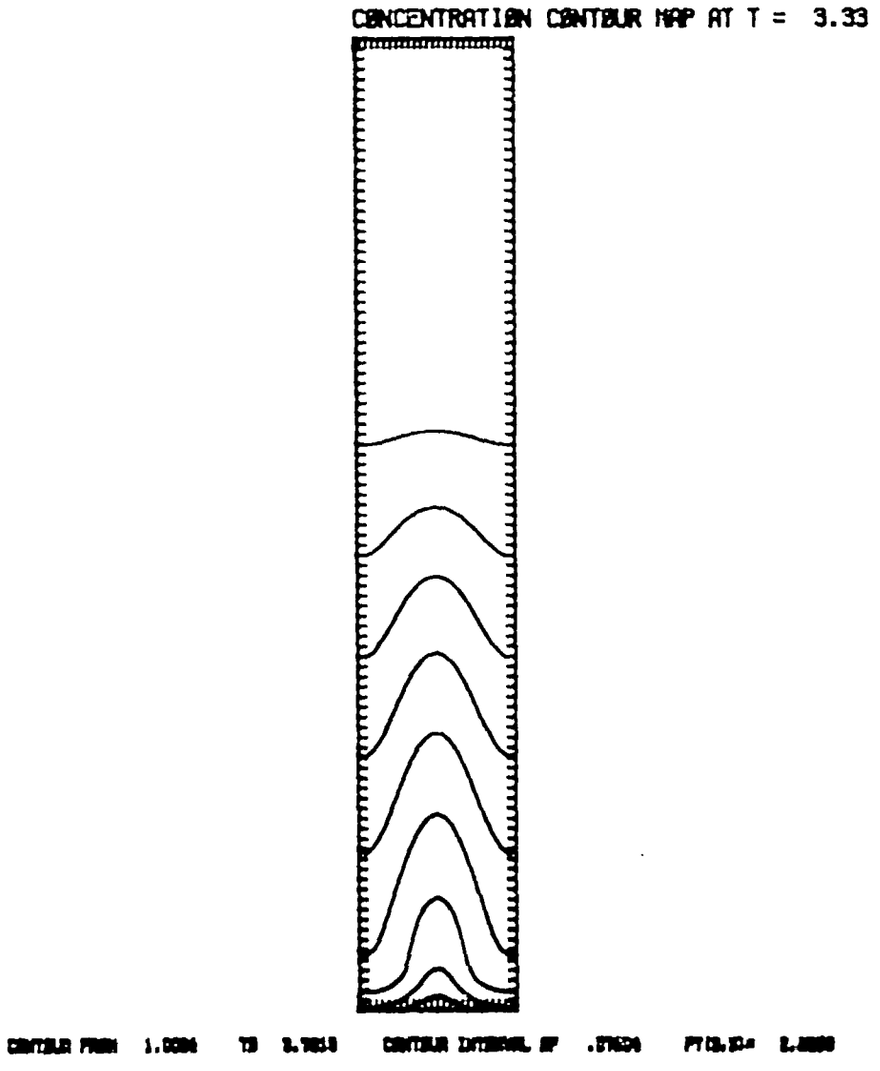

Fig. 29. The steady state concentration as a function of position for the same parameters as in Fig. 28.

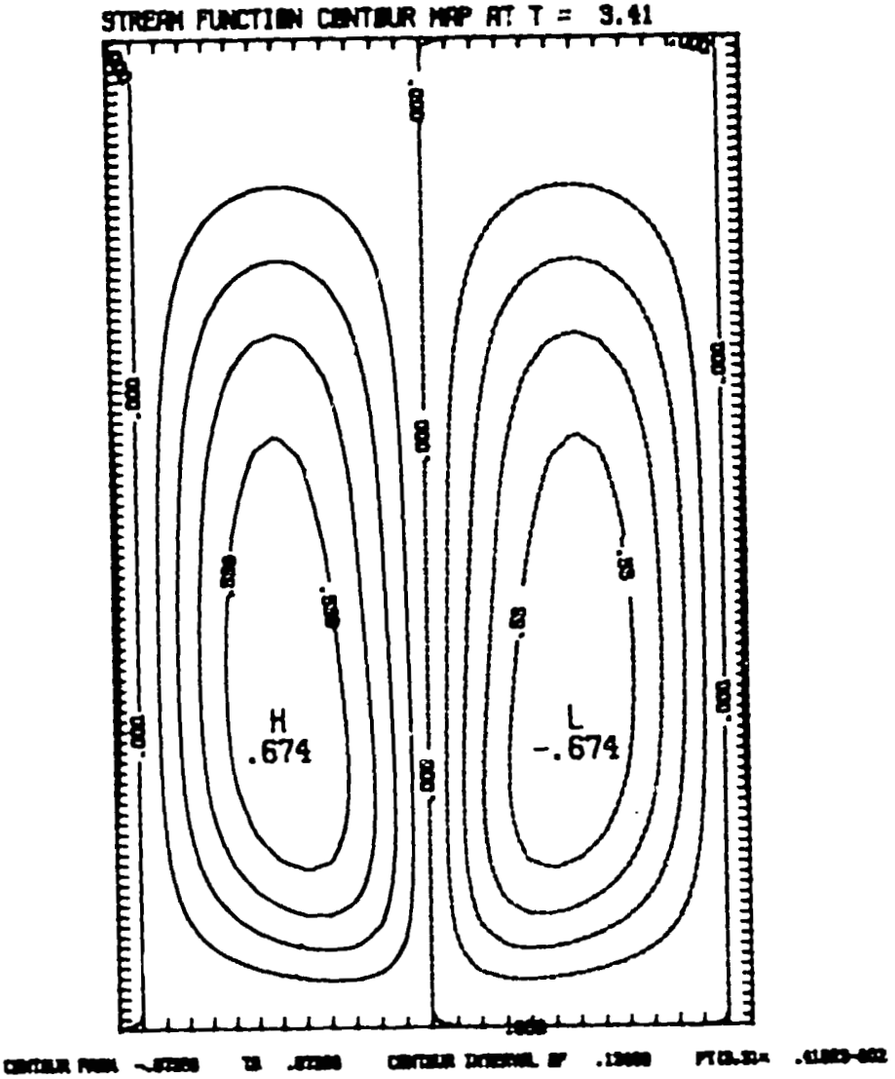

Fig. 30. The steady state stream function as a function of position for $Rs/Rs^{*} = 1.33$, $VH/D = 20.0$, $H/\lambda = 1.547$, $Ra = 0.127$, $Rs^{*} = 6.78$, and $D/V = 0.015$ cm. The values of the other parameters are given in Table 2.

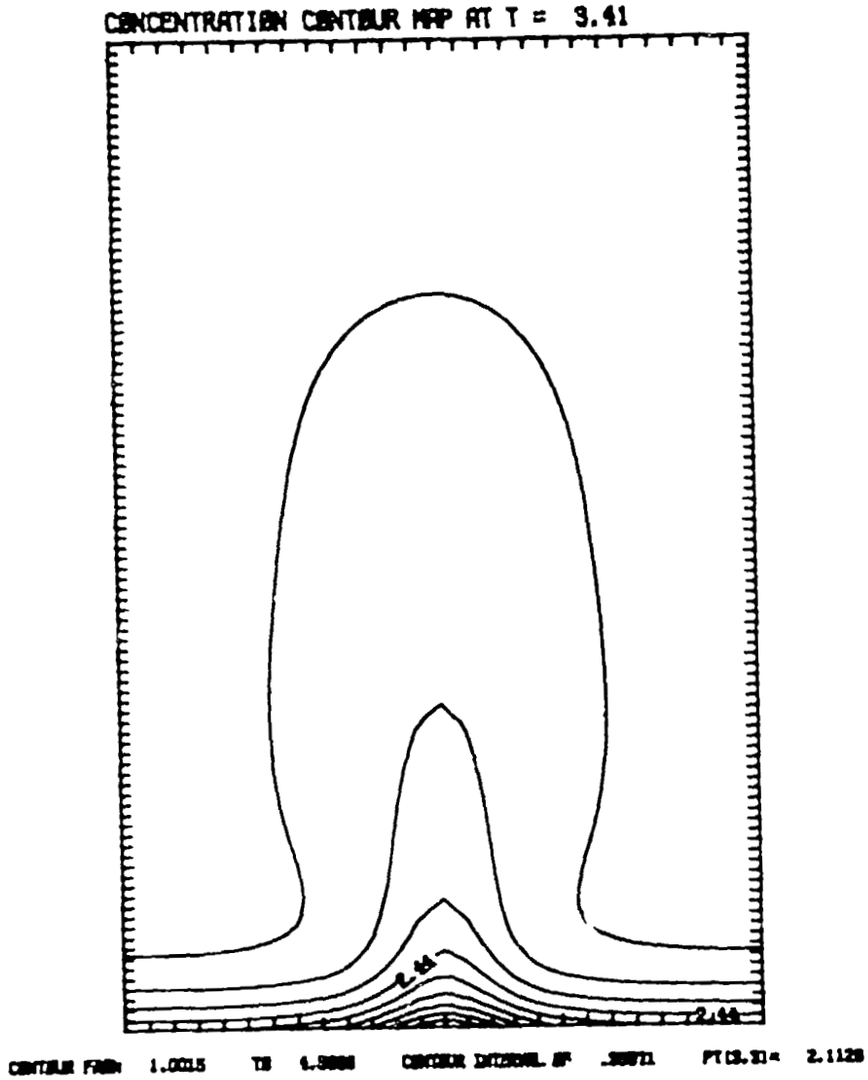

Fig. 31. The steady state concentration as a function of position for the same parameters as in Fig. 26.

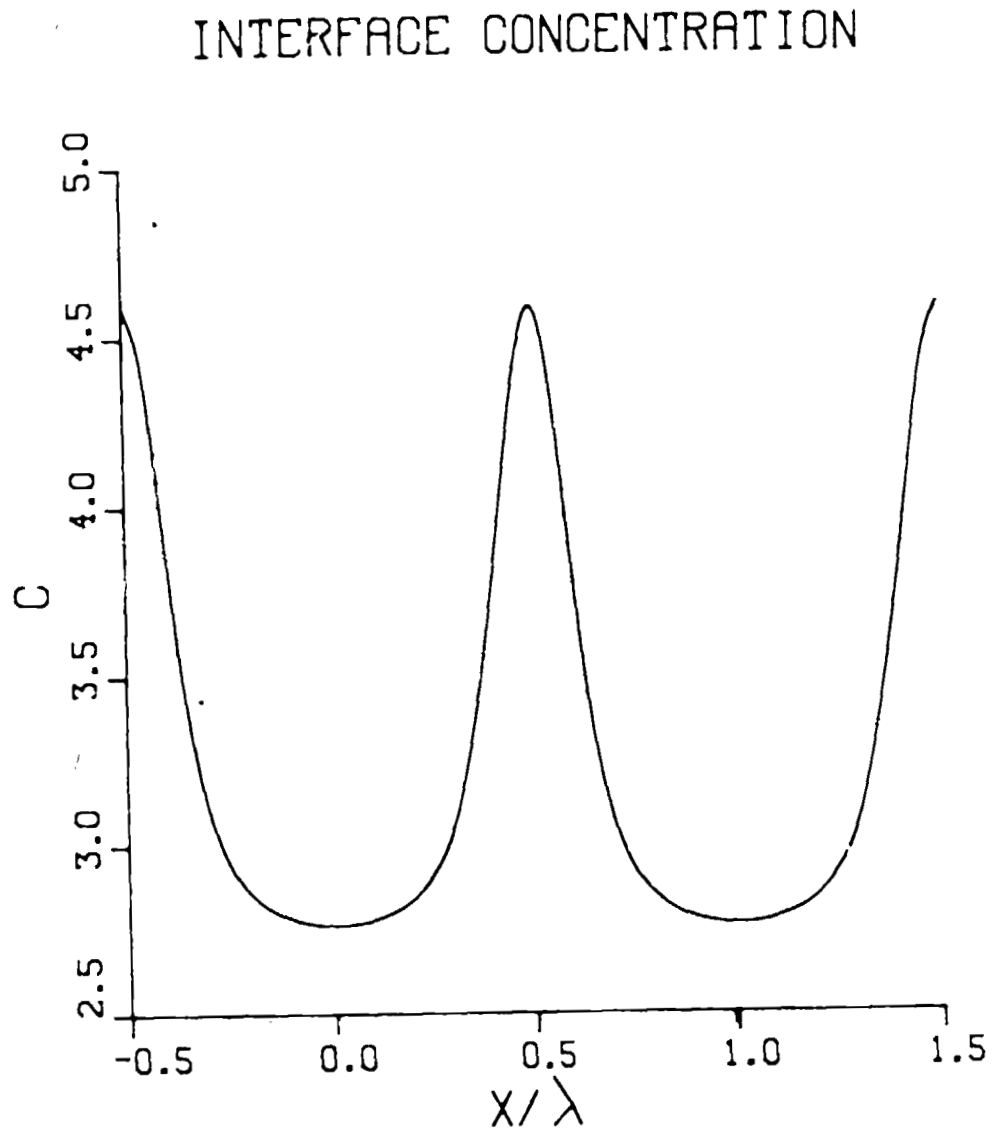

Fig. 32. The steady state interface concentration in the melt for two wavelengths in the lateral direction for the same parameters as in Fig. 31.

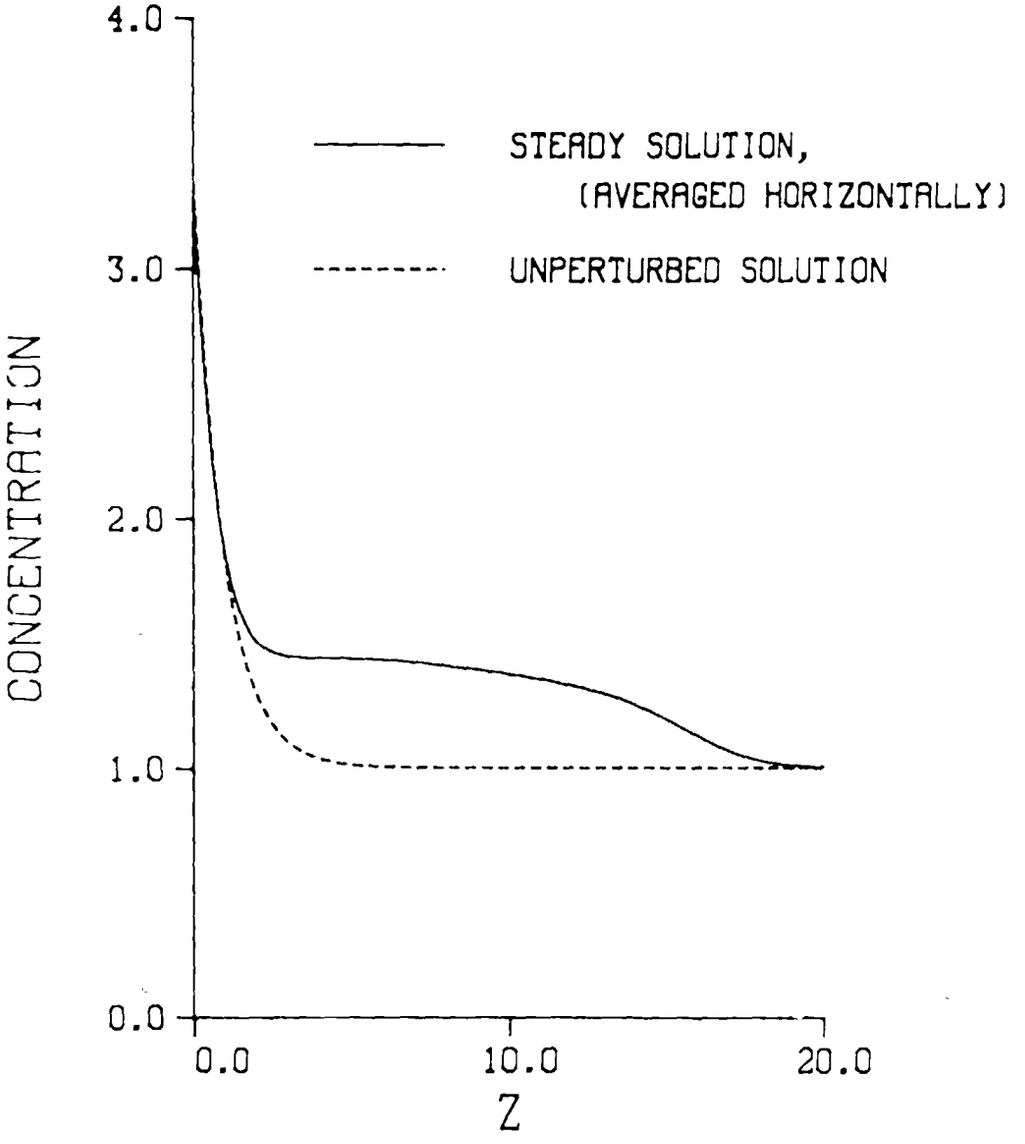

Fig. 33. The average steady state concentration in the melt as a function of the distance (in units of D/V) from the crystal-melt interface for the same parameters as in Fig. 30. The dashed line indicates the concentration in the absence of convection.

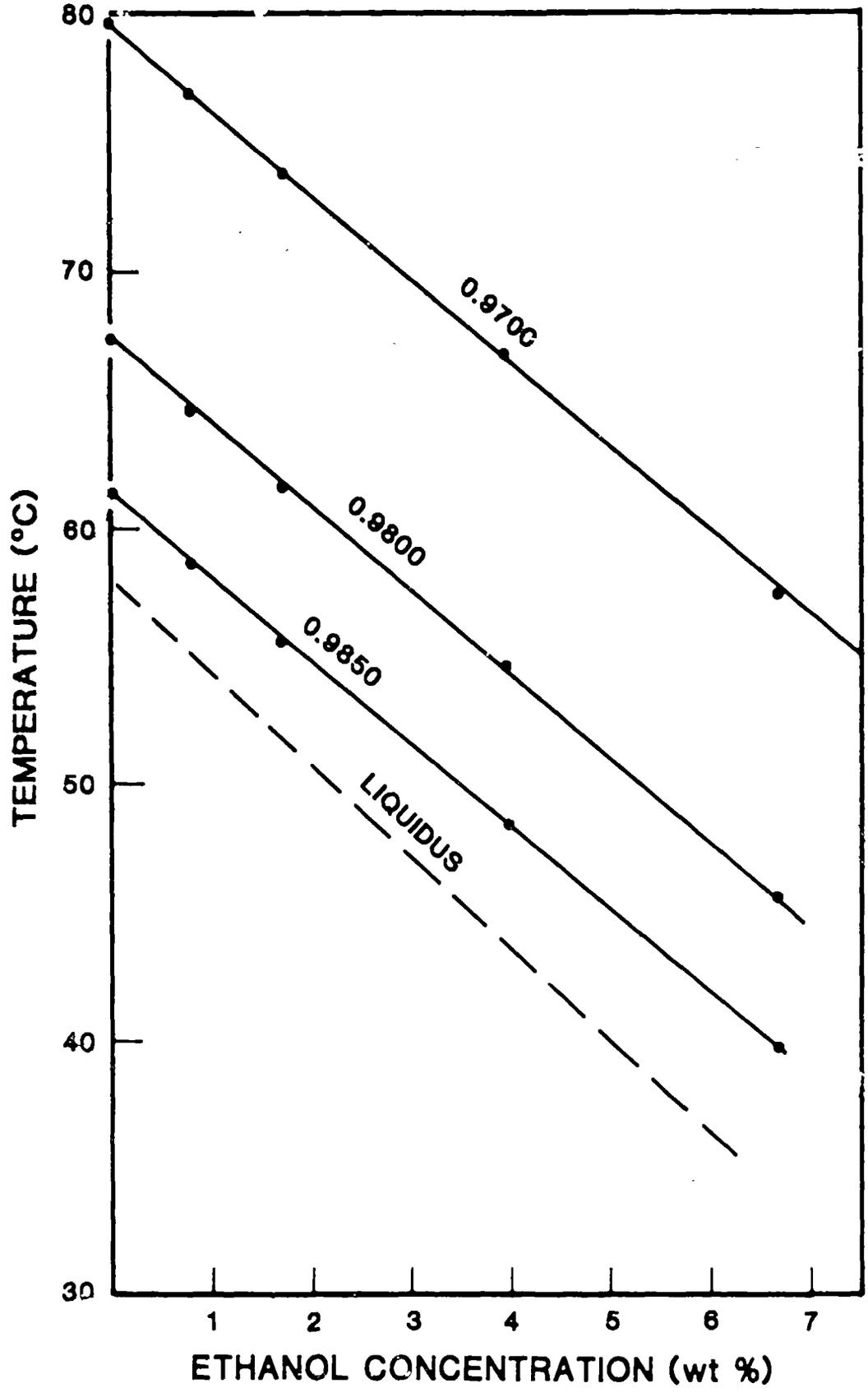

Fig. 34. Temperature and composition dependence of the density of dilute solutions of ethanol in succinonitrile.

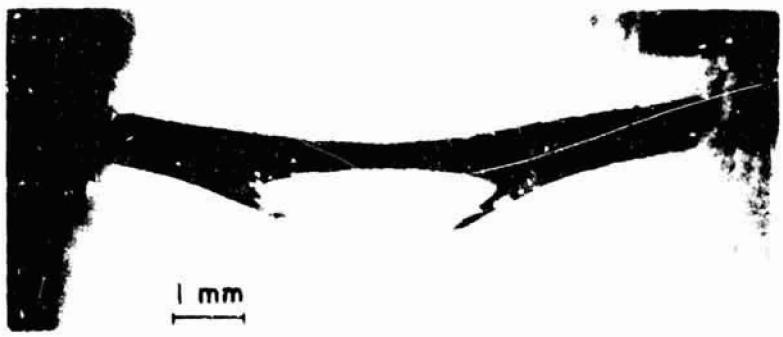

Fig. 35. Central pits formed during the solidification of succinonitrile containing 2.6×10^{-3} wt.% ethanol.
a. at a growth velocity of 2 μm/s.

Fig. 35. Central pits formed during the solidification of succinonitrile containing 2.6×10^{-3} wt.% ethanol.
b. at a growth velocity of 3 μm/s.

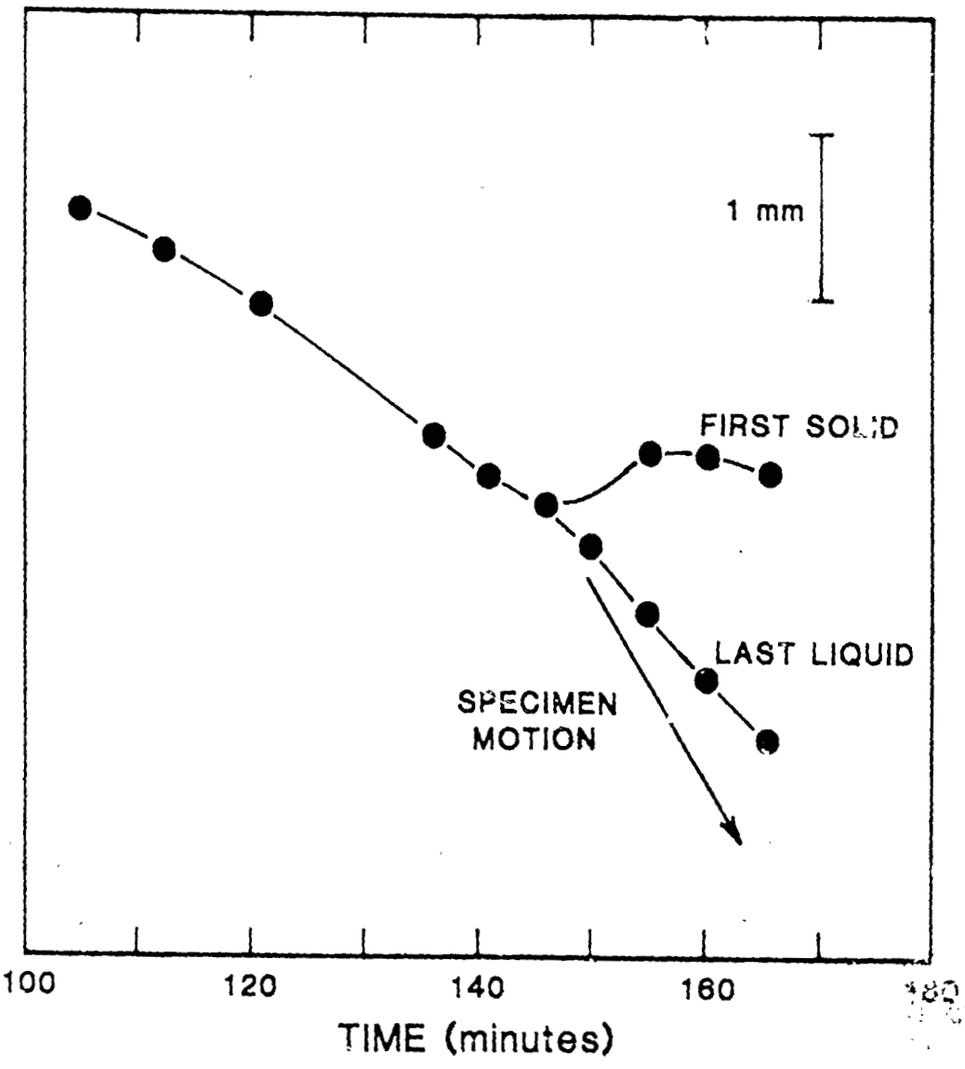

Fig. 36. Interface positions during the formation of a central pit, as a function of time following the start of growth, 2 μm/s. The position of the bottom of the pit is plotted until the cellular structure develops: the leading and trailing edges of the cellular structure are then shown.

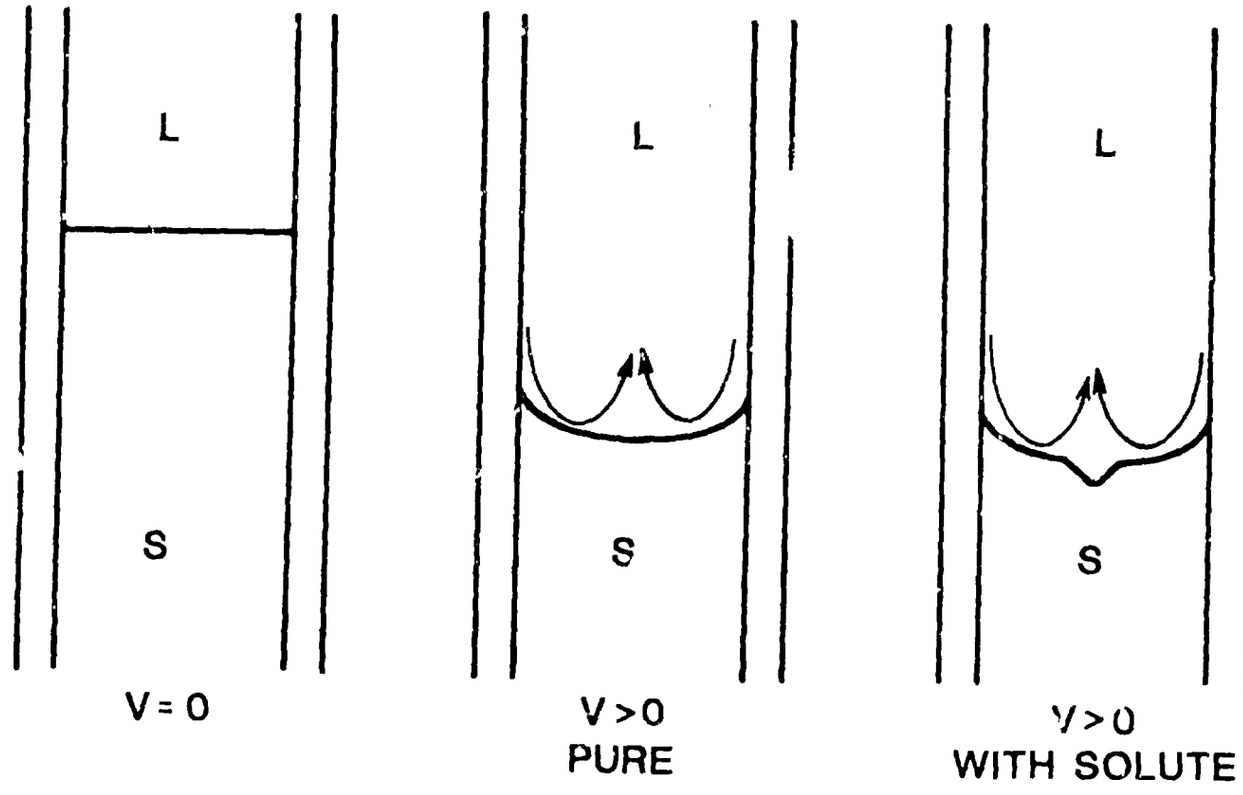

Fig. 37. Interface shapes and fluid flow patterns.
a. With no solidification, the interface is almost flat and only a small residual fluid flow is present.
b. In the pure material, solidification results in a bowl-shaped interface with a simple convective flow pattern.
c. With solute present, the same convective flow pattern redistributes solute to form a central depression in the interface.

APPENDIX

Coupled Convective Instabilities at Crystal-Melt Interfaces

S. R. Coriell, G. B. McFadden, and R. F. Boisvert
National Bureau of Standards
Washington, D.C. 20234

and

M. E. Glicksman and Q. T. Fang
Materials Engineering Department
Rensselaer Polytechnic Institute
Troy, NY 12181

The interaction between fluid flow and the crystal-melt interface is of central importance in determining the solute distribution in the solidified material, which in turn determines its properties. The effect of convective flow on morphological stability has been recently reviewed [1]. Calculations by Delves [2] showed that a flow parallel to the crystal-melt interface could increase stability and give rise to traveling waves on the interface. The interaction of morphological instability with a melt subject to thermosolutal instability has also been studied [3]. In both these cases, morphological instability occurs even in the absence of fluid flow, although in general the critical value of the parameter for the onset of instability is changed by the flow.

Recent experiments [4-7] have demonstrated an interface instability under conditions for which in the absence of flow, the crystal-melt interface would be morphologically stable. In these experiments, a long vertical cylindrical sample of high purity succinonitrile was heated by passing an electrical current through a long, coaxial, vertical wire, so that a vertical melt annulus formed between the coaxial heater and the surrounding crystal-melt interface. The outer radius of the crystal was maintained at a constant temperature below the melting point (58.1°C).

With this arrangement the temperature increases in the melt and decreases in the crystal with distance from the crystal–melt interface, and consequently the interface would be morphologically stable in the absence of fluid flow.

Buoyancy dictates that the fluid flows upward near the heated wire and downward near the crystal–melt interface. There are analytic solutions of the fluid flow and temperature equations in which the flow velocity is vertical and the flow velocity and temperature are functions of the radial coordinate alone. Choi and Korpela [8] and Shaaban and Ozisik [9] have calculated the critical Grashof number for axisymmetric instabilities of the axisymmetric flow between two vertical, infinite, coaxial, rigid cylinders held at different temperatures. We [6] have repeated these calculations by a different numerical technique and for physical properties appropriate to succinonitrile (Prandtl number of 22.8). The flow between two vertical infinite coaxial cylinders containing succinonitrile is unstable to an axisymmetric perturbation above a Grashof number of 2150 and the wave speed of this perturbation is comparable to the unperturbed flow velocity.

When these calculations are carried out with the outer rigid cylinder replaced by a crystal–melt interface, quite different results are obtained. The onset of instability occurs by an asymmetric mode at a Grashof number of 176, which is in agreement with experiment. The linear stability calculations indicate that the density change on solidification and the crystal–melt surface tension are of little importance in determining the instability. The calculations predict that the period of oscillation (time for the wave to traverse one wavelength) is proportional to the fifth power of the gap width (the difference between the radius of the

crystal-melt interface and the wire radius). This has been verified experimentally with the period of oscillation ranging from 300 to 60000 s.

In order to understand better the "coupled mode" of instability, we use linear stability theory to analyze a simpler geometry, viz., we consider the stability of the parallel flow between a vertical crystal-melt interface and a vertical wall held at a temperature above the melting point of the crystal. Three modes of instability occur: (1) a buoyant mode, (2) a shear mode, and (3) a coupled crystal-melt mode. The first two modes are well known from previous research [10] on the instability of the flow between two vertical walls. The behavior of these modes as the Prandtl number varies will also be described.

Theory

We consider an $(\bar{x}, \bar{y}, \bar{z})$ Cartesian coordinate system such that in the unperturbed state the region $\bar{x} < 0$ is crystalline, the region $0 < \bar{x} < L$ is molten, and at $\bar{x} = L$ there is a rigid isothermal wall, whose temperature is greater than the melting point of the planar crystal by an amount ΔT. We assume that the force of gravity acts in the negative y direction and that all quantities are independent of the z-coordinate. We measure lengths in units of L; temperature T in units of ΔT; time t in units of L^2/ν, where ν is the kinematic viscosity, and velocities in units of a reference velocity U, which will be specified subsequently. The dimensionless equations for the fluid velocity $\bar{u}$ and the temperature are, in the Boussinesq approximation

$$\nabla \cdot \bar{u} = 0, \tag{1}$$

$$(\partial \bar{u}/\partial t) + Re\ (\bar{u}\cdot\nabla)\bar{u} = -\nabla p + \nabla^2\bar{u} + (G/Re)T\bar{j}, \tag{2}$$

$$(\partial T/\partial t) + Re\ u\cdot\nabla T = (\nabla^2 T)/P, \tag{3}$$

where $Re = UL/\nu$ is the Reynolds number, p is a dimensionless pressure, $G = g\alpha\Delta TL^3/\nu^2$ is the Grashof number, $\bar{j}$ is a unit vector in the y-direction, P is the Prandtl number, g is the gravitational acceleration, and α is the coefficient of thermal expansion. The temperature T_S in the crystal satisfies

$$(\partial T_S/\partial t) = \nabla^2 T/P_S, \tag{4}$$

where $P_S = P\kappa/\kappa_S = \nu/\kappa_S$ and κ and κ_S are the thermal diffusivities of the melt and crystal, respectively.

The boundary conditions at the crystal-melt interface are that the tangential component of the fluid velocity vanishes and that the normal component satisfies

$$\bar{u}\cdot\bar{n} = -\ \varepsilon(\bar{v}\cdot\bar{n}). \tag{5}$$

Here $\bar{n}$ is the normal to the crystal-melt interface, $\varepsilon = -1 + \rho_S/\rho_L$, ρ_S and ρ_L are the crystal and melt densities, respectively, and $\bar{v}$ is the local solidification velocity. At the crystal-melt interface, the temperature is continuous and equal to the equilibrium temperature, viz.,

$$T_{SI} = T_{LI} = -\Gamma K, \tag{6}$$

where the subscript I denotes evaluation at the crystal-melt interface. Temperature is measured relative to the dimensionless melting point $\bar{T}_M/\Delta T$ of the planar crystal-melt interface, $\Gamma = \bar{T}_M\gamma/(LH_V\Delta T)$, γ is the crystal-melt surface free energy, H_V is the latent heat of fusion per unit volume of solid, and K is the mean curvature of the crystal-melt interface. Conservation of energy at the crystal-melt interface requires

$$\Lambda(\bar{v}\cdot\bar{n}) = (-k_r\nabla T + \nabla T_s)\cdot\bar{n}, \tag{7}$$

where $\Lambda = \nu H_V Re/k_s\Delta T$ and k_r is the ratio of the thermal conductivity of the melt k_L to that of the crystal k_S.

At the rigid wall y = 1,

$$\bar{u} = 0 \tag{8}$$

and

$$T = 1. \tag{9}$$

In the crystal we require that far from the crystal-melt interface, the temperature gradient is constant and assumes a value such that the unperturbed planar interface is stationary.

A solution of the differential equations satisfying the boundary conditions is

$$u_{yo} = [1/4 - (x - 1/2)^2][(G/6Re)(x-1/2) + 6I], \tag{10a}$$

$$T_o = x, \tag{10b}$$

$$T_{So} = k_r X, \tag{10c}$$

$$p_o = [G/2Re - 12I]y, \tag{10d}$$

where I is the net flow in the y-direction, i.e., the integral of u_y from x = 0 to x = 1. The subscripts x and y denote the x and y components of $\bar{u}$ and the subscript o denotes the unperturbed or base flow and temperature fields.

We examine the stability of the flow with respect to small perturbations. We decompose the fluid velocity, temperature fields, and crystal-melt interface shape x_I into an unperturbed and perturbed part, and assume that the y and t dependences of the perturbed quantities are of the form $F(y, t) = \exp(i\omega y + \sigma t)$, where ω is a spatial frequency and $\sigma = \sigma_r + i\sigma_i$ is a complex number which determines the temporal behavior of the system. If $\sigma_r > 0$ for any value of ω, the system is unstable. We write

$$u_x = W_x(x)F, \tag{11a}$$

$$u_y = u_{yo} + W_y(x)F, \tag{11b}$$

$$T = x + T(x)F, \tag{11c}$$

$$T_s = k_r x + T_s(x)F, \tag{11d}$$

$$p = p_o + p_1(x)F, \tag{11e}$$

$$x_I = \delta F, \tag{11f}$$

where δ is the amplitude of the perturbation of the crystal-melt interface.

The linear ordinary differential equations for the perturbed quantities, W_x, W_y, p_1, T, and T_s can be written as

$$DW_x + i\omega W_y = 0, \tag{12a}$$

$$AW_x + i\omega DW_y + Dp_1 = 0, \tag{12b}$$

$$-Re(Du_{yo})W_x + (D^2 - A)W_y - i\omega p_1 + (G/Re)T = 0, \tag{12c}$$

$$-PReW_x + (D^2 - A_T)T = 0, \tag{12d}$$

$$(D^2 - \omega^2 - P_S\sigma)T_S = 0, \tag{12e}$$

where $D = (\partial/\partial x)$, $A = \omega^2 + \sigma + i\omega Reu_{yo}$, and $A_T = \omega^2 + P(\sigma + i\omega Reu_{yo})$. The perturbed temperature field in the crystal, T_S, can be found analytically and is of the form $\exp[(\omega^2 + P_S\sigma)^{1/2}x]$.

It is desirable for purposes of numerical computation to prescribe the boundary conditions at $x = 0$ rather than at the crystal-melt interface $x = x_I$. This is easily accomplished in linear theory because any function, e.g., $f(x)$, evaluated at $x = x_I = \delta r$ can be written as $f(x_I) = f(0) + \delta F(\partial f/\partial x)$, where the partial derivative is evaluated at $x = 0$. Upon eliminating T_S and δ, we find the following boundary conditions for the fluid variables, W_x, W_y, and T at $x = 0$:

$$(1 + \Gamma\omega^2)ReW_x - \varepsilon\sigma T = 0, \tag{13a}$$

$$(1 + \Gamma\omega^2)W_y - (Du_{yo})T = 0, \tag{13b}$$

$$[(\omega^2 + P_S\sigma)^{1/2}(k_r + \Gamma\omega^2) + \sigma A/Re]T - k_r(1 + \Gamma\omega^2)(\partial T/\partial x) = 0. \tag{13c}$$

These boundary conditions are furhter simplified by taking $\Gamma = \varepsilon = 0$. It is not surprising and numerical calculations have verified that these are excellent approximations.

The boundary conditions at the rigid isothermal wall at $x = 1$ are

$$W_x = Wy = T = 0. \tag{14}$$

In order to understand the physical mechanism of instability, it is useful to compute the average kinetic energy of the perturbed flow field. The average kinetic energy in the disturbances is obtained by integrating the quantity $(\text{Real } u_x)^2 + [\text{Real}(u_y - u_{yo})]^2$, as given by eq. (11), over a basic cell having unit width in the x-direction and one wavelength $(2\pi/\omega)$ in the y-direction (Real indicates the real part of the complex functions u_x and u_y). At the onset of instability ($\sigma_r = 0$) the rate of change of the kinetic energy in the disturbance vanishes, and from eqs. (12b) and (12c), it follows that

$$-\left\langle |DW_x|^2 + |DW_y|^2 + \omega^2|W_x|^2 + \omega^2|W_y|^2 \right\rangle + (G/Re)\left\langle \text{Real}(TW_y^*)\right\rangle$$
$$- \text{Re}(Du_{yo})\left\langle \text{Real}(W_x W_y^*)\right\rangle - \text{Real}[W_y(0)DW_y^*(0)] = 0, \tag{15}$$

where the $\langle\ \rangle$ indicates integration from 0 to 1 in the x-direction and the * indicates the complex conjugate. The sum of the first four terms represents energy lost to viscous dissipation and is always negative. It is balanced by the sum of the remaining three terms. We denote the terms proportional to G and (Du_{yo}) as buoyant and shear terms, respectively. The remaining term W_yDW_y evaluated at $x = 0$ is due to the crystal-melt interface and would vanish for a rigid interface. In the results to be presented subsequently, we have found modes of instability for which one of the terms, i.e., buoyant, shear, or interface, is dominant.

The numerical methods used to solve the linear [illegible] defined by the differential equations [eqs. 12a-d] and the boundary conditions [eqs. 13-14] are all similar to those described previously [3]. We usually vary G and σ_i, keeping σ_r and all other parameters constant, until a solution of the differential equations is found which satisfies the boundary conditions. The program SUPORT [11] is used to solve the differential equations, and the program SNSQE [12-13] is used for the non-linear iteration procedure. Calculations of the critical Grashof number for the flow between two rigid plates are in agreement (to 4 significant figures) with Table 3 of Korpela, Gozum, and Baxi [14].

Numerical Results

For the calculations reported here, we have taken I = 0 (see eq. 10a) so that the net flow in the y-direction vanishes, and we choose our reference velocity U such that Re = G. Further we take $\Gamma = \varepsilon = 0$ and $k_r = P/P_S = 1$, i.e., we neglect both the crystal-melt surface energy and the density change during solidification, and we assume that crystal and melt have the same thermal properties. In most of our calculations we set $A = \nu H_v Re/k_s \Delta T = H_v g \alpha L^3/k_s \nu = 1.017(10^4)$, which corresponds to succinonitrile with L = 0.25 cm. The corresponding value of A for lead with L = 0.25 cm is A = 625. In general we calculate the onset of instability viz. $\sigma_r = 0$. For the Prandtl number P and all other parameters fixed, we calculate the Grashof number G and σ_i as functions of the spatial frequency ω for $\sigma_r = 0$. Typical results for succinonitrile P = 22.8 are shown in Figures 1-4. As previously discussed the instabilities can be characterized as buoyant, shear, or interface. For P = 22.8, the mode with the lowest Grashof number shown in Figure 1 is primarily an interface mode. The next highest branch represents a buoyant mode,

followed by a shear mode at higher va'ues of G. The interface mode is shown in more detail in Figure 2, where values of σ_i as a function of ω are also included. Note that $\sigma_i < 0$, meaning that the interface deformation propagates upward, whereas the base flow is downward near the interface. The buoyant mode is shown in Figure 3 and has a σ_i value three orders of magnitude greater than the interface mode. There is also a shear mode with a minimum Grashof number of 6200 shown in Figure 4.

The variation of the shear and buoyant modes of instability as a function of Prandtl number for the flow between two vertical rigid walls has been described by Gershuni and Zhukhovitskii [10]. In Figures 5-7, we show the behavior of the various modes as a function of Prandtl number for the crystal-melt interface. Figure 5 shows the minimum Grashof number (as a function of ω) as the Prandtl number varies. In Figures 6 and 7, we have plotted σ_i and ω, respectively, as a function of Prandtl number; the σ_i and ω curves correspond to minimum values of the Grashof number as a function of ω. The buoyant mode, which has a large value of σ_i and a large wave speed (comparable to the unperturbed flow velocity), is hardly affected by the presence of the crystal-melt interface, and is essentially identical to the buoyant mode for a rigid boundary. For high values of the Prandtl number the Grashof number for the interface mode is two orders of magnitude lower than the Grashof number for the shear mode of instability. As the Prandtl number decreases, the interface and shear modes approach each other, while the Grashof number for the buoyant modes rises abruptly and is much larger than the Grashof number for the shear mode for Prandtl numbers less than 10.

At a Prandtl number of 2.5, a plot of Grashof number as a function of ω, shown in Figure 8, has two minima, which correspond to the two Grashof numbers appearing in Figure 3. The size of each of the last three terms appearing in eq. (15) are shown in Figure 9; that is, the shear term (dashed line), the buoyant term (dot-dashed line), and the interface term (solid line). Positive values indicate a destabilizing influence since the term tends to increase the kinetic energy of the disturbance to the main flow, whereas negative values indicate a stabilizing influence. At wavenumbers less than unity, the interface term dominates the instability, while for wavenumbers greater than two, the shear term is driving the disturbance.

As the Prandtl number is decreased, Figures 10-17, the second minimum in Grashof number, corresponding to the shear mode, disappears (cf. Figure 3). Both shear and interface terms are significant for the remaining minimum. As P is further reduced, the wavenumber at the minimum Grashof number increases and the effect of the interface term becomes less and less significant. For Prandtl number P = .01, Figures 16 and 17, the crystal-melt interface term is negligible and the shear mode drives the disturbance.

In Figures 18-20, we show results for lead with L = 0.25 cm, Λ = 625, P = 0.0225, P_s = 0.012, k_r = 0.535, and $\gamma = \varepsilon = 0$, for both the crystal-melt interface and a rigid boundary. The Grashof number as a function of ω is essentially independent of the type of boundary. For a rigid boundary $\sigma_i = 0$, while for the crystal-melt interface $\sigma_i = -2.7$ at the minimum value of the Grashof number of 7630. This corresponds to a period of oscillation of 60 s.

References

1. S. R. Coriell and R. F. Sekerka, PhysicoChemical Hydrodynamics 2, 281 (1981).
2. R. T. Delves, Crystal Growth (edited by B. R. Pamplin) Vol. 1, 40, (1974).
3. S. R. Coriell, M. R. Cordes, W. J. Boettinger, and R. F. Sekerka, J. Crystal Growth 49, 13 (1980).
4. J. I. Mickalonis, M. S. Thesis, Materials Engineering Department, Rensselaer Polytechnic Institute, Troy, NY (1982).
5. M. E. Glicksman and J. I. Mickalonis, Proceedings of the 16th Southeastern Seminar on Thermal Sciences, Miami, Florida, 1982.
6. S. R. Coriell, R. F. Boisvert, J. I. Mickalonis, and M. E. Glicksman, Adv. in Space Research (proceedings of the 24th COSPAR Meeting) 3, 95 (1983).
7. Q. T. Fang, M. S. Thesis, Materials Engineering Department, Rensselaer Polytechnic Institute, Troy, NY (1983).
8. I. G. Choi and S. A. Korpela, J. Fluid Mech. 99, 725 (1980).
9. A. H. Shaaban and M. N. Ozisik, 7th International Conference of Heat Transfer, Munich, Germany (1982).
10. G. Z. Gershuni and E. M. Zhukhovitskii, Convective Stability of Incompressible Fluids, Keter, Jerusalem, 1976.
11. M. R. Scott and H. A. Watts, SIAM J. Numerical Anal. 14, 40 (1977).
12. SLATEC Common Math Library, The Program SNSQE was written by K. L. Hiebert and is based on an algorithm of Powell [13].
13. M. J. D. Powell, in: Numerical Methods for Nonlinear Algebraic Equations, ed. P. Rabinowitz, Gordon and Breach, NY (1970).
14. S. A. Korpela, D. Gozum, C. B. Baxi, Int. J. Heat Mass Transfer 16, 1683 (1973).

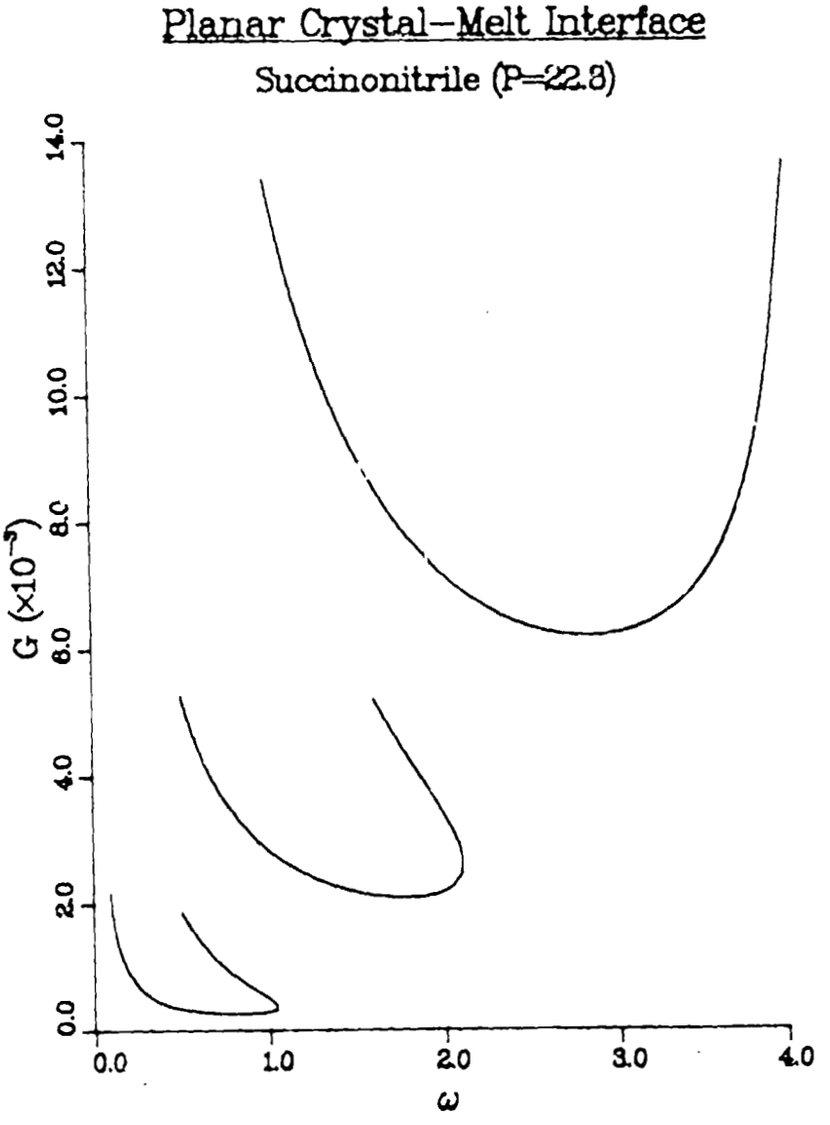

Fig. 1. The Grashof number, G, at the onset of instability as a function of the spatial frequency, ω, of a sinusoidal perturbation for Prandtl number, P, of succinonitrile, viz., P = 22.8. The three curves correspond to different modes of instability.

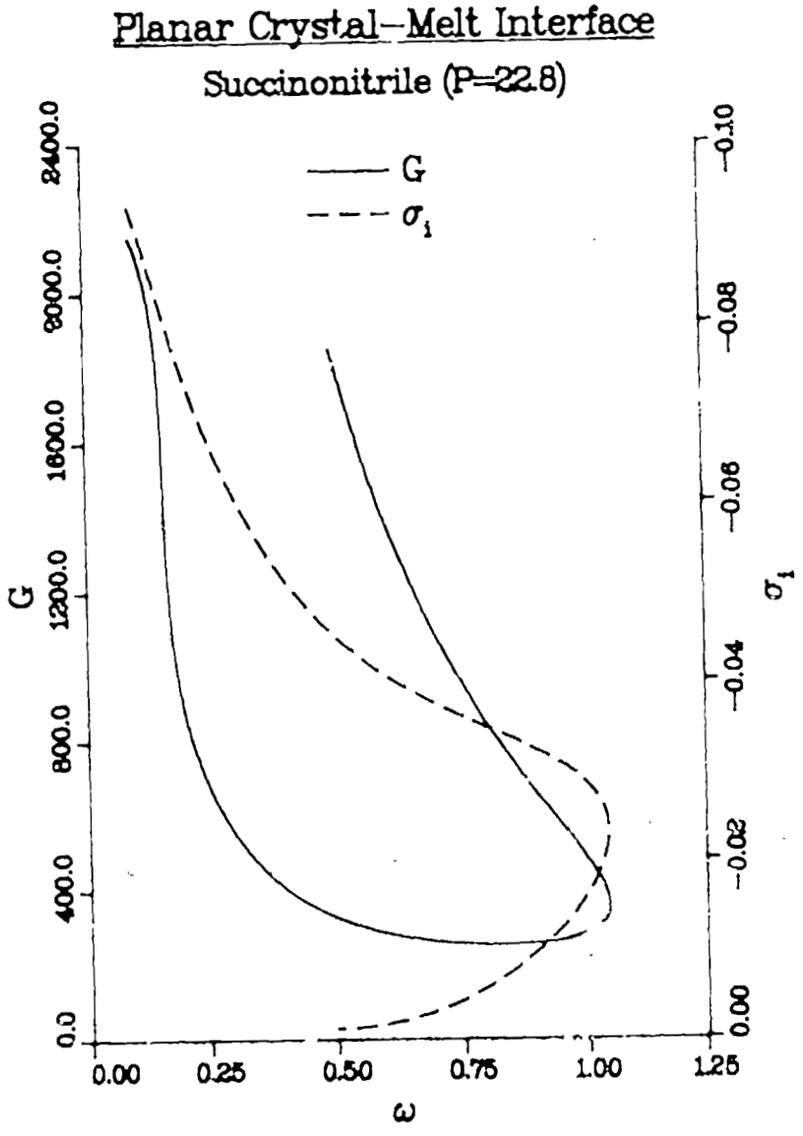

Fig. 2. The Grashof number (solid curve, left ordinate) and the imaginary part of the time constant, σ_i, (dashed curve, right ordinate) as a function of the spatial frequency, ω, of a sinusoidal perturbation for Prandtl number of 22.8. The solid curve is identical to the lower curve of Fig. 1.

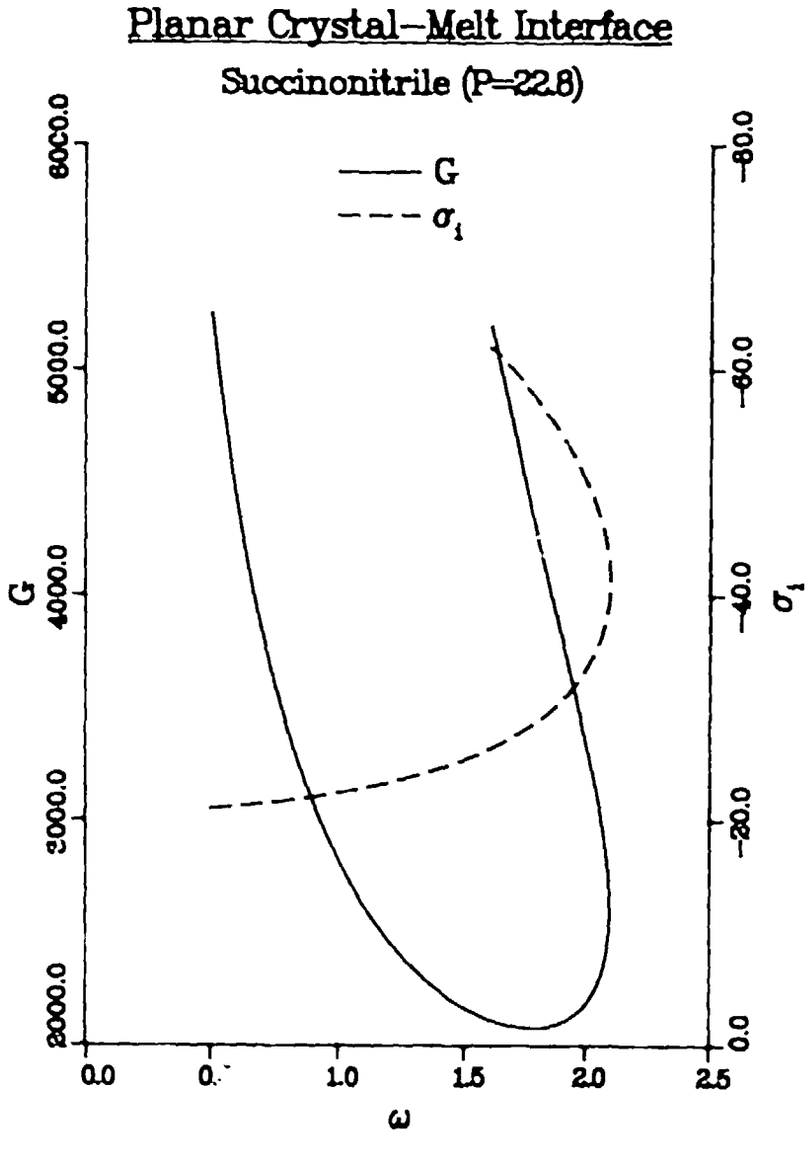

Fig. 3. The Grashof number (solid curve, left ordinate) and the imaginary part of the time constant, σ_i, (dashed curve, right ordinate) as a function of the spatial frequency, ω, of a sinusoidal perturbation for Prandtl number of 22.8. The solid curve is identical to the middle curve of Fig. 1.

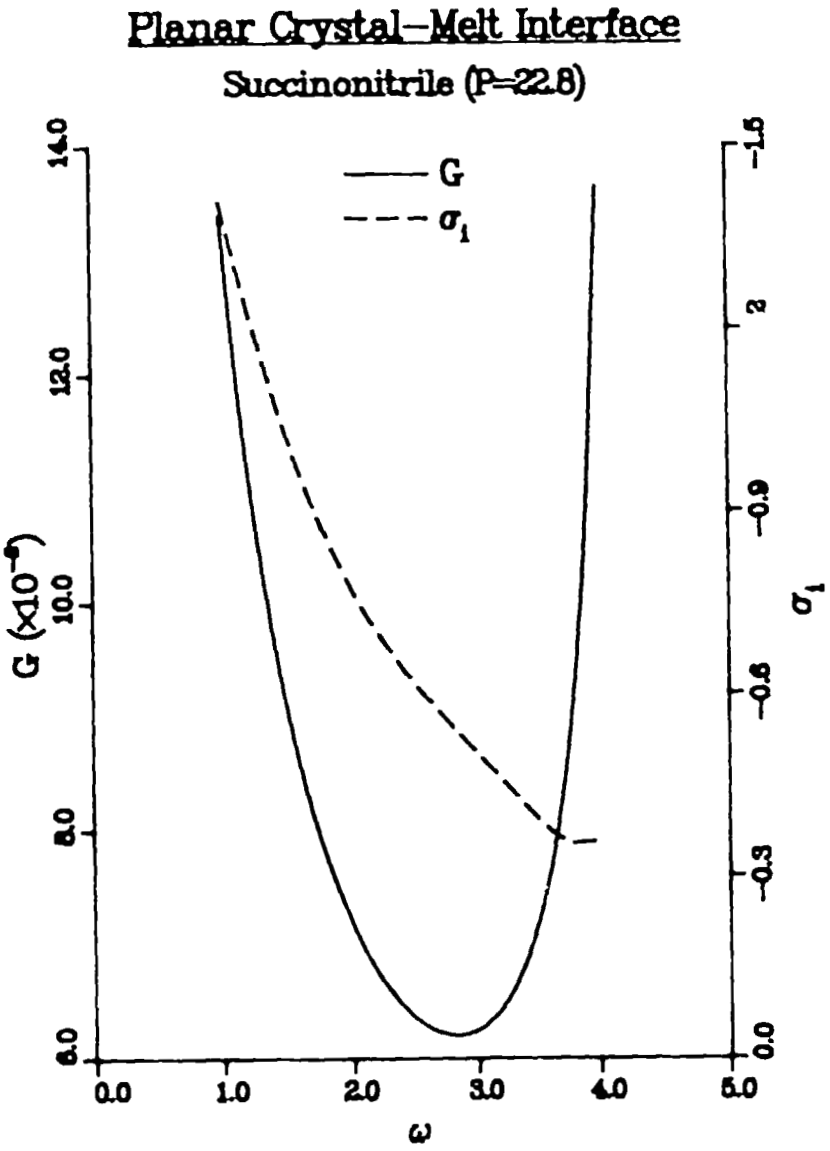

Fig. 4. The Grashof number (solid curve, left ordinate) and the imaginary part of the time constant, σ_1, (dashed curve right ordinate) as a function of the spatial frequency, ω, of a sinusoidal perturbation for Prandtl number of 22.8. The solid curve is identical to the top curve of Fig. 1.

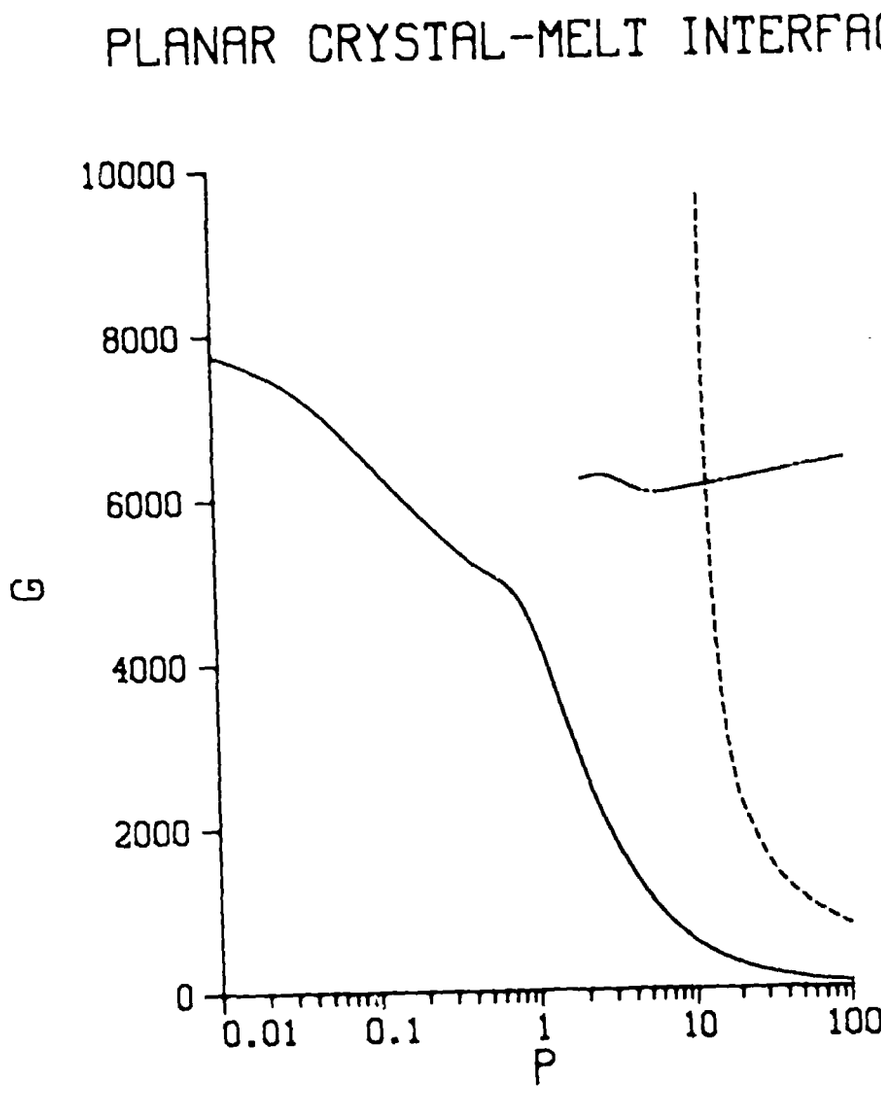

Fig. 5. The minimum Grashof number (as a function of spatial frequency) as a function of Prandtl number. For large values of the Prandtl number, three different modes of instability occur.

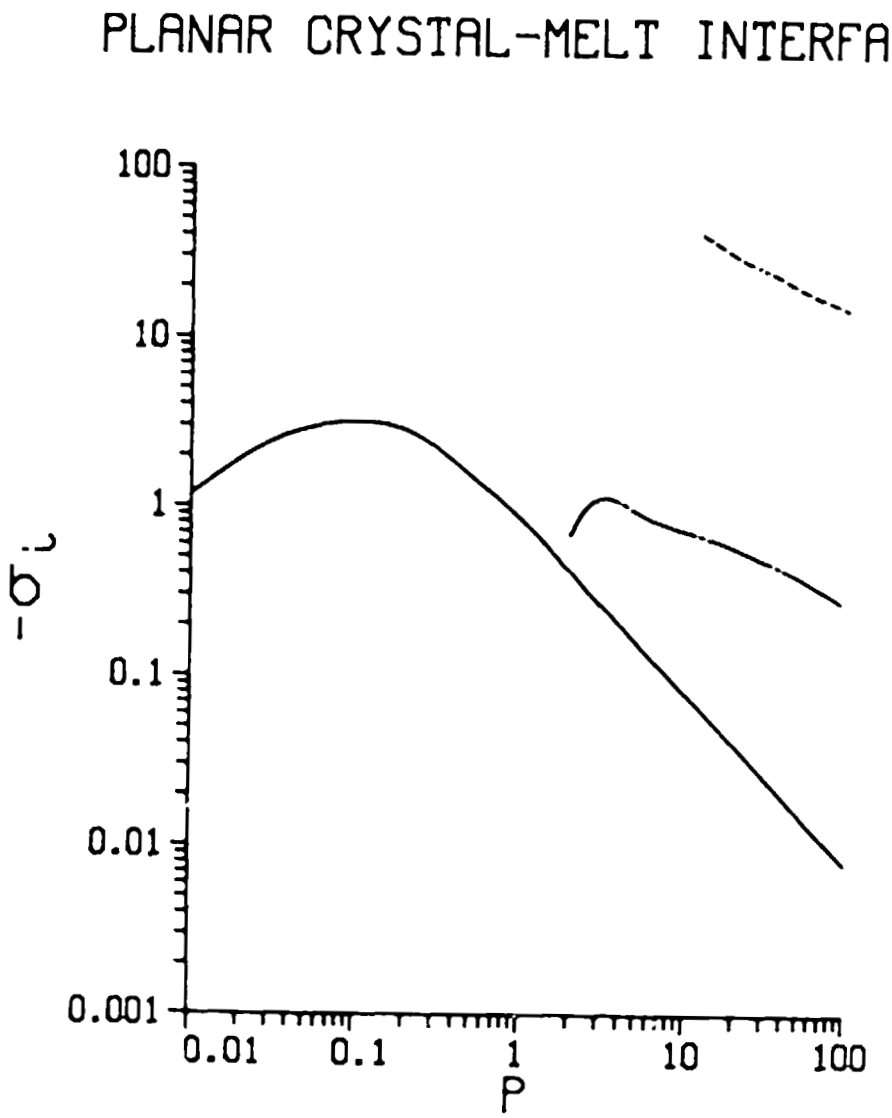

Fig. 6. The imaginary part of the time constant, σ_i, (corresponding to the minimum values of the Grashof number as a function of ω) as a function of Prandtl number.

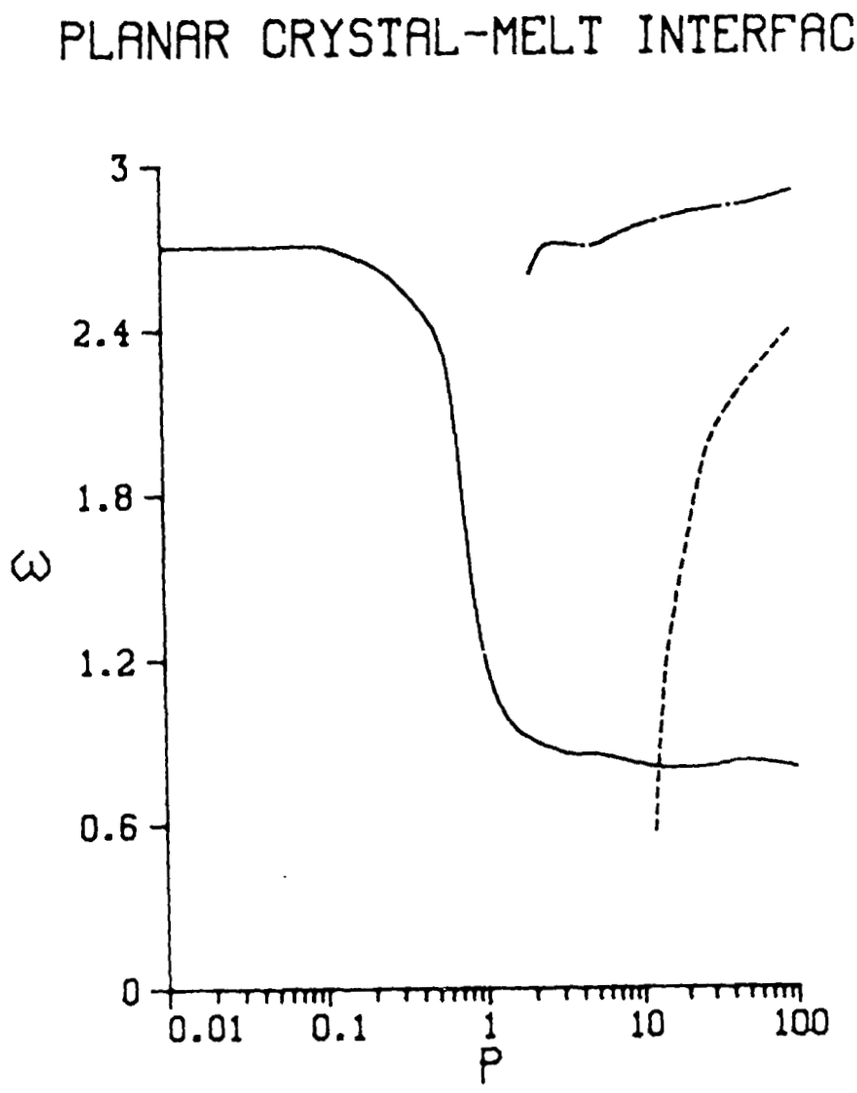

Fig. 7. The spatial frequency, ω, (at the minimum value of the Grashof number) as a function of the Prandtl number.

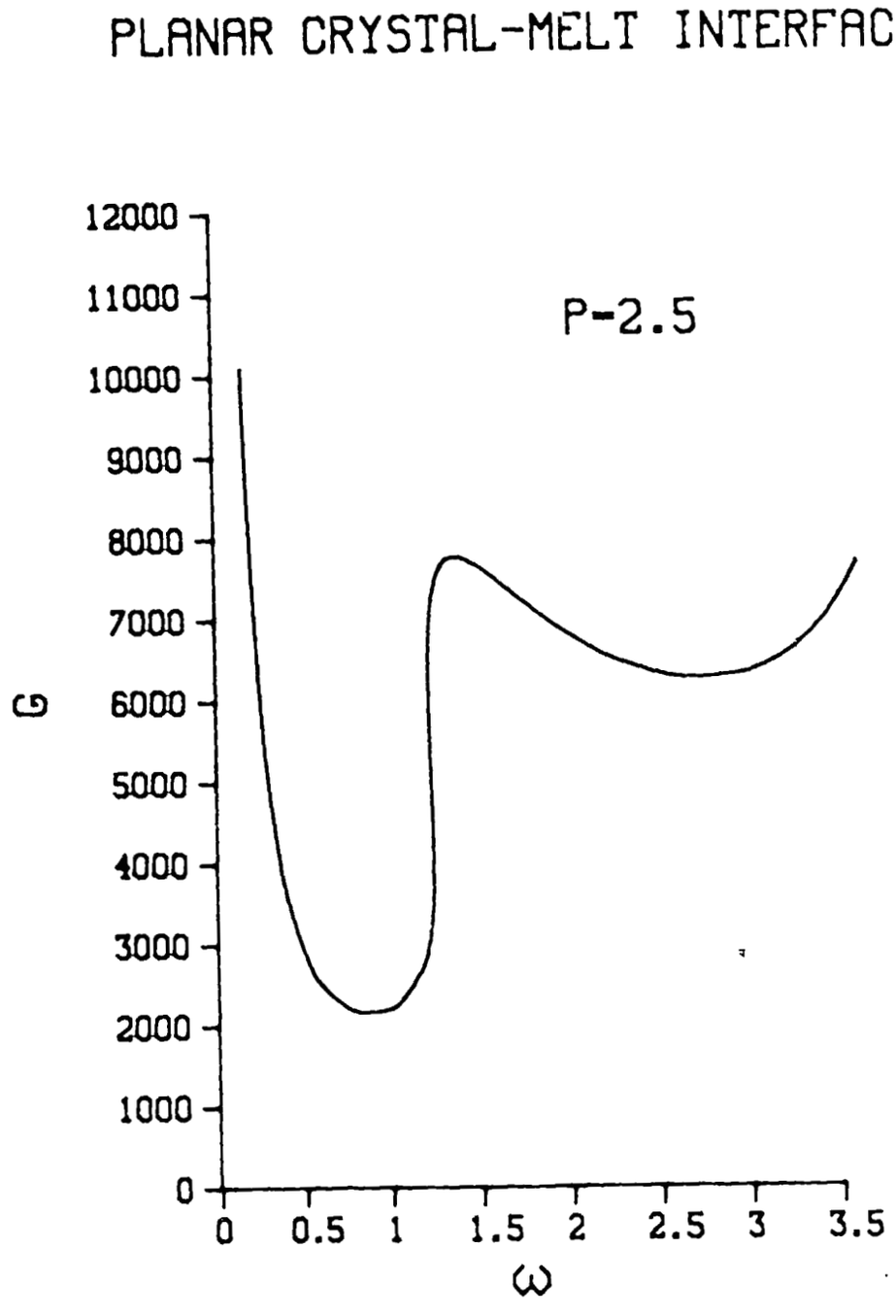

Fig. 8. The Grashof number, G, at the onset of instability as a function of the spatial frequency, ω, of a sinusoidal perturbation for Prandtl number, P, of 2.5.

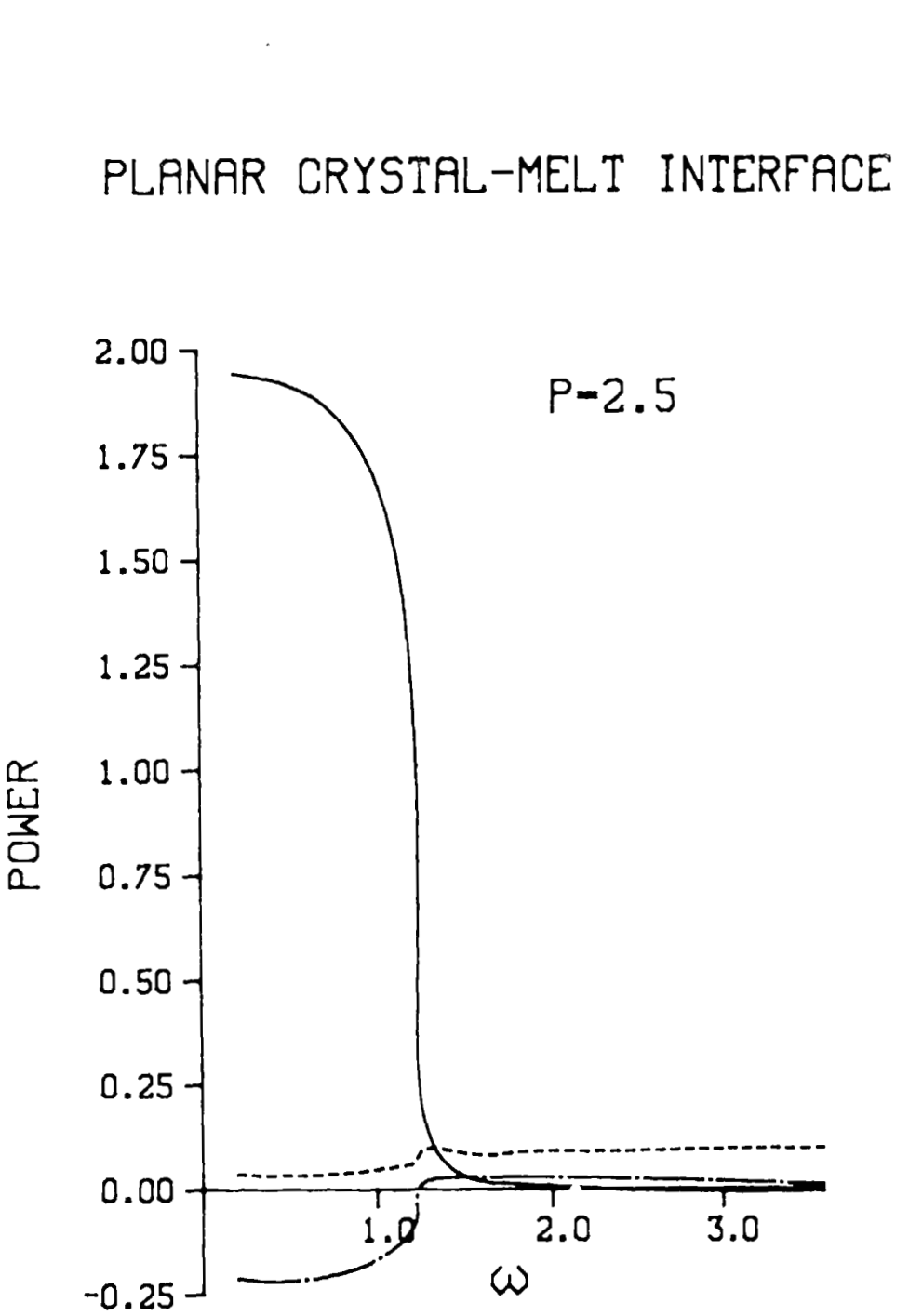

Fig. 9. The interface (solid curve), shear (dashed curve), and buoyant (dot-dashed curve) contributions to the rate of change of the average kinetic energy (power) of an instability as a function of spatial frequency for Prandtl number of 2.5.

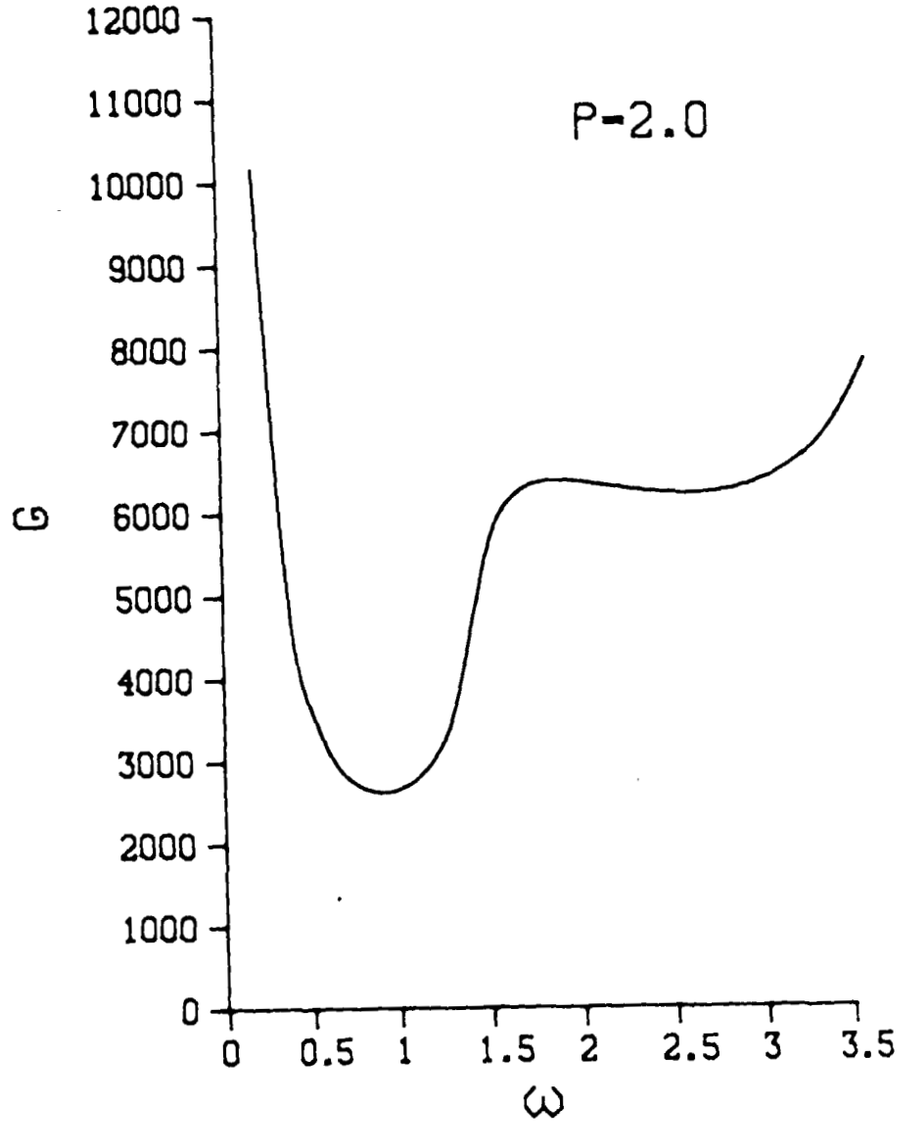

Fig. 10. The Grashof number, G, at the onset of instability as a function of the spatial frequency, ω, of a sinusoidal perturbation for Prandtl number, P, of 2.0.

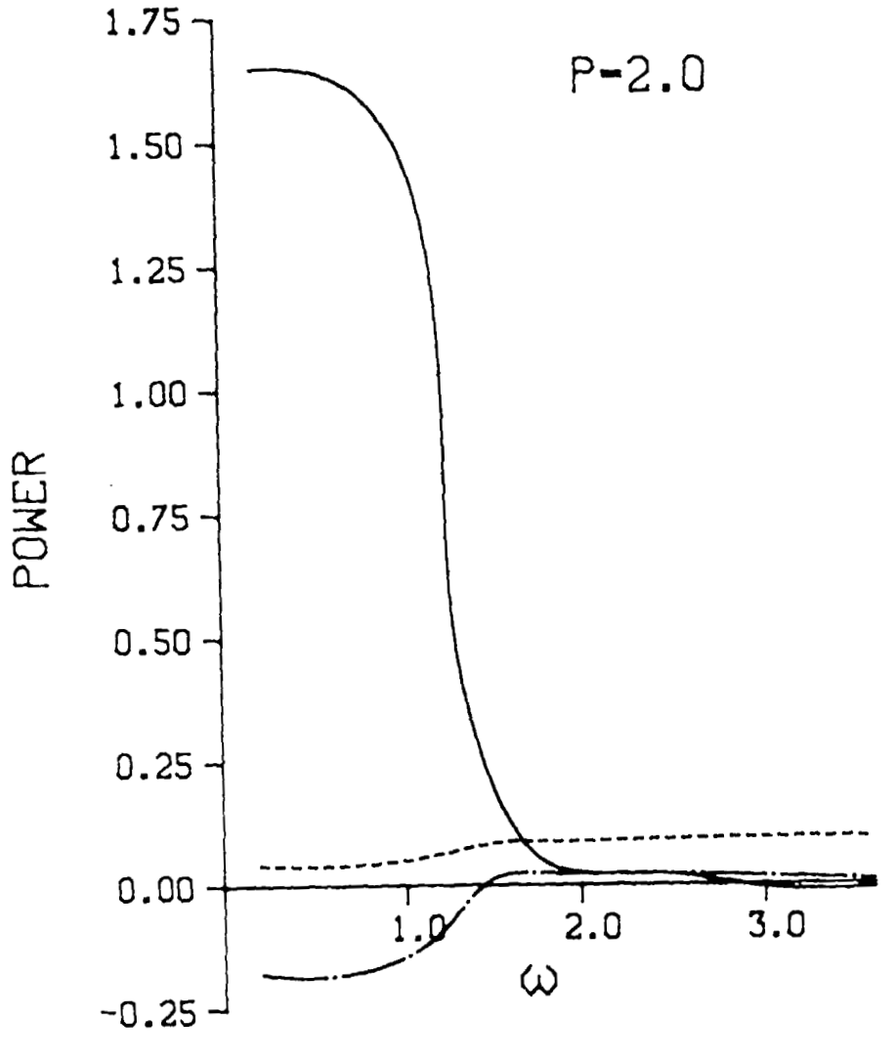

Fig. 11. The interface (solid curve), shear (dashed curve), and buoyant (dot-dashed curve) contributions to the rate of change of the average kinetic energy (power) of an instability as a function of spatial frequency for Prandtl number of 2.0.

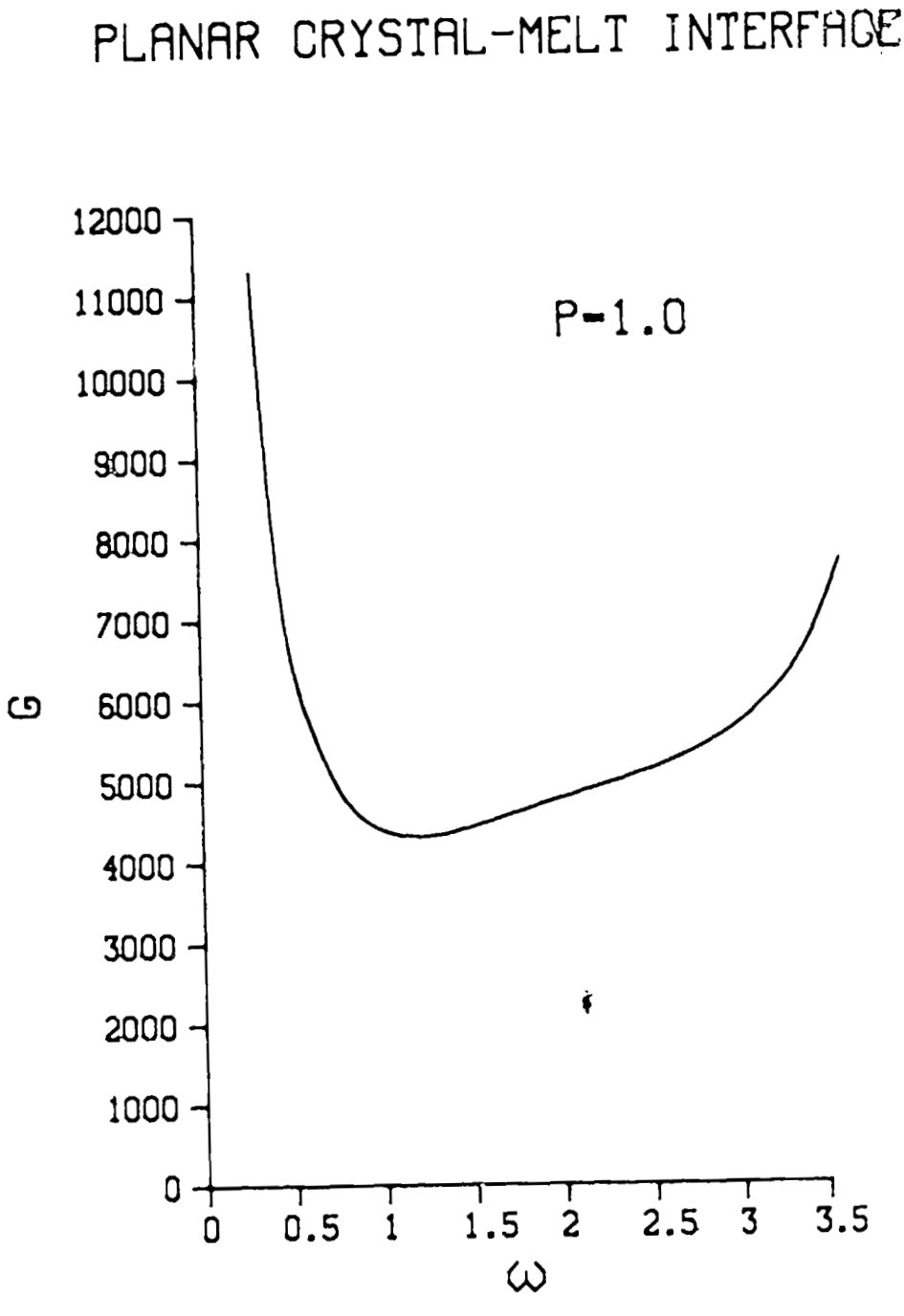

Fig. 12. The Grashof number, G, at the onset of the instability as a function of the spatial frequency, ω, of a sinusoidal perturbation for Prandtl number, P, of 1.0.

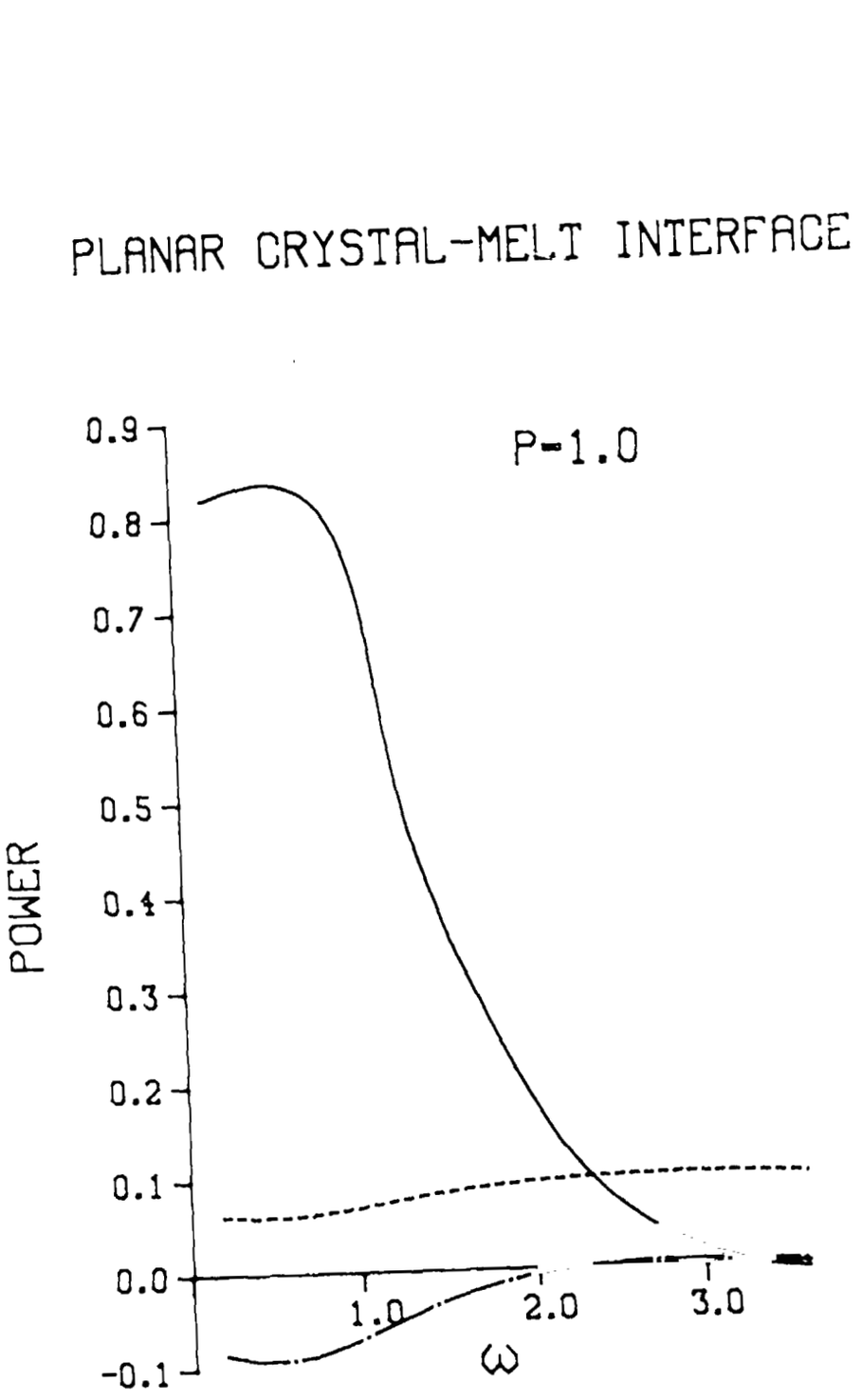

Fig. 13. The interface (solid curve), shear (dashed curve), and buoyant (dot-dashed curve) contributions to the rate of change of the average kinetic energy (power) of an instability as a function of spatial frequency for Prandtl number of 1.0.

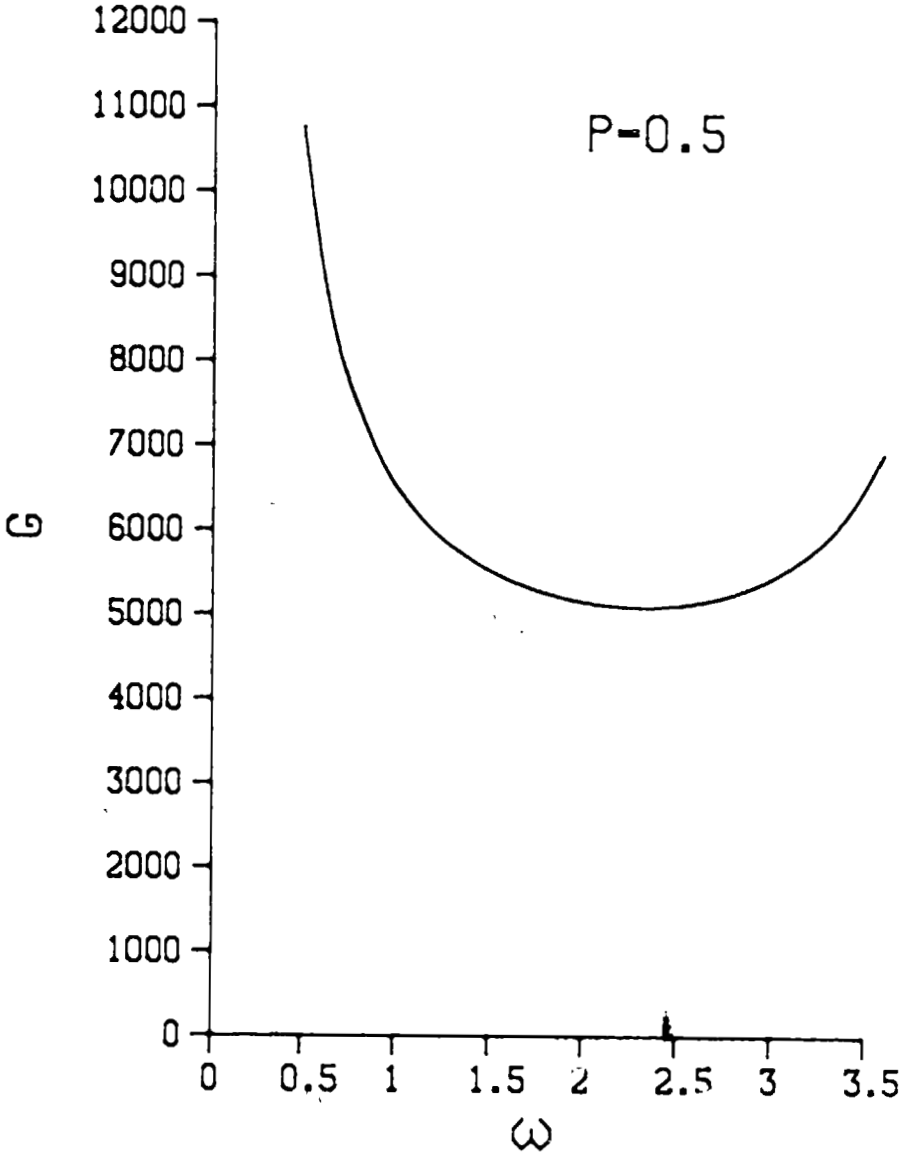

Fig. 14. The Grashof number, G, at the onset of instability as a function of the spatial frequency, ω, of a sinusoidal perturbation for Prandtl number, P, of 0.5.

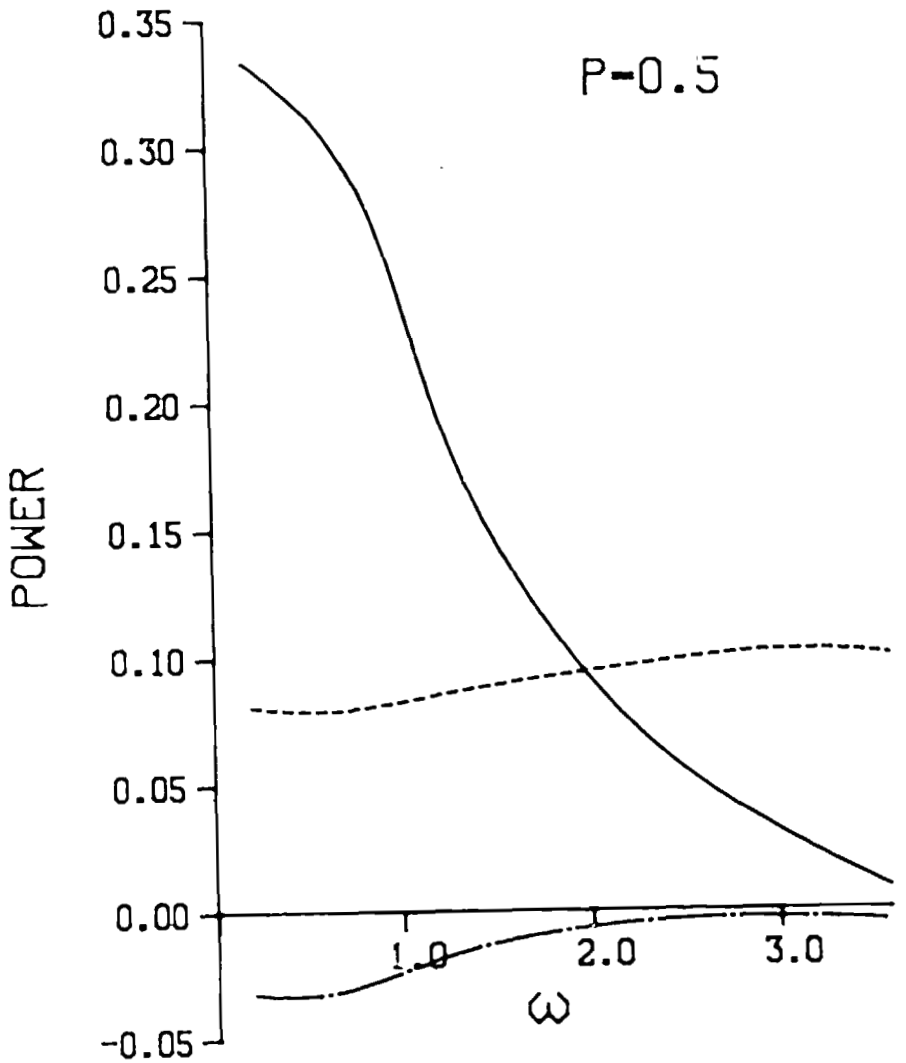

Fig. 15. The interface (solid curve), shear (dashed curve), and buoyant (dot-dashed curve) contributions to the rate of change of the average kinetic energy (power) of an instability as a function of spatial frequency for Prandtl number of 0.5.

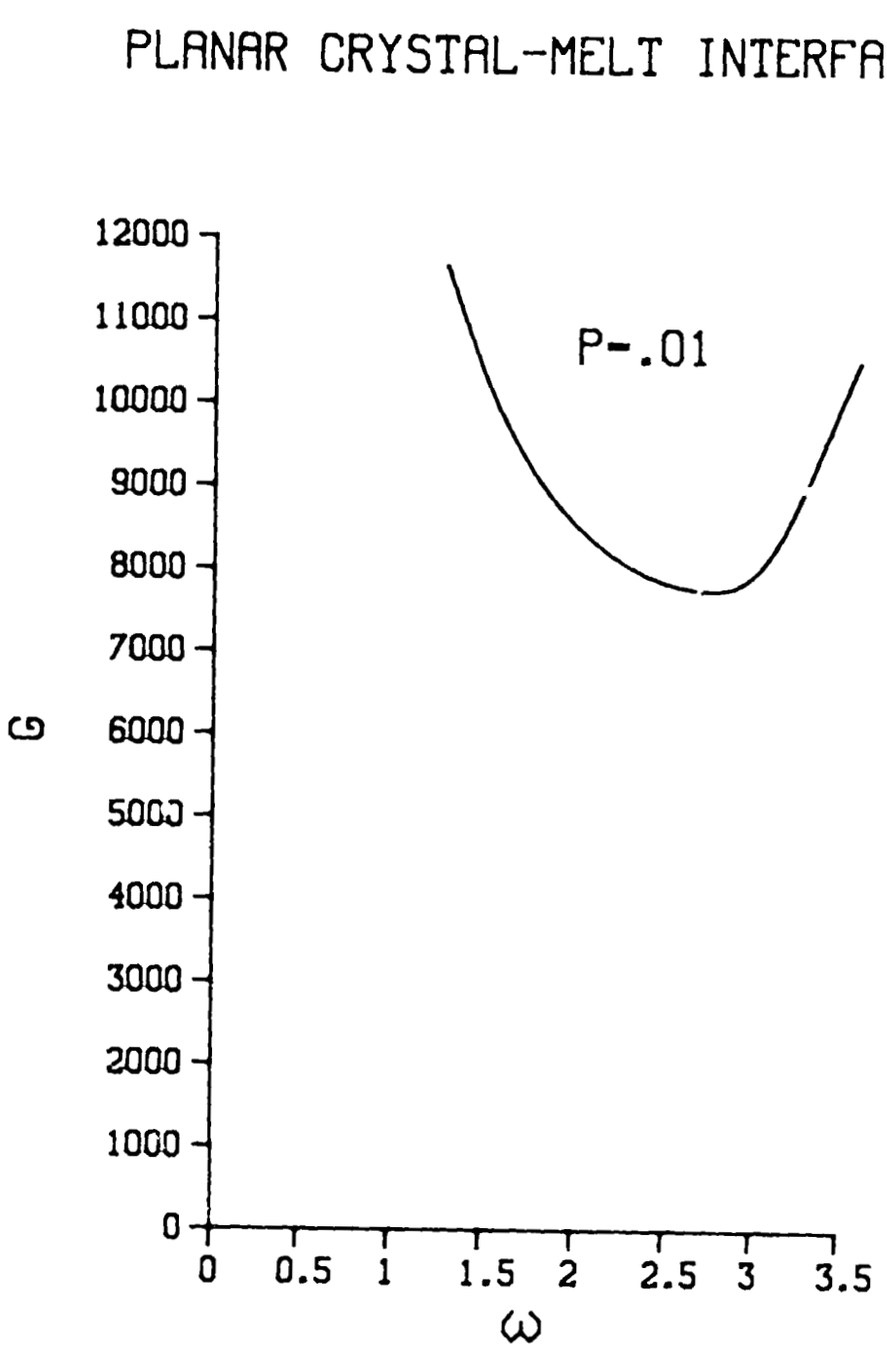

Fig. 16. The Grashof number, G, at the onset of instability as a function of the spatial frequency, ω, of a sinusoidal perturbation for Prandtl number, P, of 0.01.

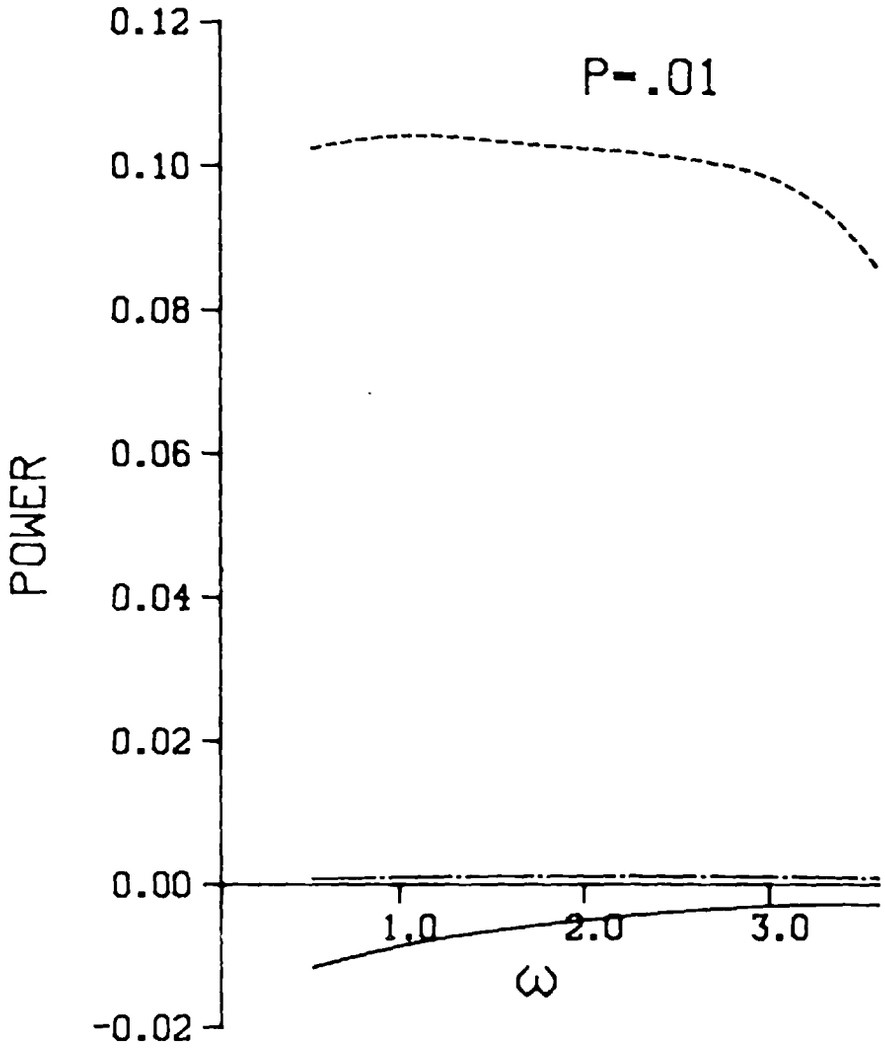

Fig. 17. The interface (solid curve), shear (dashed curve), and buoyant (dot-dashed curve) contributions to the rate of change of the average kinetic energy (power) of an instability as a function of spatial frequency for Prandtl number of 0.01.

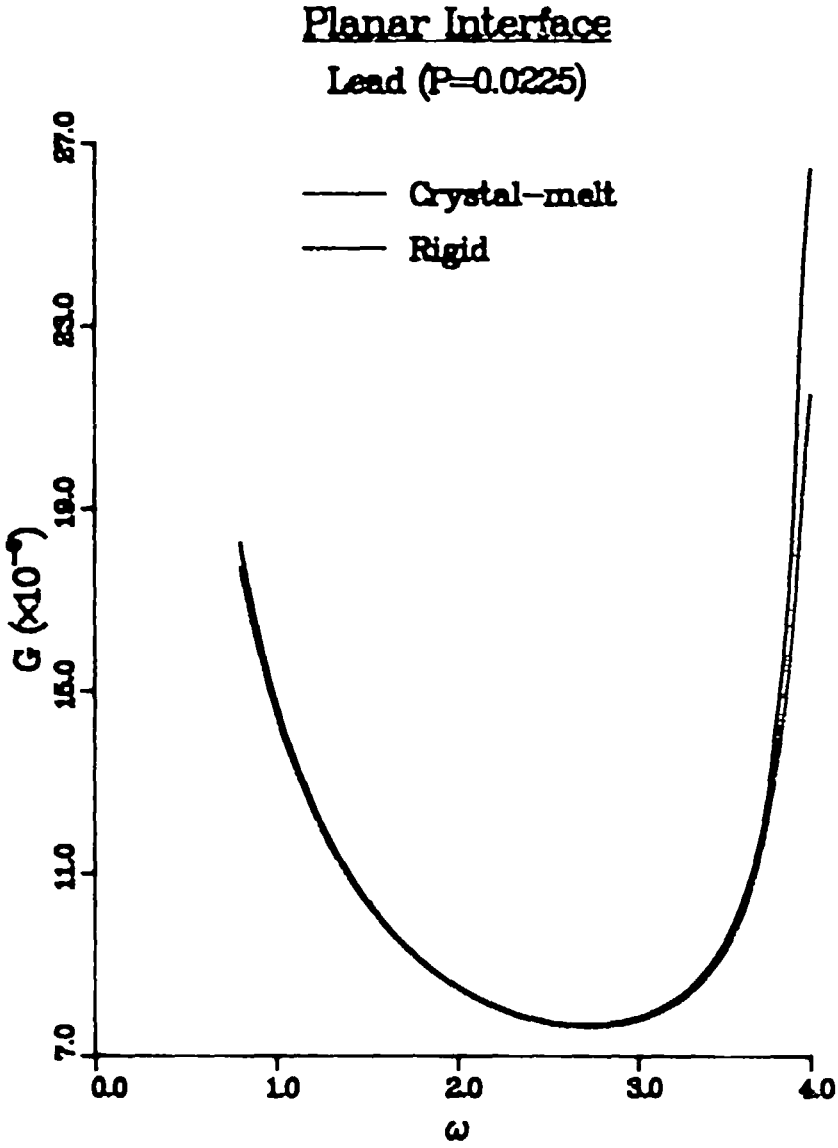

Fig. 18. The Grashof number, G, at the onset of instability as a function of the spatial frequency, ω, of a sinusoidal perturbation for Prandtl number, P, of lead, viz., P = 0.0225. The solid curve corresponds to a rigid interface while the dot-dashed curve corresponds to a crystal-melt interface.

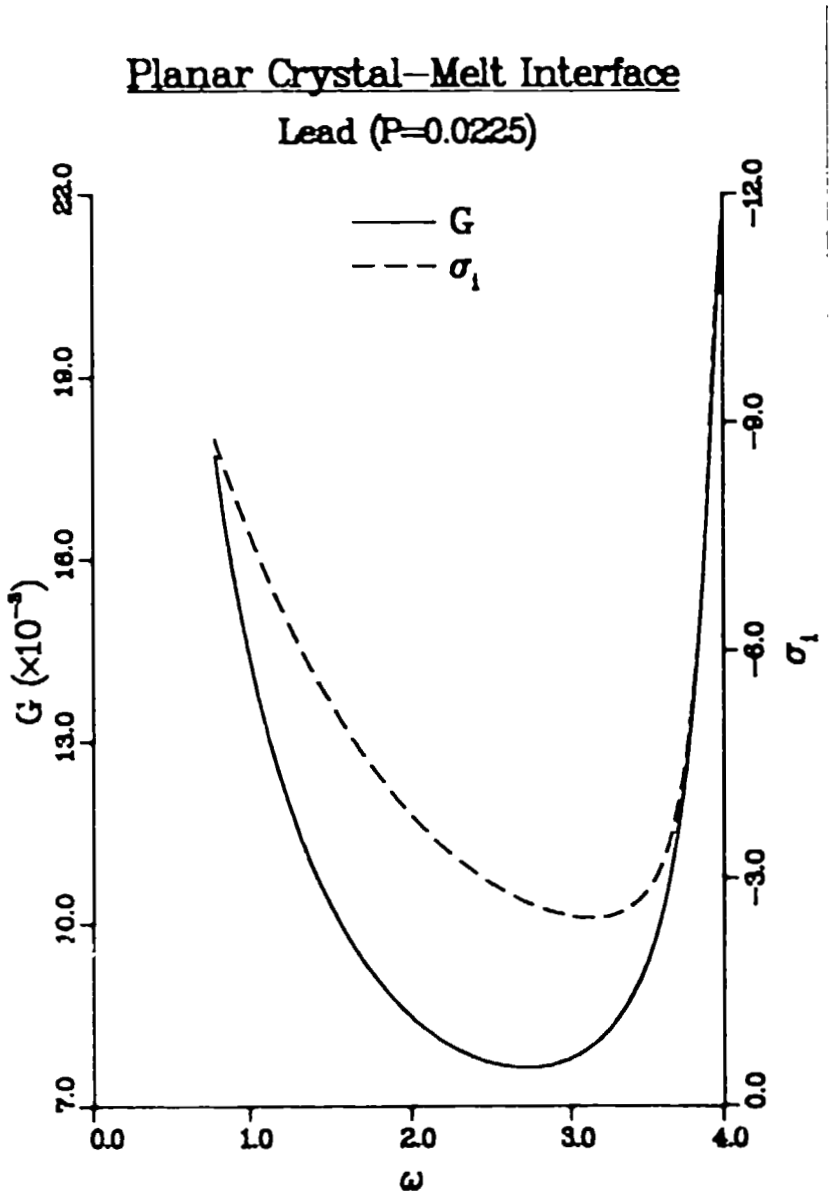

Fig. 19. The Grashof number (solid curve, left ordinate) and the imaginary part of the time constant, σ_1, (dashed curve, right ordinate) as a function of the spatial frequency, ω, of a sinusoidal perturbation for Prandtl number of 0.0225. The solid curve is identical to the dot-dashed curve of Fig. 18.

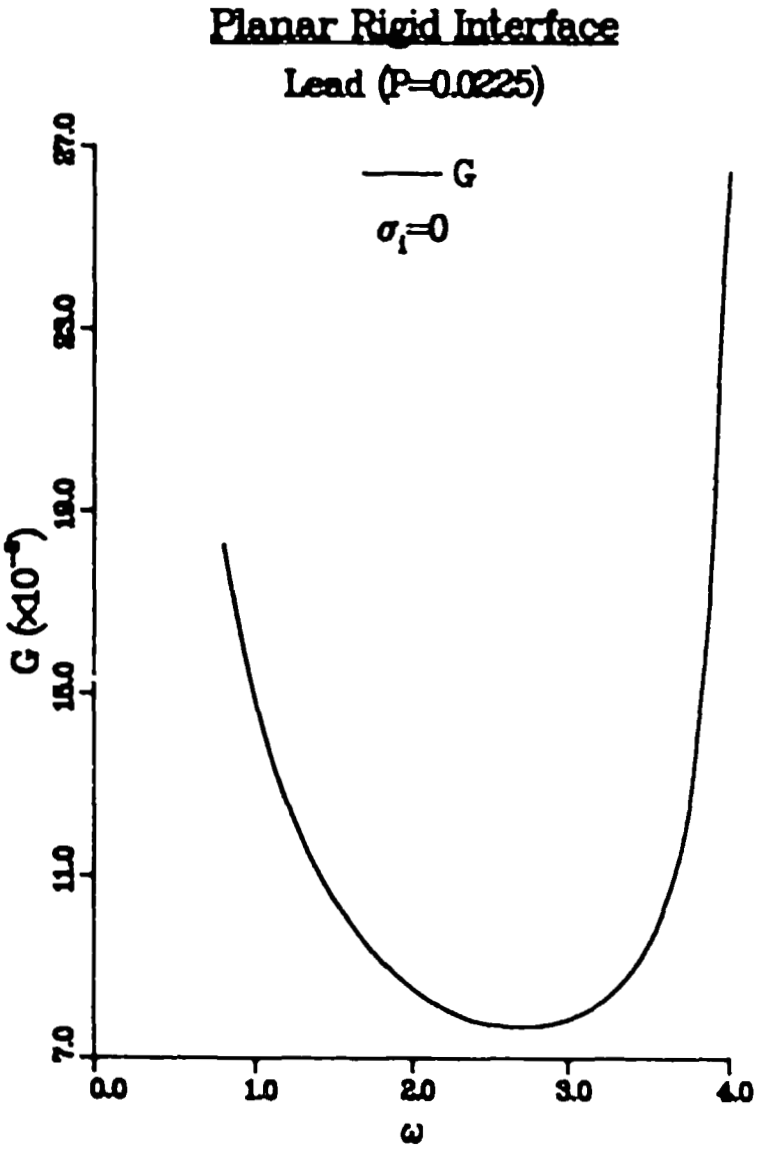

Fig. 20. The Grashof number as a function of the spatial frequency, ω, of a sinusoidal perturbation for Prandtl number of 0.0225. The solid curve is identical to the solid curve of Fig. 18. The imaginary part of the time constant vanishes.

Task 3

Measurement of The High Temperature Thermophysical Properties of Tungsten Group Liquids and Solids

D. W. Bonnell

Materials Chemistry Division

Center for Materials Science

SUMMARY

The General Electric Space Systems Division (GE) developed prototype "gulp" calorimeter has been tested in joint Rice University (RICE) and The National Bureau of Standards (NBS) experiments by dropping levitated tungsten solid at 2800 K, and found to function mechanically to perfection. The steps necessary to establish this device as a working calorimeter for both ground and potential space applications is discussed. The central problems remaining are the addition of calorimetric temperature measurement hardware precise to 0.001 K and resistant to electromagnetic interferance, the development of techniques to achieve 0.1 percent enthalpy determination uncertainty with expected 18 K temperature rises, and direct calibration of the calorimeter.

The concentration of effort to measurements at the melting point of liquid tungsten have yielded the first reported direct measurement of the heat of fusion of tungsten. The value obtained was 53.0 ± 2.3 kJ/mole (12.7 ± 0.5 kcal/mole) and, in comparison with estimates and previous indirect methods, is considered to be a current best value.

INTRODUCTION

The primary objective of this task is to develop, in conjunction with General Electric Space Systems Division (GE) and Rice University (RICE), the techniques, methodology, and experimental apparatus for measuring thermophysical properties (e.g. heat of fusion, enthalpy increment, heat capacity) of materials at extremely high temperatures. Electromagnetic levitation of conductive samples using auxiliary heating techniques such as electron-beam heating has been coupled to a drop-type block calorimeter system. Specific application to tungsten has been a prime area of interest because it is the highest melting element. Measurements of tungsten are crucial for estimation of the thermophysical properties of othe elements by correlation. The third long period transition elements have all proved to be difficult to measure directly, and little data is available for VIB and VIIB elements in spite of their importance both scientifically and for engineering purposes. Accurate data are necessary to encourage further theoretical investigation of the liquid state at high temperature. Modern computer capacities promise new models based on detailed evaluation by molecular/atomic dynamics [1], but will require validation by experimental determination of definitive thermophysical properties.

The technical difficulty of this effort has provided a measure of the dividing line between experiments which can be performed in the terrestrial environment, and those which require the absence of gravity for successful accomplishment. Continued advance of ground based efforts seems at present the clearest means to successful future experiments in space, as considerable hardware development is still necessary to take advantage of the low-gravity environment.

GULP CALORIMETRY

In the initial development of the levitation technique, it was recognized that the technique was a method to gain the advantage of non-material support in a one gravity field, giving many of the advantages of the space micro-gravity environment. The technique's application to the measurement of the heat content of levitated materials added a separate requirement, whose simplest solution is the "drop" calorimeter technique, in which gravity provides a rapid and hence approximately isothermal transfer of the sample from the high temperature state into contact with a calorimetric mass whose temperature is near the reference state. A significant problem in conducting similar high temperature calorimetry in space is the transfer of a sample to the calorimeter without the aid of gravity and without giving up the advantages of the containerless environment. The problem is not insuperable. Acoustic positioning techniques are capable of manipulating levitated objects [2-4] but the acoustic techniques still appear to have severe materials problems to overcome at the very high temperatures which are of greatest interest, and are most difficult to achieve in a controlled fashion on the ground. Electrostatic techniques are possible [5] and can be used in a vacuum, an important advantage where some methods of auxiliary heating need to be used. Less well conceived and apparently untested are techniques using an electromagnetic pulse to move a sample. Such a method would be difficult to develop in a one-g environment in conjunction with RF levitation. Since the design of ground based levitation coils is still somewhat of an art, another method was sought. In 1974, this investigator made the suggestion that it would be more straightforward to attempt to move the calorimeter instead, and J. L. Margrave of Rice University coined the name "gulp" calorimeter for this technique.

The advent of Space Shuttle experiment opportunities has made this problem an important one, as high temperature calorimetry is one of the most obvious kinds of science certain to benefit from the advantages of space for experimentation. General Electric Space Laboratories has undertaken a ground pilot development of a "gulp" calorimeter. NBS expertise has been sought in this connection in an advisory capacity, since use of the device on the ground would almost certainly occur within the framework of the current GE/RICE/NBS levitation effort. The final development by GE [6] is a excellent application of mechanical engineering ingenuity, and closely mimics the behavior a space-based device must have. Certain compromises were necessary. A primary one is the physical size of the calorimeter. Traditional drop calorimeters are designed for total heat rises of the order of one degree to minimize the temperature difference between calorimeter and surroundings. The mathematical basis for data analysis of the thermal behavior of an isoperibol (drop-type) calorimeter [7,8] invokes a linear approximation of the combined effects of the exponential Newton's law of cooling (conduction/convection) and the power law radiation transfer process. This approximation is generally excellent (better than 0.0005 average percent deviation per 10 second measurement period over 10-20 minute intervals where calorimeter block/jacket temperature differences are 1 - 2 degrees [8]). This linear relationship is used to determine when the calorimeter has equilibrated with the heat input from the sample and, more importantly, to correct for the heat contribution to/from the calorimeter during the equilibration time of calorimeter with sample. For typical equilibration times of ca. 3000 seconds, worst case error from this source is less than 0.1 percent and thus negligible in measurements of a few tenths percent overall accuracy.

The GE calorimeter prototype was designed to be tested on the ground, and to be a reasonable model (i.e., physical overall dimensions and system total mass) for a flight system. In addition, capture times were required to be as short or shorter than ground experimental arrangements, to minimize radiation losses from the sample. A pnuematic actuation system was chosen by GE as the most reasonable system capable of the required speed of operation with significant masses. This choice limited the moving mass of the calorimeter to the order of one kg, approximately 5 percent of the current ground calorimeter. Predicted heat rises for 10 gm samples of freezing liquid tungsten at 3695 K are about 18 K. No isoperibol calorimeter has apparently been reported using such large heat increases. By the above analysis, one would assume that existing data analysis techniques would cause the error from such large calorimeter/jacket temperature differences to contribute at least one percent to the uncertainty of the heat measurement. In addition, widespread practice has determined, for calorimeters with 1 atmosphere gas pressure (at 1 gravity) in the jacket region, that a jacket/calorimeter gap of the order of 1 cm yields the best uniformity of convection driven temperature transfer. This was a difficult structural requirement, and was ignored for prototype purposes, as this system is expected to operate in vacuum. Operated in atmosphere the gulp calorimeter system would require careful calibration to establish its true heat capacity behavior and the thermal effects of movement as a function of differential temperature. Even restriction to operation in vacuum below the 10 Pa (0.0001 atm) point, where gas thermal conduction becomes much less significant, will still require attention, as the radiation transfer, and incidental mechanical connection conduction will not be negligible. At the moment, there is just too little experimental data available to make such corrections a priori.

There are two possible solutions to this problem: 1) new numerical techniques for evaluation of the true thermal exchange process; and/or 2) controlling the jacket temperature to track the block temperature - a form of adiabatic calorimetry. For the first, both the radiation and conduction processes have well defined functional forms, and a direct determination of the net transfer coefficients for the two processes should be relatively easy to model from experimental calibrations, although separating the two processes may prove difficult. The hardware solution, using the surface temperature of the calorimeter as a control signal to heaters controlling all "jacket" surfaces near the calorimeter at the calorimeter surface temperature is quite attractive. This adiabatic wall process is used extensively in calorimetry where large temperature excursions are routine (e.g. low temperature calorimetry and differential scanning calorimetry) and involves only existing commercially available technology. Although the gulp calorimeter system is considerably more massive, and has both a much more complicated physical geometry and more complicated thermal pathways than the above examples, a combination of the above two methods should make high accuracy calorimetry possible with the prototype design.

The GE designed calorimeter uses a pnuematic ram with special high speed valves to move the calorimeter from its rest position to the capture region. For ground based testing, this location is just below the work coil, with clearance for the momentum opened calorimeter gate. Timing and capture trials with levitation heated samples of tungsten were conducted with the prototype instrument as a joint GE/RICE/NBS experimental effort. The calorimeter ram and gates were instrumented by GE to allow oscillograms of the time trajectory of the calorimeter to be obtained and to detect when, in that trajectory, the block radiation gates were fully open [6]. A simple time delay relay was

inserted in the signal line from the drop detector (originally constructed for tungsten experiments) which triggers the capture cycle. The delay was adjusted to retard the pnuematic impulse about 0.02 sec until the timing oscillogram intersected the falling sample location in the middle of the gate open time. The block radiation gate is counterweighted to open inertially as the calorimeter accelerates, and to close by momentum as the calorimeter stops at maximum excursion. The calorimeter system adapter to the levitation chamber was designed to limit excursion to a location approximately 4 cm below the levitation point (about 2 cm below the drop detector location), allowing clearance for the coil and pedestal assembly [for experimental details, see reference 9]. The calorimeter mount has a pair of overlapping radiation shutters which are opened by cams moving with the calorimeter. The calorimeter is just beginning to open the block gates as it passes the point of opening the main external shutters, and the block gate open time of more than 0.05 sec allowed several centimeters leeway in sample location at "capture" (defined for this purpose as the time the sample crossed the gate hinge plane and would be retained by the closing gates, rather than possibly having some of the sample ejected). A capture point corresponding to a drop distance of about 7 cm (0.12 sec) was selected. Actual testing with a hot levitated sample of tungsten (no e-beam heating) was successful. This system halves the drop time of the current system, and would presumably improve drop success significantly. It is still to be determined how robust the system is with missed drops, and how well the timing repeats as the system wears.

The remaining development needed with this new system is the actual block temperature determination. Discussions with GE led originally to the selection of a miniaturized commercial 100 ohm platinum resistance thermometer. It appeared that a custom version of the Hewlett/Packard quartz oscillator based

thermometer used for the existing system would have been required to meet geometry constraints, allow passage through a vacuum wall, and accommodate the calorimeter movement. The installation used for the existing RICE/GE system is unique to a nonmoving system, and would have been extremely difficult to adapt to the gulp calorimeter (requiring a hollow ram and other changes). Also, the 10 times larger increase in temperature rise anticipated relaxes the measurement constraint by the same factor. Although no commercial sources of electronic readout units capable of 0.001 K precision have been located, it should not be necessary to resort to potentiometric techniques to achieve this temperature sensitivity. However, a significant problem requiring some development exists here, as very small voltages will be necessary to avoid self-heating error and to minimize input energy to the calorimeter. In addition, DC determinations of the resistance of the thermometer are quite likely to be seriously disturbed by electromagnetic interference (EMI) for the RF heater. Thus, AC excitation and detection techniques will be necessary to determine the resistance of the thermometer. Expected heat inputs for the highest temperature experiments is of the order of 8000 J. Equilibration time for the gulp calorimeter will likely be between 1500 and 6000 seconds. For the upper limit estimate, if the thermometer is to contribute less than two percent of the total heat to the block, the maximum RMS voltage for excitation will be 1.6 volts. This is convenient for modern operational amplifiers, and a low (few 100 Hz) frequency AC self-balancing bridge circuit of this sensitivity should be within the state-of-the-art. The design may be non-trivial because of the electromagnetic interference rejection requirement. Other sensors, (e.g. thermocouples or thermistors) have been used, but are generally not considered to be as suitable (e.g., because of hysteresis). Temperature sensitive integrated circuits (e.g., Analog Devices AD590 or equivalent) might

be attractive temperature sensors, given that specialized apparatus to achieve the required sensitivity must be constructed.

The next steps to complete the development of the "gulp" calorimeter concept can be summarized:

1) Develop temperature measurement technique to required sensitivity with adequate EMI rejection.

2) Calibrate calorimeter by existing techniques, with specific emphasis on establishing validity of data analysis and calorimeter performance.

3) Incorporate changes as dictated by the results from 1) and 2), and repeat until calorimeter system heat capacity/temperature response is known over operating temperature range to 0.1 % level.

The unique RICE/GE interaction would seem to be ideal for this task, as the capabilities of RICE to accomplish the testing required in 2) appear a natural complement to the development expertise of GE in the completion of this task.

HEAT OF FUSION OF TUNGSTEN

The primary thrust of this project has been to assist RICE and GE in developing methodology for high temperature thermophysical property measurement utilizing the GE coupled RF Levitation/Electron-beam heating facility with a RICE supplied and operated calorimeter system. A prime problem in this work has been sample temperature determination, as the location of the levitation process in vacuum, the x-ray hazard posed by electron-beam heating and the high vapor pressure of the target material, tungsten, at its melting point all impose stringent requirements on optical access, and make commercial pyrometers impractical. For routine monitoring, GE developed an imaging system based on a silicon diode video camera, with selection electronics to allow using individual diodes as intensity detectors. Recent efforts [10]

have established the techniques for converting this type of device to a practical pyrometer system, with tracability to the International Practical Temperature Scale [11]. The combination of the apparent inability of the newly redesigned levitation coil to maintain liquid tungsten, the long cycle time of the calorimeter, the inherent noise characteristics of the existing camera system, and the difficulty of real time compensation for window obscuration have made actual temperature measurements extremely difficult. For that reason, and in order to isolate problems in this effort, it was decided to concentrate efforts on measurements at the melting point, with the specific aim of obtaining the heat of fusion of liquid tungsten.

Previous reports of this parameter have been primarily based on the Tamman Rule [12] ($\Delta H_m/T_m$ = 2.3 cal/mole.K {9.6 J/mole.K}, 1 calorie = 4.184 joule) used in the standard references [e.g., references 13 and 14]. This gives the value, 36 kJ/mole, for the heat of fusion using the best estimate value for the fusion temperature, 3695 K, determined by Cezairliyan [15]. Dikhter and Lebedev [16] reported ΔH_m of 80 ± 4 cal/gm, corresponding to 62 ± 3 kJ/mole. This value is probably too high, as it predicts a value for the entropy of melting (ΔS_m) of 17 J/mole.K, a value almost 25 percent higher than the currently highest known value for a transition metal (molybdenum, 12.9 J/mole.K. ΔS_m for tungsten is expected to be somewhat higher than for molybdenum, although too much of the data for the transition metals is estimated to draw strong conclusions. One would expect, in this region of the transition metal portion of the periodic table, that the second-to-third long period change in ΔS_m would be less than a 25 percent increase. Thus, this value is viewed as an upper bound. The report by Wouch, et al., [17] is based on the application of a cooling model to experimental data with rather large temperature error bounds. The model ignores supercooling, and yielded a heat of

fusion of 47.7 kJ/mole, with a corresponding entropy of fusion of 12.9 J/mole.K. From their reported fit to the model, a change in ΔH_m of 8 kJ/mole occurs with an increase of only 0.5 times the standard deviation of the best fit and ± 32 kJ/mole at the 2σ point is the variance in the fitted ΔH_m. Although somewhat insensitive, this model approach has produced the best estimate of ΔH_m prior to the direct measurements of this task.

Results of drops estimated to be 50 percent or more molten out of 25 drops for this work are given in Table 1. The estimates of percent melt for partially fused samples were based on visual inspection. Sectioning is planned to refine these values, but some of these samples may be reused in subsequent efforts, as partially melted samples are generally more successful. The completely melted sample was weighted 5 times the partially melted data in recognition of the uncertainty in the partial melt estimates. Two methods were used to derive essentially identical values of the heat of fusion. In the first method, the difference between radiation corrected [8] drop heat (molar basis) and the enthalpy value for the solid, 119.395 kJ/mole, from JANAF [18] was corrected to a 100 percent melted basis, and a weighted average taken. In the second method, a two parameter weighted least square analysis of corrected drop heat verses fraction melted was made. The heat of fusion was then just the slope of this function, and its intercept is the solid enthalpy. That intercept was 119.5 ± 2 kJ/mole, in excellent agreement with the JANAF [18] value. Because of this agreement, both methods are essentially numerically identical, and the value for the heat of fusion obtained by both methods was 53.0 ± 2.3 kJ/mole. The statistical uncertainty is of the order of twice the anticipated error from temperature uncertainty, excess e-beam disturbance of the calorimeter, and normal calorimetric errors.

Several factors contributed to the relative success of these efforts: 1) nearly flawless operation of the new automatic gate system; 2) improved initial stability and low outgassing of the specially cleaned ground samples [19], and improved heating and holding characteristics of the slightly smaller samples (a set of large samples (1.25 cm diameter, 20 gm) were extremely stable levitators, but proved impossible to melt, even on the surface); 3) the redesigned coil, which improved levitation stability (only in the case of sample N did the coil show any evidence of holding a molten sample, and that sample may have completed melting as it was being lowered in the coil preparatory to dropping in that case).

However, a number of problems, related to the age of the GE equipment, and the large number of hand operations necessary to ensure successful operation resulted in a significant number of failures (at least 1 in 4) due to system error, either outright hardware misfunctions or human error. The remainder of failures to melt are attributable to electron-beam adjustment failure. This appears to be the current primary difficulty to obtaining successful melting. A number of tests and setup techniques were employed in attempts to correlate tuning technique with successful melting. A special fixture to simulate high temperature emission grounding was constructed. One of the larger balls was mounted on a 0.32 cm diameter tungsten sting, attached to a baseplate flange, which allowed the placing of a specimen in the coil for beam focusing. This established that the levitation field did not seriously disturb beam focus, but pointed up a number of equipment improvements necessary to make tuning more reproducible.

It appears that successful melting occurs only when the electron beam is focused so tightly that it can actually "drill" a hole through the sample (see

figure 1a and 1b). The local heating is apparently considerable, and significant amounts of material are ejected, often with accompanying arc-induced shut-off of the RF generator and loss of sample. It would seem that this tight focus and consequent undesirable local heating should not be necessary for melting on the basis of estimates of the secondary emission characteristics at the melting temperature of tungsten. However, inability to observe and control the beam focus as desired has made systematic testing of focus effects difficult.

A new molybdenum shade ring, to protect the smaller work coil and to provide a run-to-run place to tune the electron beam witnout mounting special fixtures, will be installed. A number of minor hardware modifications to the e-beam control apparatus have also been suggested. These improvements should be completed about the time GE finishes the development of a new two-color pyrometry camera system, implementing part of the design proposed earlier [19]. In order to improve performance, a new series of smaller samples will be prepared with a weight of approximately 6-7 gm. In addition, a new coil with smaller (1.4 verses 1.6 cm) inside diameter and solenoid geometry to maximize the field gradient for these smaller samples and improve liquid holding capability has been designed and recommended to GE.

CONCLUSIONS

A prototype "gulp" calorimeter system has been developed and tested for mechanical performance. The design seems suitable for a potential flight experiment series, but a number of developments are still necessary before the unit operates as a true calorimeter.

The ground-based effort to determine thermophysical properties for tungsten have yielded a value of 53.0 ± 2.3 kJ/mole for the heat of fusion of tungsten. This value needs additional experimentation for confirmation, but

appears at present to represent a best value for that parameter. Experimental difficulties are still a serious problem. It is clear that the electron beam performance is the most important obstacle to successful levitation melting. Focus, beam shape, and positioning are all quite critical factors, even though the more than 3000 watts available is about 7 times the necessary power to melt the tungsten samples if absorbed. It is recommended that GE devote some effort to improving this aspect of their experimental facility, with a view toward determining the critical factors in electron beam melting of levitated specimens. Improvements have been suggested to improve control and allow some experimental tests to be performed.

It appears that this research still requires some developmental effort to achieve its goal of obtaining tungsten liquid enthalpy increments. The problems are understood, but will require laboratory time to resolve.

Table 1.

Sample	Weight, gm	Drop enthalpy,[a] kJ/M	% melted (est)	ΔHm,[b] kJ/M
A	7.895	158.36	75	51.9
D	9.740	148.62	60	48.5
F	9.473	148.44	50	58.2
G	9.596	158.83	75	52.7
N	9.468	172.58	100	53.18
RiA	9.3249	159.35	75	53.1
				53.0 ± 2.3[c]

[a]Radiation loss corrected

[b]computed on 100 % melt basis

[c]weighted average/regression - see text

REFERENCES

1. R. Munro, Private Communication, (1983).
2. T. Wang, Jet Propulsion Laboratories, Private Communication (1983).
3. P. C. Nordine and R. M. Atkins, Rev. Sci. Instrum., 53, 1456 (1982).
4. W. A. Oran, L. H. Berge, and H. W. Parker, Rev. Sci. Instrum. (1981).
5. C. D. Hendricks in "Materials Processing in the Reduced Gravity Environment of Space," ed. G. E. Rindone, MRS Symp. Proc 9, (North-Holland, New York, NY, 1982), p. 59-65.
6. R. T. Frost and E. Stockoff, Final Report, NASA Contract NAS8-34231, Task 7 (General Electric Space Systems Division, Vally Forge, PA, 1983).
7. J. Coops, E. S. Jessup, and K. van Nes, "Experimental Thermochemistry," ed. F. D. Rossini, (Interscience Publishers, Inc., New York, 1956).
8. D. W. Bonnell, "Property Measurements at High Temperatures - Levitation Calorimetry Studies of Liquid Metals," Ph.D Thesis, Rice University (1972).
9. G. Wouch, "Containerless Melting and Solidification of Metals and Alloys in the Terrestrial and Space Environment," Ph.D. Thesis, Drexal Univ. (1978).
10. G. Wouch, R. T. Frost, D. Rutecki, N. Beser, and E. C. Okress, Final Report, NASA Contract NAS8-34231 (General Electric Space Systems Division, Valley Force, PA, 1975).
11. D. W. Bonnell, "NBS: Materials Measurements," ed. J. R. Manning, NBSIR 81-2295 (1981).
12. IPTS-68 - The International Practical Temperature Scale of 1968 - Metrologica, 5, 35 (1969).
13. G. Tamman, Z. Phys. Chem., 85, 273 (1913).
14. K. K. Kelley, U.S. Bureau of Mines Bull. No. 584 (1960).

15. R. Hultgren, P. D. Desai, D. T. Hawkins, M. Gleiser, K. K. Kelley, and D. D. Wagman, "Selected Values of the Thermodynamic Properties of the Elements" (American Society for Metals, Metals Park, OH, 1973).

16. A. Cezairliyan, High Temp. Sci., 4, 248, (1972).

17. I. Ya. Dikhter and S. V. Lebedev, High Temp. - High Press., 2, 55,(1970).

18. G. Wouch, E. L. Gray,, R. T. Frost, and A. E. Lord, Jr. - High Temp. Sci., 10, 241 (1978).

19. JANAF Thermochemical Tables, NSRDS-NBS 37 (1972).

20. D. W. Bonnell, "NBS: Materials Measurement," ed. J. R. Manning, NBSIR 82-2560 (1982).

1a. Run P

1b. Run T

Figure 1. Recovered tungsten samples, showing electron beam "drilling" of stably levitated samples. Note the obvious signs of ejecta surrounding the site of melting. The specimens are 1 cm in diameter, and the hole in run T is about 0.7 cm deep.